Evaluation of a Wave Powered Water Pump Performance by Ocean Field Testing and WEC-Sim Modeling

By

Chelsea Kimball
Mechanical Engineering BS,
University of New Hampshire 2017

Submitted to the University of New Hampshire
in Partial Fulfillment of
the Requirements for the Degree of

Master of Science
in
Mechanical Engineering

September, 2023

This thesis was examined and approved in partial fulfillment of the requirements for the degree of Master's of Science in Mechanical Engineering by:

Martin Wosnik, Professor of Mechanical and Ocean Engineering and Director of the Center for Ocean Engineering

M. Robinson Swift, Professor Emeritus of Mechanical and Ocean Engineering

Nathan Laxague, Assistant Professor of Mechanical and Ocean Engineering

David Fredriksson, Professor of Mechanical and Ocean Engineering and Director of Center for Sustainable Seafood Systems

On Friday, August 4th, 2023

Approval signatures are on file with the University of New Hampshire Graduate School.

TABLE OF CONTENTS

LIST OF FIGURES

LIST OF TABLES

DEDICATION

For my family and their support:

Nova

Cam

Aly

Bryn

Lily

Chris & Steve

ACKNOWLEDGMENTS

The author would like to thank the following individuals who contributed their time, dedication, and equipment to make this project possible. For their guidance and project advising: Rob Swift and Martin Wosnik. Technical experts: John Ahern, Steve Pamboukes, Jon Hunt, Michael Monahan, and Paul Lavoie. The R/V Gulf Challenger team Bryan Soares and Jon Long for safe and successful equipment deployment and retrieval. The Shoals Marine Laboratory for the use of their moorings and web-camera, with a special thank you to Ross Hansen and Zach Charewicz. Small boat coordinators Dave Shay and Nate Rennels. The UNH Ocean Engineering Administrative team: Jane Miller, Sally Nelson, and Valerie Tillinghast. AMEC Program Manager Andressa Gutierrez. The UNH Media team for their incredible photographs and videos of the deployment: Jeremy Gasowski, Scott Ripley, and Beth Potier. Grant Milne and Jen Miksis-Olds for the hydrophone loan and acoustic expertise. Zach Moscicki and Tom Lippman for the Spotter wave buoy, mooring, and technical expertise. James Abare and Kevan Carpenter of UNH's Technical Service Center for 3D printing several key components. Nathan Daigle for waterjet cutting a key component. Anthony Westfall for expertise and tutorials in UNH's Premise computing cluster. Nathan Tom, Dominic Forbush, and the WEC-Sim development team from the National Renewable Energy Laboratory for troubleshooting the WEC-Sim model effort.

It takes a village to float a buoy.

This material is based upon work supported by the U.S. Department of Energy, Office of Science, Office of Energy Efficiency and Renewable Energy, Water-Power Technologies Office under Award Number DE-EE0009450.

LIST OF ACRONYMS

AMEC - Atlantic Marine Energy Center

BA - Biological Assessment

cm - centimeters

CAD - Computer Aided Design

CCOM - Center for Coastal and Ocean Mapping

DAQ – Data Acquisition

DOE - US Department of Energy

DOF - Degree of Freedom

Ft - Foot

FWS - US Fish and Wildlife Serice

GB - Gigabyte

Gpm - Gallons per minute

Hr - Hour

KB - kilobyte

Kg - Kilogram

Lbs. - Pounds

Lpm - Liters per minute

M - Meter

MLLW – Mean Lower Low Water

NH - New Hampshire

NMFS - US National Marine Fisheries Service

NOAA - National Oceanographic and Atmospheric Administration

NREL - National Renewable Energy Laboratory

OOA - Open Ocean Aquaculture

OTS - Off The Shelf

PA - Point Absorber

PPT – Parts Per Thousand

Psi - Pounds per Square Inch

PTO - Power Take Off

RAO - Response Amplitude Operator

RM3 - Reference Model 3

SML – Shoals Marine Laboratory

SS - Stainless Steel

SST – Sea Surface Temperature

STL - Stereolithography

UNH – University of New Hampshire

WEC – Wave Energy Converter

WPWP – Wave Powered Water Pump

ABSTRACT

A rising demand for macroalgae (or seaweed) has led researchers to seek out methods of increasing macroalgae aquaculture yields. Macroalgae is a food product, and may be used in biofuel, animal feed, and fertilizer. Applying upwelling technology to macroalgae aquaculture has been shown to increase biomass yield. A wave-powered upwelling device (or water pump) generates cold, nutrient-rich water flow to the surface of an aquaculture operation. A wave pump device developed at University of New Hampshire was refurbished and outfitted with instrumentation to determine its performance. Testing in the laboratory on both the device and instrumentation was conducted to prepare for field testing. An ocean field deployment of the device was conducted in March 2023. Five days of high-quality data were produced, revealing a maximum average flow rate of 16.5 gallons per minute, in corresponding average sea state conditions of 2.2 feet significant wave height and 5.9 second period. The maximum efficiency of the device over the course of deployment was estimated at 0.5%, which is an indicator that the current design is undersized for the tested wave conditions. A WEC-Sim numerical model of the wave pump was created, and validated using the field data. Comparing the average WEC-Sim model data to the field data resulted in a percent difference of approximately 19% for flow rates, 22% for stroke heights, and 16% for stroke periods, which is considered a successful model validation. A conceptual design for a modified, improved wave pump was generated, where increased flow rate and drawn depth were the motivating specifications. The modified design was modeled using WEC-Sim, which produced an average flow rate of 119.6 gallons per minute, and an efficiency of 4.8%. Determining and improving the efficacy of wave pump devices to benefit macroalgae production is a developing effort.

CHAPTER 1

Introduction

1.1 Background

Widespread interest utilizing upwelling technologies for aquaculture to increase productivity is a forward-thinking approach to sourcing crucial constituents for many global industries. An article from the Economist in October 2021, "Floating Offshore Farms Should Increase Production of Seaweed" [22] discussed several teams around the world using wave powered upwelling technology to increase kelp productivity. Experiments have shown that upwelling can increase kelp productivity by up to four times and extend the kelp growing season further throughout the year [45]. The Climate Foundation is working on a four phased approach to develop several marine permaculture projects, including deploying upwelling devices in the field at a macroalgae farm in the Philippines. The devices used in that project will be developed by the company Atmocean. The Helmholtz Center for Ocean Research has also been examining upwelling technology and has found that pumping rates which are too high are less effective at keeping the cold, nutrient rich waters at the surface. The fast rate causes the water to sink back to the bottom before the kelp has had a chance to benefit from its presence. Secondary mixing type devices may be required to increase efficiency for fast pumping or large-scale devices. Another project includes Otherlab, which has an ARPA-E grant to work on tethering kelp beds close to the ocean floor using ROVs and developing upwelling devices for mariculture. The ARPA-E MARINER program aims to develop the United States' macroalgae industry into a global biomass producer to create viable feedstocks for biofuels, chemicals, and animal feeds [39].

The UNH Wave Powered Water Pump (wave pump) enhances macroalgal mariculture by upwelling the colder, nutrient-rich waters from lower in the water column to the surface. The macroalgae can additionally produce more biomass and can continue producing longer through the warmer seasons. Analysis and optimization of the device design and operation was essential to understanding its capabilities. The device's survivability, efficiency, and flow rates in various wave conditions required evaluation. Knowledge of device performance will allow for correct sizing to individual mariculture projects. Evaluating the design also creates opportunities for optimization. Field data of device performance was used to validate a WEC-Sim numerical model of the device. A validated numerical model allows for simulated design changes, which can aid in optimization and decision making for development of future models of the device.

1.2 Oceanic Characteristics to Enhance Macroalgal Mariculture

There were several varieties of kelp which were considered optimal for biofuel feedstock. In the Gulf of Maine *Saccharina latissima* (sugar kelp) and *Laminaria digitata* (oarweed) are mariculture crops that have potential for use as a biofuel feedstock [32]. Around the world, there are other kelp species being considered for biofuel feedstock such as *Saccharina japonica* (ma-konbu), *Macrocystis pyrifera* (giant kelp), and others [42]. Each species of kelp has its own optimal growth conditions dependent on water temperature, nutrient profiles, and light conditions. Regional and seasonal variations in ocean conditions drive different device requirements for each mariculture location. Given that factors related to kelp mariculture are highly variable, designing an upwelling device to aid kelp growth depends upon many site- and project-specific characteristics. These characteristics will determine the depth of the device intake pipe and optimal flow rate. The amount of kelp grown will also determine the number of upwelling devices required to serve the farm area.

Several kelp studies determined that optimal water temperatures and exposure to high levels of nutrients had positive kelp growth correlations. A laboratory study on *L. digitata*

found that at water temperatures of 26°C 100% of specimens died, whereas at 20°C 40% died, and at 16°C they all survived within a three-week period [70]. The highest growth rates occurred at 12°C, and the macroalgae were able to absorb more nitrogen in the colder water. This confirmed the findings in an earlier study by Bolton and Luning (1982)[12], which found *L. digitata* experienced peak growth at 10°C, and did not survive at temperatures beyond 23°C. This indicates that a temperature difference of 4°C can have a large impact on the health and yield of *L. digitata* farms. Where there are steep thermoclines, an upwelling device that gradually cools the surface waters could help increase survivability and productivity of *L. digitata*.

Similar studies were completed for *S. latissima* to determine what conditions best foster growth. *S. latissima* has a slightly larger temperature range for optimal growth from 10 to 15°C and cannot survive in water temperatures beyond 23°C [12]. A land-based study compared the growth rates of *S. latissima* in tanks of surface water (13.1°C) and in tanks of deep water (10.2°C and higher in nitrate concentrations). The kelp in the deep-water tanks grew at a rate approximately three times larger than that of the kelp receiving surface water [30]. Another land-based tank study involving *S. latissima* also found a positive correlation between kelp growth and nutrient availability [11]. An offshore *S. latissima* growth study determined that the highest growth rates occurred when the temperatures were cooler and at depths of 5m [5]. These studies indicate that cooler and nitrogen rich waters were conducive to producing optimal growth in *S. latissima*, while the macroalgae still has access to sunlight in shallower waters. Upwelling devices in *S. latissima* mariculture can aid in creating these optimal conditions for longer periods of time throughout the year.

Similar to employing upwelling devices in kelp mariculture, another practice proposed by growers was depth cycling the cultivation lines to expose the macroalgae to the cold nutrient rich waters at night and returning them to shallow waters in the day for photosynthesis. In California, a study on giant kelp (*M. pyrifera*) attempted this novel growth practice of depth cycling and found the kelp had increased biomass of four times that of the non-

depth-cycled kelp [45]. During the daytime the cultivation lines were 9m deep, and at nighttime they were dropped to 80m deep. Throughout the experiment from May to July, the water temperature at the 80m location remained within 10-11°C, and at the 9m location varied from 16-20°C. Nitrate concentrations on average were much higher at the deep-water location (18μM) compared to the surface (approximately 0μM). The depth-cycled kelp had a maximum growth rate of 5% per day, and had elevated protein and Nitrogen concentrations compared to non-depth-cycled kelp. Continuous upwelling of the deep, cold, nitrogen-rich water to the surface could potentially create the same enhanced growth effect for *M. pyrifera*.

While site- and project-specific characteristics will drive exact device specifications, many macroalgae biological studies indicate that exposing kelp to deeper waters which were cooler and more nutrient-rich will increase growth. Upwelling this water directly to the kelp at the surface using the UNH wave pump device may provide optimized growth conditions. Creating a kelp mariculture site with an environment primed for excellent productivity may increase the harvest yield by up to two to four times, and could also extend the kelp growing season. The number and size of devices and depth of the intake pipe will need to be considered for each mariculture location and kelp species.

1.3 Prior Work on Wave Powered Upwellers

Development of wave powered upwelling devices was a research focus for several groups worldwide. One of these devices was the UNH wave pump that upwells nutrient rich water to the photic zone to enhance macroalgae mariculture. This review mainly focuses on wave powered upwelling devices designed since 1976, and reviews some Wave Energy Converter (WEC) devices that utilize pumped water for electric energy generation. Reports on WEC devices contain applicable lessons learned, novel designs, and numerical modeling efforts similar to the UNH wave pump modeling efforts.

A similar conclusion was drawn by different research groups that WEC devices in the field and in numerical modeling had increased device efficiency in lower frequency waves and

irregular waves compared to higher frequency waves and regular waves. This trend may aid in informing the UNH design. Another common trend was that when WEC devices were in the field for experiments, many researchers report device durability as a critical issue.

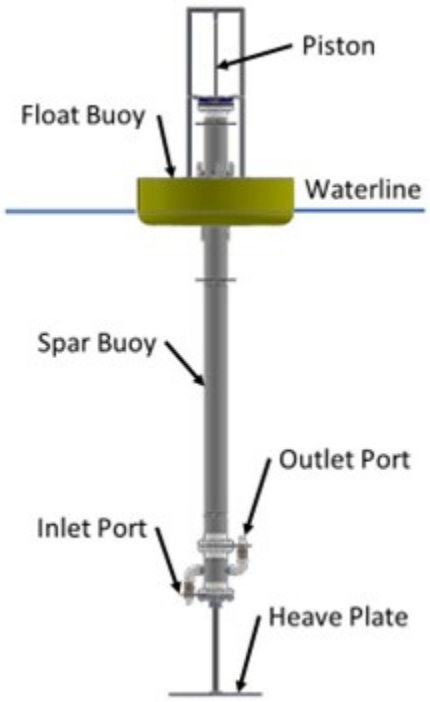

Figure 1.1: Simplified overview diagram of UNH wave powered water pump design, which was made using CAD SolidWorks software.

The UNH wave pump design was a two-body point absorber (PA) WEC that acts as an upwelling pump (Figure 1.1). The UNH design was novel amongst the eleven devices reviewed. Amongst the reviewed devices, no other WEC upwelling device was configured in the same way with two check valves at a centralized, underwater location.

Several of the reviewed research papers focused their WEC development process on numerical modeling. In these papers the software tool WEC-Sim [55] was a reliable method for numerical modeling efforts. The WEC-Sim tool was a Matlab based code, which uses device geometry and Power Take Off (PTO) characteristics to model performance in various wave fields. These papers were used to inform the UNH efforts to apply WEC-Sim for modeling the wave pump.

Isaacs et al. (1976) [28] developed a simple, one-body wave powered water pump design, which has been utilized by many other researchers since (Figure 1.2). The goal for this device was electric energy generation, and the focus of the paper was not on upwelling or flow rate. This design comprised a vertical riser (or pipe) in the water column, with a single one-way flapper valve (upwards flow only) located midway on the intake pipe. A slack tethered float attached at the top of the tube utilized the wave motion to gradually pull water from significant ocean depths to a reservoir at the surface. The pressure within the reservoir relied on the length of the pipe and the sea state conditions (wave height and frequency). By testing a variety of differently sized prototypes in several wave conditions, the researchers determined that devices must employ the full extent of available wave heights for maximum efficiency. They also determined that for device success, survival in various wave fields and durability was critical. In 1.8m waves Isaacs tested a 61m and 92m long device where each device was positioned vertically in the water column. The 92m long pump, which had a diameter of 5cm, created a pressure equivalent to 30psi in wave heights of 2ft. This device had a successful deployment of two months, and a reported efficiency of about 30%.

Using a similar version of the Isaacs wave pump, Wick and Castel (1978) [69] conducted field tests in Kaneohe Bay, Hawaii. A small-scale model of the Isaacs design was used to produce electricity, and the data were sent ashore using a telemetry system. The device's three polyethylene intake pipes were each approximately 5cm in diameter and 92m long. The pumped water was considered a by-product of electrical energy generation, so the flow rates were not measured or reported in the data. The generator failed early due to corrosion, but these tests lasted a total duration of four months and ended when the mooring system failed. The dead weight to hold each pipe in place during deployment was 400 pounds. While the tests did last four months, this team also experienced durability issues when one of their pipes broke during deployment. In wave heights of 3 to 4ft, and wave periods of 6 seconds, the pump was able to achieve a peak pressure at the outlet of 40psi, which was reported at around 25% efficiency.

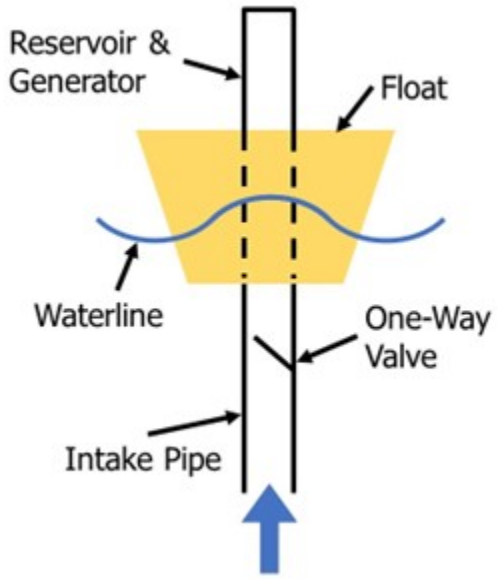

Figure 1.2: Representative diagram of Isaacs et al. (1976) WEC upwelling device, diagram not to scale. [28]

Vershinskiy et al. (1987) [66] created a single-body wave pump specifically for upwelling, which was moored and ballasted. This device comprised a vertical tube, with the valve at the top instead of the bottom. The goal was to determine whether it would create increased algal blooms or effect local coastal climate. Water characteristics were tested alongside the device including temperature, salinity, oxygen, and mineral content. Two different lengths of devices were tested, 22m and 204m, in the Black Sea in 1983. The device was characterized as low cost by the design team. For the device pumping from 22m depth, mineral contents increased by two to nine times that of naturally occurring levels, and temperature decreased by approximately 8°C. For the 204m device, mineral contents increased by six to fifty times naturally occurring levels, and surface temperature decreased by 15°C. From the 22m device with a 0.30m diameter in 0.35m wave height and 4 second wave periods, flow data was approximately 36m^3 per hour. The team also estimated the flow rate for a 100m long device with a 1.2m pipe diameter in 2m high waves with 8 second periods as 3600m^3 per hour. They concluded their study emphasizing the likelihood of these devices being able to generate algal blooms and to cool local coastal climates.

Liu et al. (1991) [37], a team from University of Hawaii performed laboratory testing of another wave powered upwelling device. This device was a two-body point absorber and used a deep-water pipe, a valve at the top, and a floating tank with an air chamber. The wave driven relative motion forced water out the discharge pipe at the surface. The goal of this device was to enhance fish mariculture through upwelling by increasing mineral content and flushing out pollutants. It was designed to operate in wave conditions of 2m height with 8 second periods. The research team recognized that a potential challenge for their device was controlling the plume mixing after achieving regional upwelling. The scale model for laboratory tests was 1:20, and the model was constrained to move vertically. Theoretical flow rates for the device were calculated for various pressures within the chamber from 0.6psi to 1.8psi. For the full-scale device predicted flow rates for each range of pressures were $601\frac{m^3}{hr}$ and $680\frac{m^3}{hr}$, respectively.

Numerical modeling of a similar device, but with the reservoir at the top removed was conducted in 1995 [38]. The device had a float buoy 4m in diameter, with a pipe of 1.2m in diameter open at the top. The length of the pipe was 300m and had the check valve near the top. Both regular and random waves were simulated in the numerical model. Modeling the random waves was done using a Bretschneider Spectrum using the same 2m high, 8 second period waves characteristically found off Oahu, Hawaii. Assuming the float was a wave follower, random waves were found to produce a nearly continuous flow, whereas regular waves had more time where the flow was zero. The results for this device in the numeric model were flow rates of 3420m^3 per hour in random waves and 1620m^3 per hour in regular waves. To validate the numerical model, wave tank experiments using a 40:1 scale physical model of the device were later performed. Using the numerical model, flow rates of 1800m^3 per hour in regular seas were calculated for the full-scale device [36]. These laboratory and numerical results followed similar trends to Isaacs' and Vershinskiy's test results.

Kirke (2003) [34] modified the designs of Liu and Vershinskiy to create an upwelling device designed to operate over a large area in the ocean. The motivation behind this design

change was to increase algae in surface waters which would ultimately support larger schools of fish. Side effects of this kind of device would reduce ocean temperatures, which would help to decrease storm severity and coral bleaching in tropical areas. If negative side effects occurred, the team proposed that removing the devices from the water would easily reverse those effects. The devices were designed to upwell from 500 to 600m depths, which was the deepest upwelling device reviewed. Kirke proposed a design with the following modifications: moving the check valve to the bottom of the pipe, using three vertical pipes for upwelling instead of one, using fabric for the tubes to enhance durability, using an efficient WEC terminator (like Salter's "Duck") instead of a simple float, and mooring the device on the bottom using elastic tethers. The check valve at the bottom of the pipe would maintain rigidity of the flexible pipe on upstrokes. A numerical feasibility study was completed to determine whether the design would be capable of pumping 50m^3 per second (180,000m^3 per hour). Kirke predicted that a float 21.5m in diameter and 40m in height operating in 2m high waves with wave periods of 12s at 80% efficiency would be sufficient to achieve the desired pumping rate. This was a much larger device than the previously reviewed works and was also much larger than the UNH wave pump research project.

A commercially available wave powered upwelling device by Atmocean was tested off the coast of Hawaii in 2010 [68]. The design of the pump was based on the pump created by Isaacs in 1976, but its goal was changed to upwelling and not electricity generation. Due to the changing objective, the modified design increased the pipe diameter. This design differs from the UNH design in that the water travels up the length of the tube, with a single flapper valve at the bottom (Figure 1.3). The pumps were tested by pulling 300m water depths to the surface and achieved an approximate flow rate of 16 m^3 per hour. Flow rate was measured by a MAVS3, and ocean gliders were deployed to measure local environmental properties. In a mean wave height of 2.4m the device experienced a critical failure after 17 hours. The team analyzed the failures and believed the main issue was due to lack of durability in the tube material, which was made of polyethylene. Additional failures included mangled

hardware in various regions along the pump. The efficiency of the pump was also very low, at approximately 10%. Friction losses in the tubes could have contributed to the efficiency losses. One key takeaway from this paper was that upwelling velocity depends heavily upon wave amplitude and frequency, which were the two important inputs for numerical modeling. Pressure was not measured in the pump for this study.

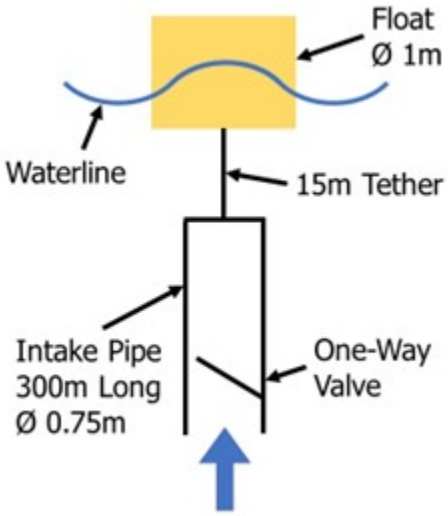

Figure 1.3: Representative diagram of Atmocean WEC wpwelling device, diagram not to scale. [68]

In 2015 a French team of researchers published the results of a twelve-year case study on their WEC development, SEAREV [17]. This WEC was a free-floating point absorber that utilizes an internal, heavy pendulum to produce electricity. While this device does not create upwelling effects, the lessons learned in this study were applicable to the UNH project. The researchers found that the three most important factors in WEC design were survivability, maintenance, and performance. The device shape was optimized over several iterations of the prototype. Optimization factors included reduction in slamming as waves pass by and of waves breaking on the float, greater stability, and avoiding flat panels. The shape of the float that the team ultimately settled on was very similar to Salter's "Duck". By utilizing a braking mechanism of the internal pendulum at optimal moments, the energy

efficiency of the device was improved by 35% in their first-generation design and by 15% for their second-generation prototype. Unfortunately, the team found in their cost analyses that the first-generation prototype was too expensive to be market competitive at full scale, and while the same was true for their second-generation prototype it at least produced double the energy generation.

Returning to the concept of using wave energy for a hydraulic pump, a team of researchers from the Netherlands had a novel idea for a device [67]. Instead of the single vertical upwelling pipe, this team had the idea to use a system of floats, referred to as a floater blanket, to power multiple piston pumps. The floater blanket aligns with an incident wave, to provide power to the multiple piston pump PTO system more continuously. The team created a numerical model of their device using WEC-Sim, which was used to evaluate both analytical and laboratory experiments. Good agreement between experiments, other analytical models, and the WEC-Sim model, indicates that the WEC-Sim model was reliable for this device. The numerical model takes approximately a day to complete the simulation in the Matlab code. In the numerical model, the team found that the device performed well in wave conditions with long periods, but not for short period waves due to diffraction and radiation effects. The team also noted that varying the piston spacing and employing a control algorithm drastically affected the efficiency of the device.

Another wave powered pumping design that differs from the upwelling devices was comprised of flexible tubes and check valves which direct the flow downwards into an accumulator and turbine located underwater [47]. The flexible composite tubes were unique to this application and were made of an elastomer and carbon fiber. The material was capable of withstanding high pressure, non-corrosive in saltwater, durable, and required no moving parts. Due to the flexibility of the tubes, a small external load creates a large volume change. As a wave approaches the surface float rises, and the attached tube was stretched. The bottom of the tube was attached to a stationary plate. In the wave trough, the tube was relaxed, and allowed water inside through the tube's top. As the float neared the wave

crest, the tube stretched closing the valve at the top and opening the valve at the bottom, which caused the water to be forced downwards. The water pumped downwards was stored in an accumulator which can then be used to power a generator (Figure 4). Both a numerical model analysis and 50:1 physical scale model test were performed for the prototype device. The reduced model scale testing produced efficiency of 40%, with 0.21W produced. For the full-scale version, the researchers expect this technology to produce 180kW. The researchers also note that the composite material could also be used for PTO tethers in other two-body point absorber WEC designs.

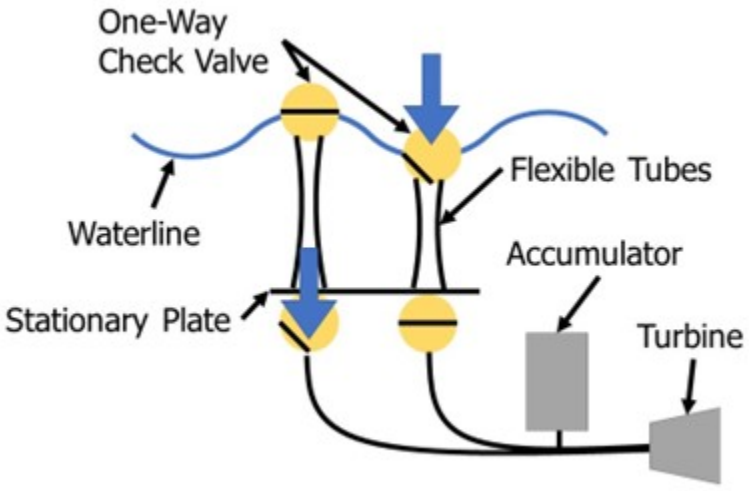

Figure 1.4: Representative diagram of WEC downwelling device, diagram not to scale. [47]

A smaller scale electrical energy generating WEC device was designed specifically for the Colombian Pacific Ocean [41]. This device does not use pumps or upwelling and was modeled using WEC-Sim. This device was designed for coastal communities which were far removed from electrical grids. Heave motion drives a linear generator for the power. The surface floats were attached to an arm, and they move vertically with the wave motion. The other end of each arm was attached to a pivot mounted at the top of a vertical piling embedded in the sea floor. The arm rotates about a horizontal mean position as the float oscillates vertically. The linear generator was stored in each arm, which were oriented horizontally, and the translator slides along the stator coils. Numerical models were created for the device

in WEC-Sim and Ansys Aqwa. In typical swell conditions found along the Colombian Pacific coast (1.17m height and 10.6 second period), the device generated 1.17kW in irregular waves and 0.5kW in regular waves. The research team reported an efficiency of 42%, where lower wave frequencies increased the efficiency. This was another instance of long period waves producing higher efficiencies.

Table 1.1: Summary of Reviewed WEC Device Designs and Performance
* Indicates modeling effort, with no laboratory or field tests performed at time of publication.

Source	Device Type	Device Production	Float or Pipe Diameter	Target Depth	Reported Performance	Reported Efficiency
Isaacs et al. 1976 [28]	One-Body P.A.	Electricity	0.05m	92m	30psi	30%
Wick and Castel 1978 [69]	One-Body P.A.	Electricity	0.06m	92m	40psi	25%
Vershinskiy et al. 1987 [66]	One-Body P.A.	Upwelling	0.30m	22m	36 m^3/hr	N/A
Liu et al. 1999 [36]	Two-Body P.A.	Upwelling	4.0m	300m	1800 m^3/hr	N/A
Kirke et al. 2003 [34]	One-Body P.A.	Upwelling	21.5m	500 - 600m	180,000 m^3 /hr	80% *
White et al. 2010 [68]	One-Body P.A.	Upwelling	1.0m	300m	45m^3/hr	10%
Cordonnier et al. 2015 [17]	One-Body P.A.	Electricity	30m	Surface	1620 MWh/yr	25% *
Wei et al. 2017 [67]	Attenuator	Electricity	N/A	Surface	Varies *	Varies *
Philen et al. 2018 [47]	Attenuator	Electricity	0.006m	Surface	0.21W	40%
Romero et al. 2019 [41]	Attenuator	Electricity	N/A	Surface	1.17kW (irr. waves)	42%
Yetkin et al. 2021 [71]	Two-Body P.A.	Electricity	Varies	Varies	Varies *	Varies *

Another numerical approach to a two-body point absorber WEC was studied by taking a closer look at optimizing control systems on the WEC to increase efficiency and survivability [71]. Both hard and soft constraints on the device motion were analyzed in this numerical model, to determine effectiveness and the impact of these additional costs on WEC devices. WEC-Sim was used to develop the numerical model and study the relationship between the constraints and energy absorption. End stops were employed in the simulated PTO,

which were also used in the UNH WEC-Sim numerical model. A more advanced control system may also be necessary to apply forces to counteract excessive sea state conditions, which will increase the durability and longevity of the device. The researchers' control model incorporated the energy expended by using the control force, which had not yet been done in earlier control models.

A summary of the WEC devices reviewed in this paper is found in Table 1.1.

The techniques described in these papers to study WECs, and their lessons learned will be applied to the UNH wave pump research project. Specifically, device durability, WEC-Sim for numerical modeling, and ideal wave conditions will all be used to influence the UNH design. The UNH design will be field tested for volume flow rate in various wave field conditions to evaluate performance. This data will also be used to validate numerical models of the UNH wave pump. Lessons learned from the field test will inform improvements to the design as well as provide insight into a commercial scale design.

1.4 Project Objectives

The objectives for this project were as follows:

- Upgrade existing UNH wave pump device
- Develop numerical model of wave pump device using WEC-Sim
- Conduct ocean field test of existing wave pump device measuring: flow rate, relative motion, and wave conditions
- Validate WEC-Sim model using ocean field data
- Redesign wave pump with knowledge gained and WEC-Sim model

1.5 Project Approach

An ocean field test was required to evaluate the existing wave pump device design. To ensure the device survived and succeeded in an ocean field test several hardware improvements, instruments, and laboratory tests were required. Details of the hardware refurbishment were

included in chapter 2. Instrumentation was purchased and integrated, as well as developed specifically for the device. Instrumentation includes a Sofar spotter buoy for capturing nearby wave conditions, a lidar, and a flow meter. A custom-designed data acquisition (DAQ) module was built to power and capture the data. Details of the instrumentation were included in chapter 5. These instruments allow for recording volumetric flow and relative motion of the wave pump in various sea states.

The process detailing the ocean deployment methods was included in chapter 6. The data from the deployment were applied to validate numerical models of the device. A numerical model in WEC-Sim and Matlab were constructed to simulate the device in a variety of wave conditions. A comprehensive description of the numerical model was included in chapter 3. The performance of the wave pump device during the ocean field deployment was assessed in (chapter 7). These results were applied to the numerical model for validation (chapter 8). Using the validated numerical models, optimizations and improvements to the device design were suggested, and a modified, larger-scale design was proposed in chapter 9. Key findings and potential for future work was reviewed in chapter 10.

CHAPTER 2

Wave Powered Water Pump Design

2.1 Overview

This chapter covers details of the wave pump design and how it operates. Applicable theory for WEC dynamics are also reviewed.

2.2 Detail of Design and Operation

The wave pump is a two-body WEC point absorber device. The two main components are a float buoy and a spar buoy (Figure 2.1). The float buoy is characterized as a 'wave follower' and moves vertically with the waves at the surface. Whereas the spar buoy remains relatively stationary in the water column due to an attached heave plate.

Inside the spar was a piston, which was connected to the float buoy. At the lowermost end of the spar was an inlet and outlet pipe system with check valves. As the waves move the float up and down, the motion moves the piston which causes seawater to be pulled and pushed through the pipe system. The inlet was angled downwards to pull in deeper water, and the outlet was attached to a hose that brings the water towards the surface. The hoses were not shown in (Figure 2.1). The wave pump operates by drawing water in on the wave upstroke and pushing the water back out on the down-stroke (Figure 2.2).

The device was approximately twenty-two feet tall when in its equilibrium position (when there were no waves acting on the device), approximately sixteen feet of which were sub-

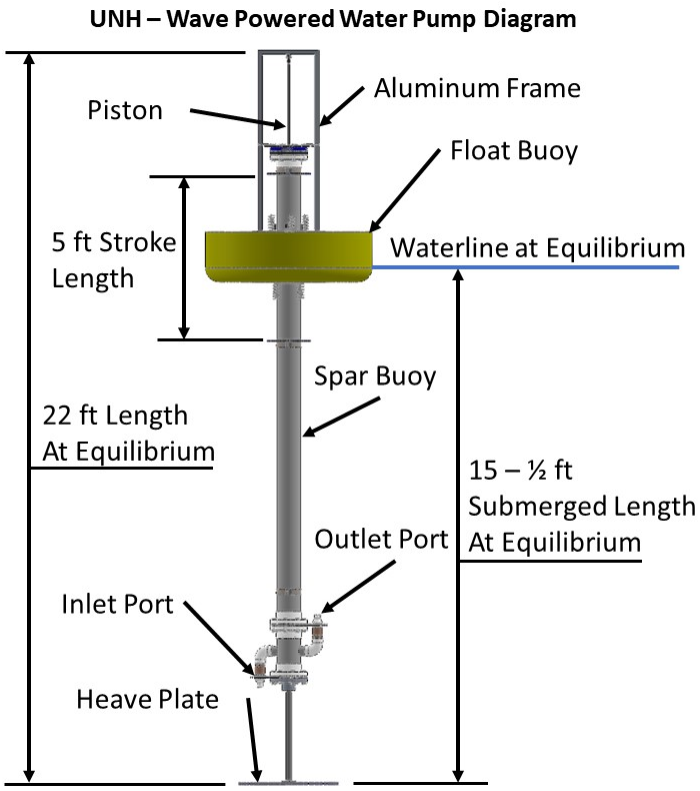

Figure 2.1: Detailed overall diagram of wave powered water pump design, created using CAD SolidWorks software.

merged when deployed. The float buoy was five feet in diameter and yellow, which provides high visibility for spotting of the device. The float buoy was made of Surlyn® ionomer foam. The heave plate at the bottom of the spar buoy helps inhibit vertical motion of the spar buoy due to wave action. The spar buoy was constructed from a Schedule 40, size 8 PVC pipe (8.6-inch outer diameter). The wave pump device's total weight was estimated at 680 pounds.

Additional details on the wave pump design and construction were included in chapter 4. The majority of the device construction was detailed in previous UNH technical reports [13]. The piston cylinder was the four inch diameter PVC pipe that was installed inside the main spar float PVC pipe. The piston was an aluminum 6061 cylinder which was machined to contain three O-ring grooves. The piston was attached to a piston rod, made of 316SS. The rod is comprised of three, four-foot long sections, which were joined together with

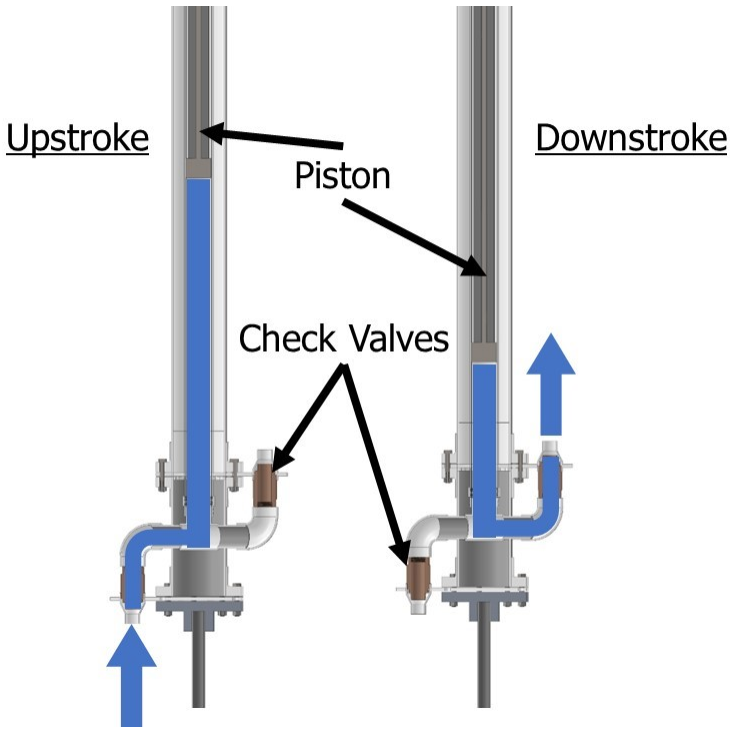

Figure 2.2: Cross section of wave pump with Detail on Pump Operation

small threaded rods. The check valves were off-the-shelf (OTS) components, purchased from McMaster-Carr, part number 7746K47. The gantry or aluminum frame attached to the float buoy was constructed from extruded aluminum 6061 components. The stopper plates installed on the spar buoy to constrain the float motion were constructed from plywood. The plate at the top of the spar is constructed from marine-grade UHMW-PE. The majority of the ballast is comprised of a pipe flange at the bottom of the spar, which is also OTS from McMaster-Carr with part number 68095K397.

During the previous field test in April 2021, the wave pump was measured pumping approximately two gallons per minute [13]. However, prior to the March 2023 field test, the range of pumping flow rates for this device were unknown. Numerical model simulations indicate pumping rates up to eleven gallons per minute were possible in the average summertime wave conditions. The maximum stroke length for the device was four feet and was constrained by stopper plates and compression springs.

2.3 Applicable Theory

The existing wave pump design was developed utilizing dynamics of floating bodies, hydrodynamic stability, and typical wave conditions present in the Gulf of Maine [14], [43], [13].

Motion of floating bodies in a time series approach was characterized by:

$$m\ddot{X} = F_{ext}(t) + F_{md}(t) + F_{rad}(t) + F_{pto}(t) + F_v(t) + F_{me}(t) + F_B(t) + F_m(t), \tag{2.1}$$

[55] where:

m = Mass matrix

$\ddot{X}$ = Translational and rotational vector of the device

F_{ext} = Wave pressure force includes a Froude-Krylov force component and diffraction component

F_{md} = Mean drift force

F_{rad} = Force and torque vectors produced by wave radiation includes an added mass component and wave damping component

F_{pto} = Force and torque vector produced by PTO

F_v = Force and torque vector produced by damping

F_{me} = Force and torque vector produced by Morison Element, specifically the drag term from the Morison Equation [44]

F_B = Force and torque vector produced by net buoyancy

F_m = Force and torque vector produced by mooring connection.

The dynamics of the float buoy and spar buoy were analyzed in the WEC-Sim numerical model (see chapter 3 for more detail). The results were then compared to the lidar field data which collected relative motion data. This comparison was utilized in chapter 8 to validate the WEC-Sim numerical model.

Dynamic stability of the existing wave pump device has been a challenge throughout the

course of the project, even as recently as April 2021 [13]. The first challenge lies within balancing the ballast and buoyancy forces along the spar buoy so that the waterline was located between the stopper plates. See section 4.9 and subsection 9.3.1 for more details on this topic.

If this was achieved in a hydrostatic environment, the next challenge was applying this balance in an environment with ocean waves. Examining the pitch (or roll) dynamics of the device in waves indicates the device's ability to right-itself or remain upright in wave forcing.

Resonant periods or frequencies of buoys indicate the wave period at which buoys experience the most motion. For a two-body WEC, the resonant period indicates the frequency or period at which the most relative motion between the bodies was present. Response Amplitude Operators (RAO) were a good indicator of resonant frequencies. For both the field data and the WEC-Sim modeling, relative motion RAO's were calculated in subsection 7.11.1 and subsection 8.2.1.

2.4 Hydrostatics of Existing Device

The existing device for the field deployment experiment was analyzed for its hydrostatic characteristics and stability. By focusing on the spar components, which excluded the float buoy, gantry, and piston, the following information was calculated using SolidWorks. Densities for each material were defined for each component in SolidWorks, to determine the total weight and center of gravity. The total weight of the spar float assembly, including the flow meter sensor and data acquisition (DAQ) module, was 179.148kg. The center of gravity (h_g), equilibrium waterline location (h_{wl}), and center of buoyancy (h_b) are shown on Figure 2.3. Locations for these distances on the diagram are approximate.

The waterline location was determined by measuring the device submerged in saltwater with an approximate density of $1025\frac{kg}{m^3}$. The center of gravity was determined using SolidWorks. The center of buoyancy was estimated as half the waterline location, assuming that

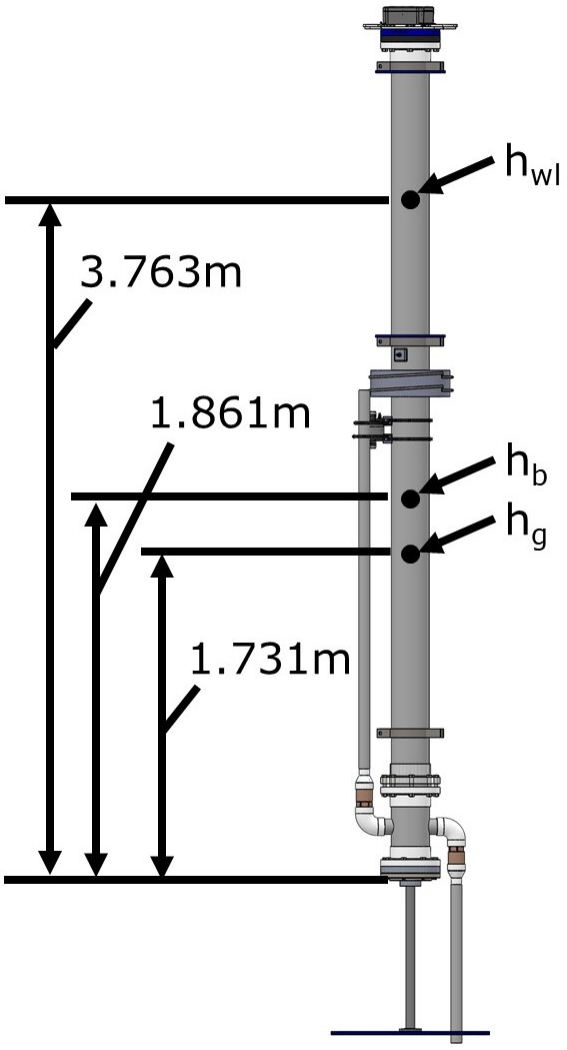

Figure 2.3: Diagram of spar buoy assembly with equilibrium waterlineh_{wl}, center of buoyancy h_b, and center of gravity locations shown h_g (not to scale).

the volume of the heave plate was negligible, and that the spar assembly had a uniform geometry.

The distance between the center of gravity and the metacentric height, m, is calculated by:

$$g\bar{m} = \frac{I}{V} + \bar{bg}, \tag{2.2}$$

[64], where:

$g\bar{m}$ = Distance between the center of gravity and metacentric height = 0.152m

I = Second moment area of inertia = 1.113e-4m^4

V = Total submerged volume, calculated using SolidWorks = 0.175m^3

$\bar{bg}$ = Distance between center of buoyancy and center of gravity = 0.151m

Since the metacentric height is above the center of gravity, the spar is initially stable. However, since the metacentric height is close to the center of gravity, in large wave states the spar is susceptible to tipping. This was later observed during the field deployment (chapter 6). A lower center of gravity and higher metacentric height will reduce instability in future designs, which was explored in chapter 9.

CHAPTER 3

Development of WEC-Sim Numerical Model

3.1 Overview

A simulation based on a numerical model is a useful design tool for engineers, researchers, and scientists. By creating an accurate model and simulation, designers can modify wave conditions to match different sites and determine device performance. The device geometry and hydraulic Power Take-Off (PTO) can also be iteratively modified within a model and simulated to determine what features increase device performance and survivability. Field data was used to validate the WEC-Sim model in chapter 8. The validation process indicates the degree of accuracy for the WEC-Sim model that can be expected during the design process.

WEC-Sim is a numerical modeling software specifically designed for simulating wave energy projects [55]. For the wave pump device, simplified geometry files were created using SolidWorks [10] and Meshmagick [53]. Then using Capytaine [3] [6], the Boundary Element Method (BEM) analysis was completed using the geometry files to determine the hydrodynamic response of the device. Capytaine software is a linear potential flow solver. This analysis was then uploaded to WEC-Sim. By modifying the included Reference Model 3 and corresponding hydraulic PTO model in the WEC-Sim software, a numerical model of the wave pump was created. Matlab [40] and Simulink [62] are required to use the WEC-Sim program. The outputs from the WEC-Sim program include device dynamics and flow rate.

3.2 Applicable WEC-Sim Theory

WEC-Sim simulations involve relationships between wave state, WEC device dynamics, device power-take-off (PTO), and WEC mooring. Calculations of radiation and diffraction allow for predictions of device performance in a given wave state. These calculations rely upon hydrodynamic forces solved using BEM analysis. For a comprehensive description of WEC-Sim's operational theory, see [55].

Coordinate System and Units The WEC-Sim coordinate system was oriented so that the surge and sway motions were along the X and Y axes, respectively. Heave was oriented along the Z axis (Figure 3.1).

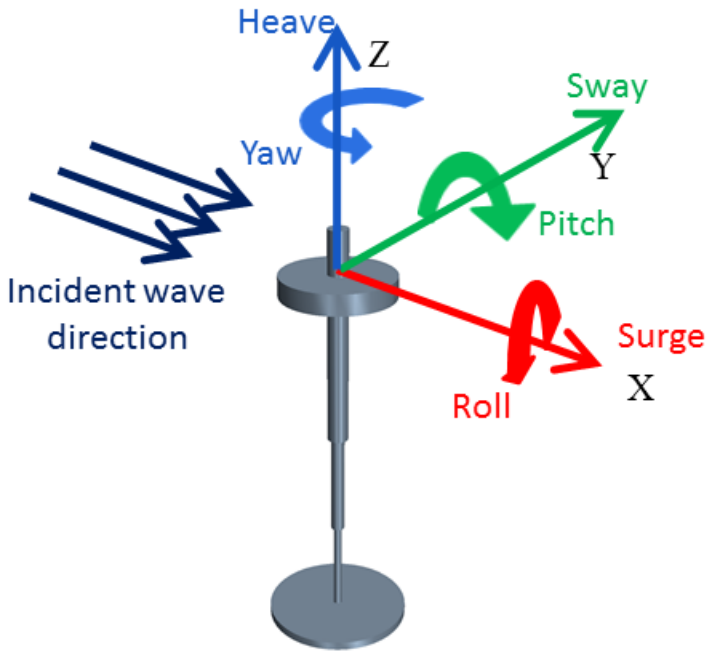

Figure 3.1: WEC-Sim coordinate reference system diagram [55]

The units for WEC-Sim were metric. Distance was measured in meters, mass in kilograms, and time in seconds. Angles were measured in radians, but wave directionality was

measured in degrees.

Hydraulic PTO The two governing equations for the hydraulic PTO were given by:

$$F_{PTO} = \Delta p_{piston} A_{piston}, \tag{3.1}$$

and

$$P_{PTO} = -F_{PTO} \dot{X}_{rel}, \tag{3.2}$$

[55] where:

F_{PTO} = Force from the PTO (units)

Δp_{piston} = Differential pressure across the piston

A_{piston} = Surface area of the piston face interacting with the sea water

P_{PTO} = Power output of the PTO

$\dot{X}_{rel}$ = Velocity of the piston relative to the spar.

The power and force of the PTO were critical to the dynamic analysis, representing the power extracted by the wave pump and the force acting between the float and spar buoys. Using these values, the relative motion can be determined, which was instrumental in validating the WEC-Sim model with field data of relative motion. By including the hydraulic PTO component, an accurate calculation of the piston relative motion can be achieved. The equation for calculating the pump flow rate was included in section 3.6.

3.3 Generating Geometry Files

The wave pump SolidWorks CAD design files [13] were used to develop geometry files which could be used in the BEM analysis. Simplified versions of the spar and float buoy part files were created based on the wave pump device design files. If the heave plate connection rod were included in the geometry, the accuracy of the model would be increased. This is an opportunity to increase accuracy of the numerical model in future work.

The simplified float CAD file was created with its origin located where the waterline exists at equilibrium. This waterline was located five inches above the base of the float. The float was five feet in diameter, with an inner diameter of nine inches. The float was eighteen inches tall overall, with a radius on the external edge of five inches at the base.

The spar's origin and waterline location was located 44-inches from the its top. The simplified spar file was created by using a single cylinder with an outer diameter of 8.625-inches and a length of 228.5-inches. The heave plate was modeled as an additional cylinder at the spar base with a diameter of 36-inches and thickness of 1-inch.

The orientation of both parts in SolidWorks must align the Z coordinate axis with the upwards direction (or so that the Z coordinate aligns with the device's vertical axis in the water column). Both Solidworks part files were saved as STL type files. The SolidWorks STL file type must have the units saved in meters.

The CAD files for both the float and spar were then processed by the Meshmagick software [53], which transforms the SolidWorks generated STL file type into a ".nemoh" file type. This file type was a text file containing all the geometric information. This geometric information was organized in a triangular finite element mesh with X, Y, and Z coordinates (Figure 3.2).

3.4 BEM Analysis Using Capytaine and BEMIO

The WEC-Sim Reference Model 3 (RM3) example was used as the basis for the numerical model, since it was a two-body point absorber WEC similar to the wave pump device. Modifications were made throughout the RM3 example, to increase the model's similarity to the wave pump device. The RM3 example included both Capytaine and BEMIO code developed by the WEC-Sim team, which were also used as a basis for the wave pump numerical model.

Capytaine is a linear potential flow solver, determining the device's hydrodynamic re-

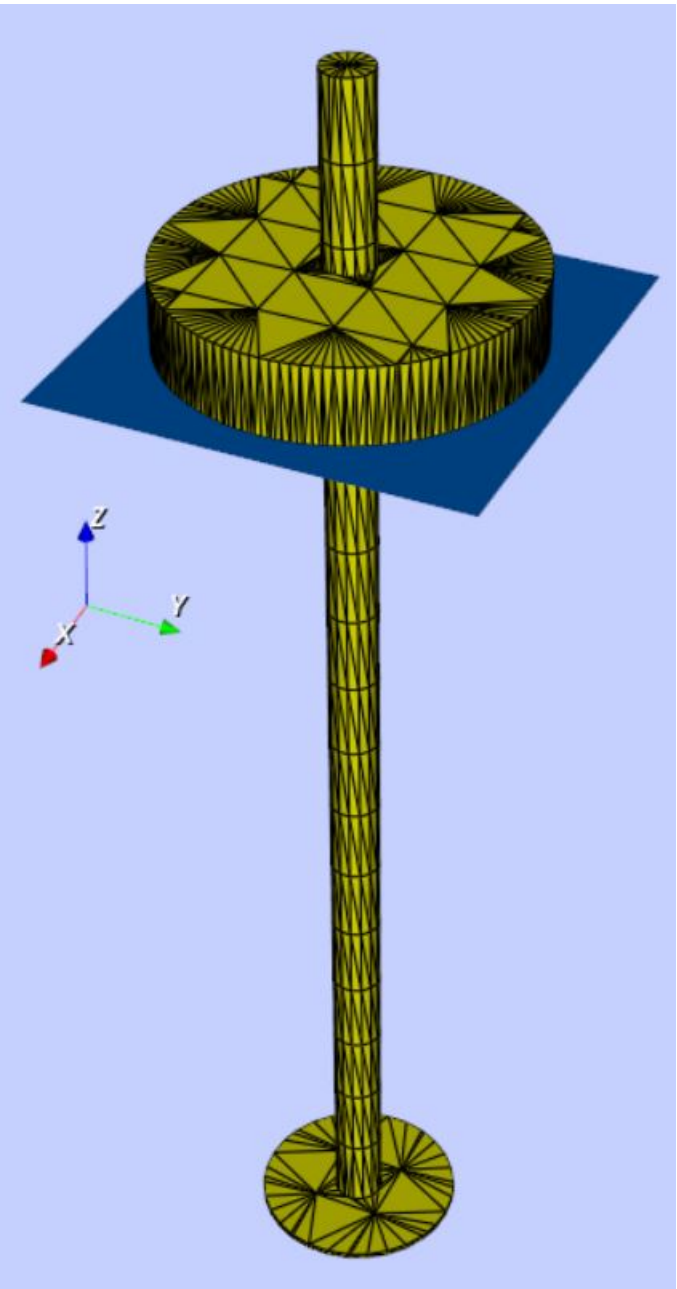

Figure 3.2: Meshmagick Viewer Showing the Float and Spar Meshes Combined, Waterplane Shown (for BEM analysis files were kept separate)

sponse in a variety of wave frequencies. In the RM3 Capytaine example code, few parameters were changed other than updating file and variable names. The geometry files of the wave pump were used instead of the RM3 files. The location of the center of gravity for both the float and spar were updated to reflect the wave pump. These values were relative to the

geometry files' origins or waterplane location. The float had a center of gravity location of 0.188m above the waterplane, and the spar had a center of gravity location of 2.110m below the waterplane.

The BEM analysis was completed over a range of wave frequencies, beginning at 0.02 $\frac{rad}{second}$ and ending with 10 $\frac{rad}{second}$, in 520 intervals throughout this range. This frequency range spans wave periods between 0.63 seconds and 314 seconds. Wave headings for the BEM analysis in Capytaine were set to zero in the Y and Z coordinate directions, so that the waves were traveling only along the X coordinate direction.

Water depth was set to the deep water assumption, where the water depth must be greater than half the wavelength [19]. This was an accurate assumption for the field deployment location, which requires wavelengths less than 20 meters to be considered deep water. Typical wavelengths in this region of the ocean were less than 20 meters [23]. Water density was set to $1025\frac{kg}{m^3}$, which is a standard ocean water density.

Given the simplified geometry of the wave pump when running in the Capytaine BEM program, the results took approximately two hours to complete with a 2.5GHz processing speed, 16GB RAM computer.

The results from the BEMIO Matlab script were shown here. The first figure Figure 3.3 Normalized Added Mass of the device in the various wave states were shown. For an accurate model, both the float and spar bodies should tend towards a constant value as the frequencies increase. Since both the float and spar tend towards a constant value in all three degrees of freedom, this indicates an accurate simulation. Normalized added mass, $\bar{A_{ij}}$, was unitless. Normalized added mass in heave for the float buoy was approximately equal to one for most of the frequency range. There appears to be an error for the float normalized added mass in heave at approximately $9\frac{rad}{s}$, where the values are negative. At this frequency, the wave periods are 0.7 seconds. Wave periods below 0.7 seconds are not used in the WEC-Sim simulations, which made this error not a concern. For the spar, it tends towards zero for the entire frequency range. The subscripts i and j for the normalized added mass value indicate

what values in the greater added mass matrix correspond to the directional motions: surge, heave, and pitch.

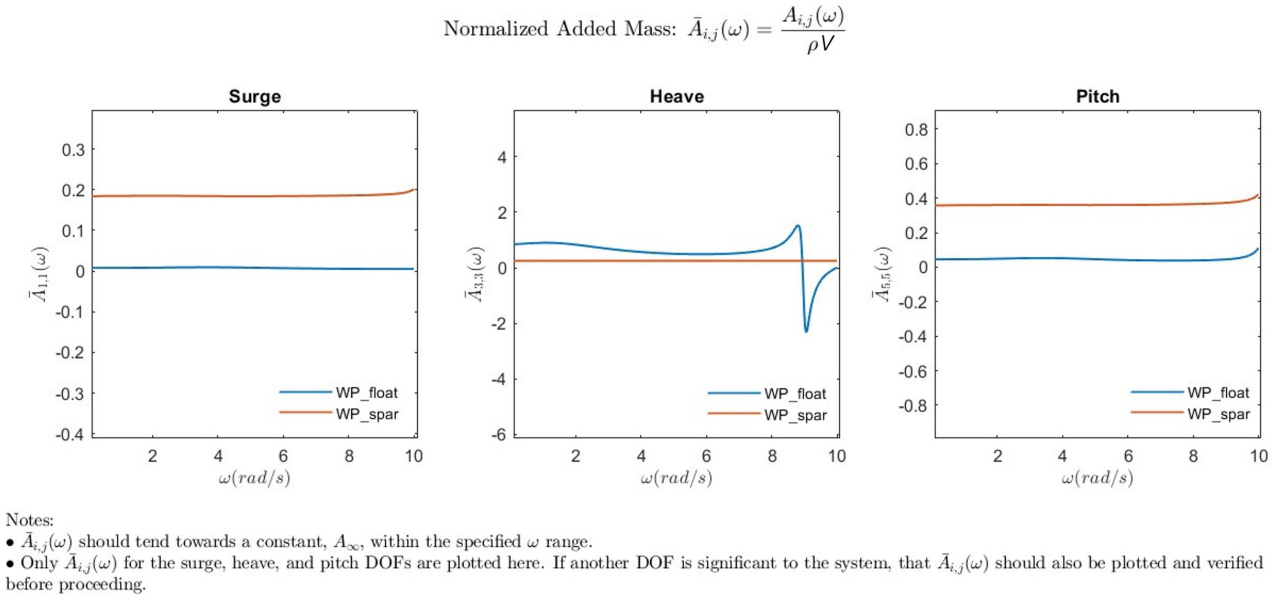

Figure 3.3: BEMIO normalized added mass result for wave pump device in various wave states.

The next result from BEMIO Figure 3.4 shows the system's normalized radiation damping result, $\bar{B_{ij}}$, which is dimensionless. For an accurate simulation, both damping terms should tend towards zero between 0.02 and 5.2 $\frac{rad}{second}$. The wave conditions measured during the field test were sampled at a rate of 2.5Hz. This sampling frequency negates the need to examine WEC-Sim generated wave frequencies smaller than 1.25Hz (7.9 $\frac{rad}{second}$) more closely when comparing the WEC-Sim data to the field data. The radiation damping response in heave motion was the most critical for this type of system. Focusing on the heave plot, the spar damping response remains at zero throughout the range of frequencies. This indicates that the spar was a poor radiation wave generator through the given range of frequencies. The float has a term which remains low, and spikes at approximately 0.7 second periods (8.9 $\frac{rad}{second}$). This indicates that the float will generate large radiation waves, the most of which

occurs at 0.7 second period waves.

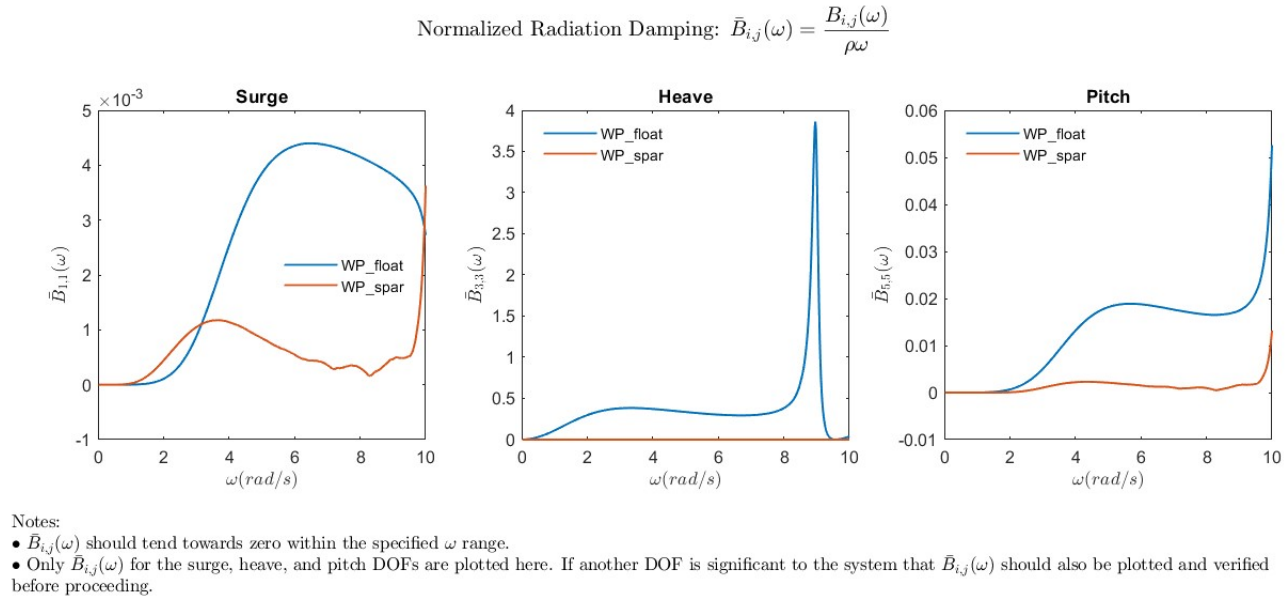

Notes:
• $\bar{B}_{i,j}(\omega)$ should tend towards zero within the specified ω range.
• Only $\bar{B}_{i,j}(\omega)$ for the surge, heave, and pitch DOFs are plotted here. If another DOF is significant to the system that $\bar{B}_{i,j}(\omega)$ should also be plotted and verified before proceeding.

Figure 3.4: BEMIO normalized radiation damping result for wave pump device in various wave states.

The normalized radiation impulse response was also an indicator for simulation accuracy. In Figure 3.5 radiation IRF $\bar{K}$ was dimensionless. The normalized radiation impulse responses for each body were plotted in the time domain, and must tend towards zero within the specified time. All results in each three plots do tend towards zero, indicating accurate radiation impulse response for modeling the device dynamics. The spar remains at zero or decays quicker than the float in all three instances of motion, which indicate smaller radiation response in wave forcing. The float has the largest magnitude radiation response, compared with surge or pitch. This indicated that the float has a large oscillatory response to radiation impulses, and will tend to create large relative motion between the float and spar in heave.

The normalized excitation impulse response indicates how the float and spar will behave in an excitation scenario. If each body was acted upon by an excitation force, the normalized response was shown decaying over time. $\bar{K}_i$ was the i-th component of the time- and

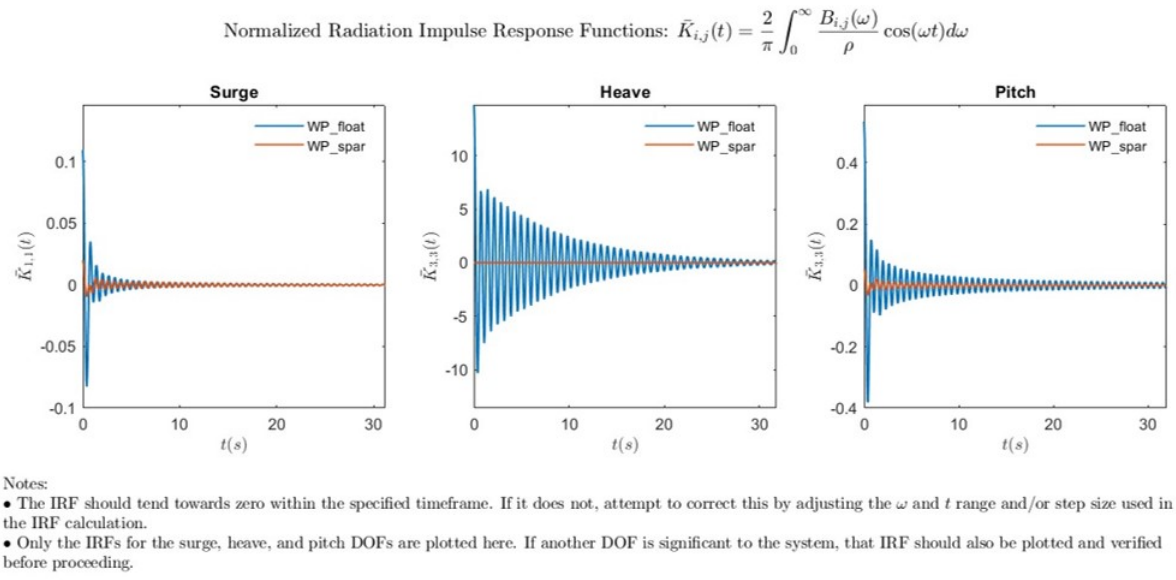

Figure 3.5: BEMIO normalized radiation impulse response for wave pump.

direction-dependent incident-wave-excitation force on each body (float or spar) per unit wave amplitude [31]. In Figure 3.6, both components should tend towards zero in the given time frame. In all three degrees of freedom, both components drop to zero within a short period of time, indicating accurate device dynamic modeling in the simulation. The expression shown on the figure representing normalized excitation impulse response, includes the term X_i. This term was the i-th component of the frequency- and direction-dependent complex transfer function for incident-wave excitation force on each body (float or spar) per unit wave amplitude [31].

3.5 Modified Reference Model 3 (RM3)

The WEC-Sim RM3 model was used as a basis for the wave pump numerical model. Several aspects of the RM3 model were changed to better reflect the wave pump design. The masses of the float and spar buoys, moments of inertia, and centers of gravity were shown in Table 3.1. The center of gravity was relative to the equilibrium waterline location.

CAD models of the float and spar were also uploaded for use in the simulation graphics.

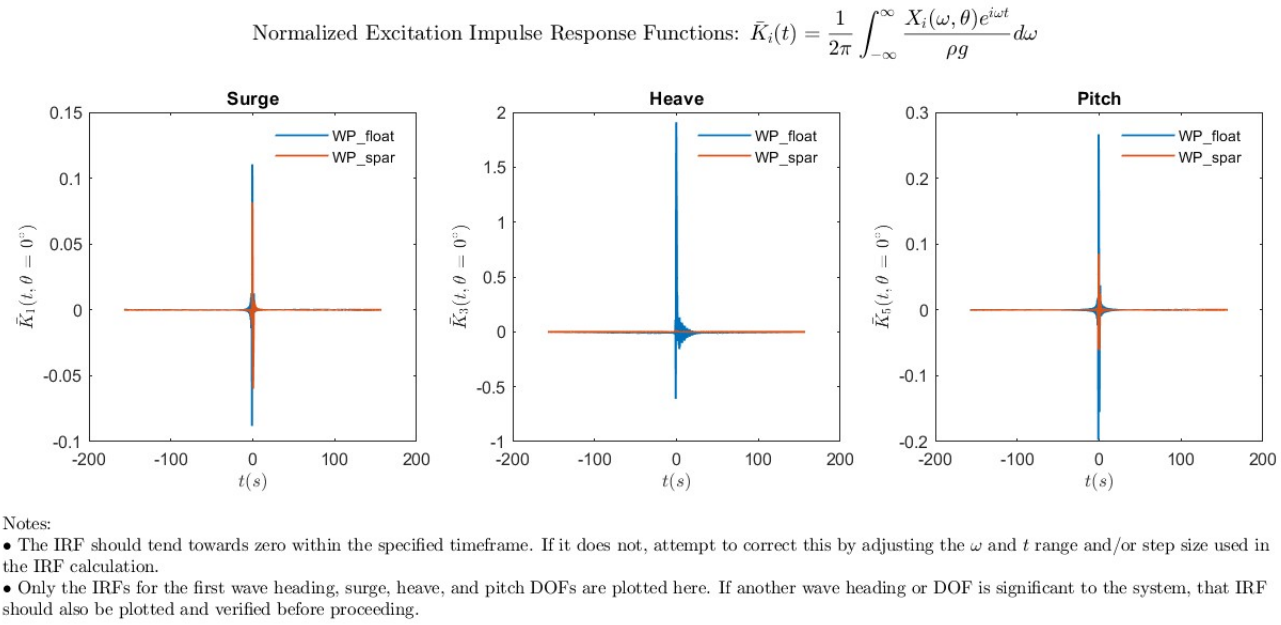

Figure 3.6: BEMIO normalized excitation impulse response for wave pump.

Table 3.1: Mass and Moments of Inertia for Float and Spar Buoys in WEC-Sim

Property	**Float Buoy**	**Spar Buoy**
Mass (kg)	95	173
Moments of Inertia: X, Y, Z ($\frac{kg}{m^2}$)	89, 89, 18	470, 470, 2.8
Center of Gravity (m)	+0.188	-2.110

These models need their origins located not on the waterplane, like for the BEM analysis, but at the center of gravity.

The mooring constraint chosen for the model was floating with six degrees of freedom. This was changed from the RM3, which had a constraint that was floating with three degrees of freedom. The three degrees of freedom constraint was defined as allowing motion in heave (Z-planar), surge (X-planar), and pitch (Y-rotational), and preventing motion in yaw (Z-rotational), roll (X-rotational), and sway (Y-planar). The six degree of freedom constraint was chosen because it most closely resembles how the device will be moored during a field deployment. The mooring during the field deployment was anticipated to have little wave response dynamic effect, which makes the six degree of freedom constraint a good choice.

In some cases, detailed further in chapter 8, a fixed spar constraint was utilized. The fixed spar constraint reduced simulation runtime and was consistent with minimal spar motion. However, the six degree of freedom constraint was the more accurate choice.

The highest level Simulink diagram for the float and spar was shown in Figure 3.7. The float and spar bodies were represented by the yellow boxes. The PTO or pump simulation blocks were shown by the blue and upper white box. The blue box was the standard translational PTO actuation block from the WEC-Sim library. The white box was modified to represent the wave pump device. The mooring constraint was the lower white box, and the green box represents the global reference frame for the model. The bodies, reference frame, PTO, and mooring constraint all remained standard given the RM3 setup or from the WEC-Sim library. The PTO-Sim block received some additional alterations, detailed in the next section.

3.6 Modified RM3 Hydraulic PTO

One of the WEC-Sim Advanced Features is PTO-Sim, accessed through the WEC-Sim Applications Repository. By utilizing the RM3 Hydraulic PTO example, modifications were made to more closely resemble the wave pump device. A simplistic diagram representing the wave pump device was shown in Figure 3.8. Where P represents pressure and Q represents flow rate at the indicated location. This simple diagram includes the two check valves and piston that comprise the pump.

The lower portion of the piston was filled with seawater, and the upper side of the piston was open to the atmosphere. The upper portion of the piston was removed from the Simulink model, since it was open to the atmosphere. The lower portion of the piston was characterized by:

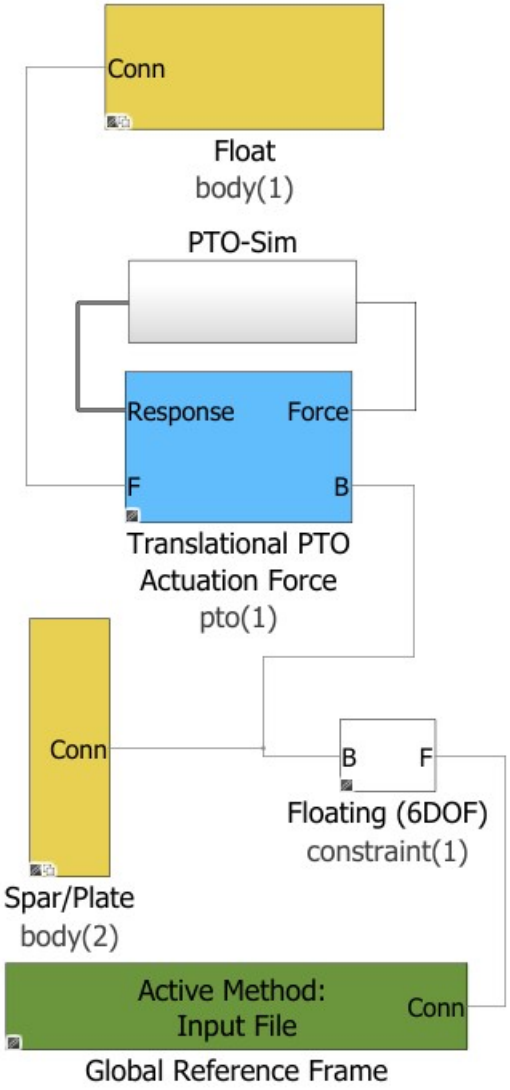

Figure 3.7: WEC-Sim Simulink model overview diagram for wave pump model.

$$\int_{-inf}^{inf} \frac{B(Q_{valves} - Q_{piston})}{x_{rel}A_{piston} + V_{piston}} dt = P_{piston}, \tag{3.3}$$

where:

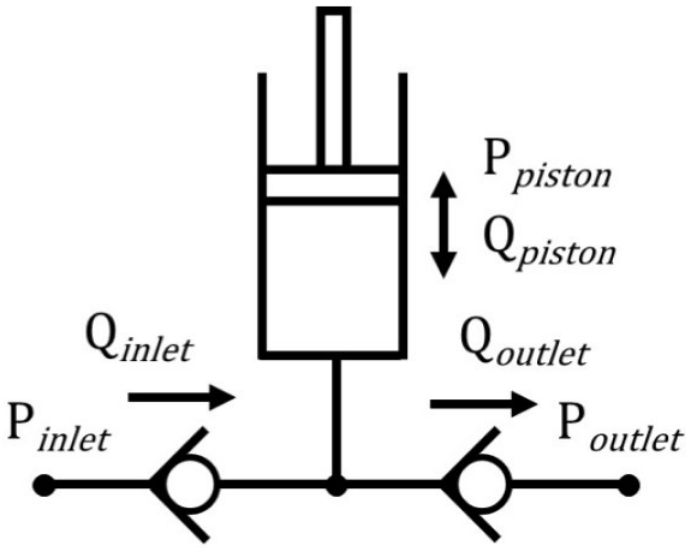

Figure 3.8: Simplified diagram of single piston pump operation with PTO variables

B = Bulk modulus of seawater

Q_{valves} = Flow rate through the check valves

Q_{piston} = Flow rate through the piston

x_{rel} = Position of the piston relative to the spar

A_{piston} = Surface area of the piston face interacting with the sea water

V_{piston} = Volume of the piston at neutral position

P_{piston} = Pressure in the piston's lower chamber.

In Equation 3.3, the hydraulic fluid was compressible; however in this application with the upper portion of the piston open to air, the fluid is not compressed. Consequently, the volume flow rate of the valves were characterized by:

$$Q_{valves} = Q_{inlet} - \mathrm{Q}_{outlet}, \tag{3.4}$$

where:

Q_{valves} = Flow rate through the check valves

Q_{inlet} = Flow rate through the inlet check valve

Q_{outlet} = Flow rate through the outlet check valve.

The volumetric flow rate through the piston was given by:

$$Q_{piston} = A_{piston}\dot{x}_{rel}, \tag{3.5}$$

where:

Q_{piston} = Flow rate through the piston

A_{piston} = Surface area of the piston face interacting with the sea water

$\dot{x}_{rel}$ = Velocity of the piston relative to the spar.

Volumetric flow rate through the inlet check valve was given by:

$$Q_{inlet} = C_d \times \left[tanh\left(k_2\left[(P_{in} - P_{pstn}) - \left(\frac{P_{max} + P_{min}}{2}\right)\right]\right)\left(\frac{A_{max} - A_{min}}{2}\right) + \left(A_{min} + \frac{A_{max} - A_{min}}{2}\right)\right] \times \sqrt{\frac{2(P_{in} - P_{pstn})tanh(k_1(P_{in} - P_{pstn})}{\rho}}. \tag{3.6}$$

The equations used to derive Equation 3.6 were the orifice equation and valve area equation as a variable area poppet valve [58], these are also used to develop the expression for flow through the outlet valve. For the outlet check valve, volumetric flow rate was:

$$Q_{outlet} = C_d \times \left[tanh\left(k_2\left[(P_{pstn} - P_{out}) - \left(\frac{P_{max} + P_{min}}{2}\right)\right]\right)\left(\frac{A_{max} - A_{min}}{2}\right) + \left(A_{min} + \frac{A_{max} - A_{min}}{2}\right)\right] \times \sqrt{\frac{2(P_{pstn} - P_{out})tanh(k_1(P_{pstn} - P_{out})}{\rho}} \tag{3.7}$$

In Equation 3.6 and Equation 3.7:

Q_{inlet} = Flow rate through the inlet check valve

Q_{outlet} = Flow rate through the outlet check valve

C_d = Flow coefficient

k_2 = Valve Coefficient

P_{inlet} = Pressure at the inlet valve

P_{outlet} = Pressure at the outlet valve

P_{piston} = Pressure in the piston's lower chamber

P_{min} = Cracking pressure of the valve, given by manufacturer

P_{max} = Approximately twice the value of valve cracking pressure

A_{max} = Valve cross-flow area when open

A_{min} = Valve area when closed

k_1 = Valve coefficient = 200

ρ = Density of seawater.

The valve coefficient, k_1, was expressed by:

$$k_2 = tanh^{-1}\left[\left(\frac{\dot{V}}{C_d A_{max}}\right)^2 \frac{\rho}{2}\frac{1}{P_{min}}\right]\frac{1}{P_{min}}, \tag{3.8}$$

where:

$\dot{V}$ = Volumetric flow rate of pump.

The Simulink diagram of the modified RM3 Hydraulic PTO contains these PTO equations.

Additional parameters needed to create an accurate model of the wave pump were included in Table 3.2:

Table 3.2: Parameters representing the wave pump device in WEC-Sim

Property	**Value**
Constant Pressure at Inlet (Pa)	24,000
Constant Pressure at Outlet (Pa)	10,055
Piston Area (m^2)	0.007
Bulk Modulus of Seawater (Pa)	2.34e9
Check Valve Discharge Coefficient	0.61
Check Valve Max. Area (m^2)	0.002165
Check Valve Min. Area (m^2)	1e-8
Pressure for Fully Open Valve (Pa)	17236.9
Valve Cracking Pressure (Pa)	3447.4

3.7 Preliminary Results

To determine whether the model was producing results that appeared reasonable and on the correct order of magnitude, regular wave conditions of 0.3m significant wave height, with a period of 4 seconds were selected. After the selection of these wave conditions, the model simulated the device dynamics and flow rate.

Figure 3.9 indicates the flow rate of the wave pump for the fixed spar constraint. The flow rate was instantaneous and shown for a thirty second simulation with a ten second ramp time. The outlet flow rate was shown in blue and the inlet flow rate was shown in orange. Upon reaching steady state, the outlet and inlet instantaneous flow rates were similar levels around 25gpm.

Figure 3.10 indicates the relative distance between the float and spar (also the piston motion) for the fixed spar constraint. Since the spar was fixed in this simulation, the relative motion tracks the motion of the float buoy. The float buoy was acting as a near-perfect wave follower, where it matches the height of the 0.3m waves. The peaks of each stroke were shown for reference.

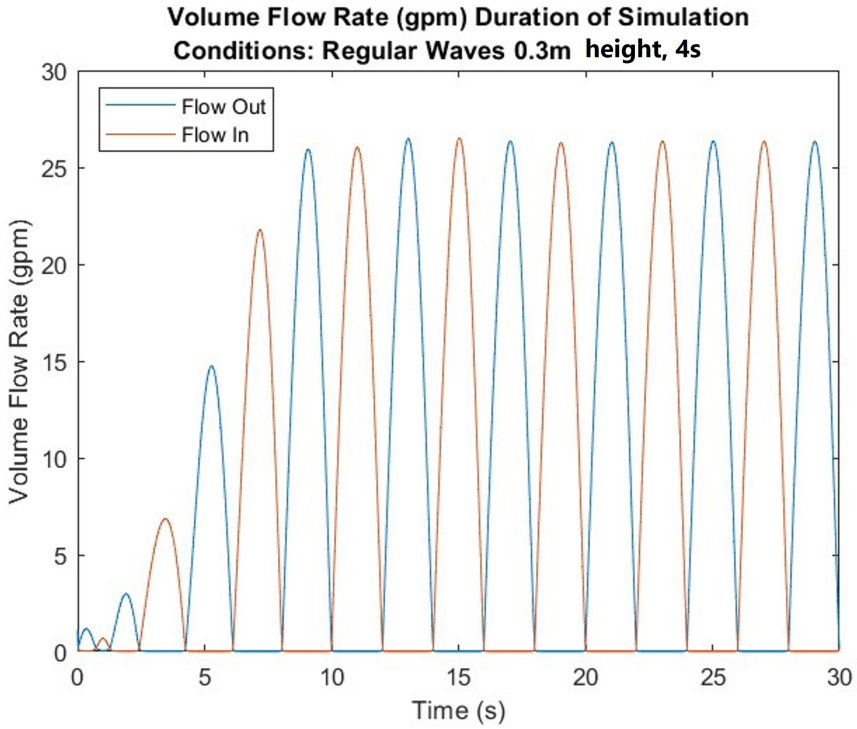

Figure 3.9: Example wave pump flow rate representation in regular wave state of 0.3m significant wave height with 4 second periods with fixed spar constraint.

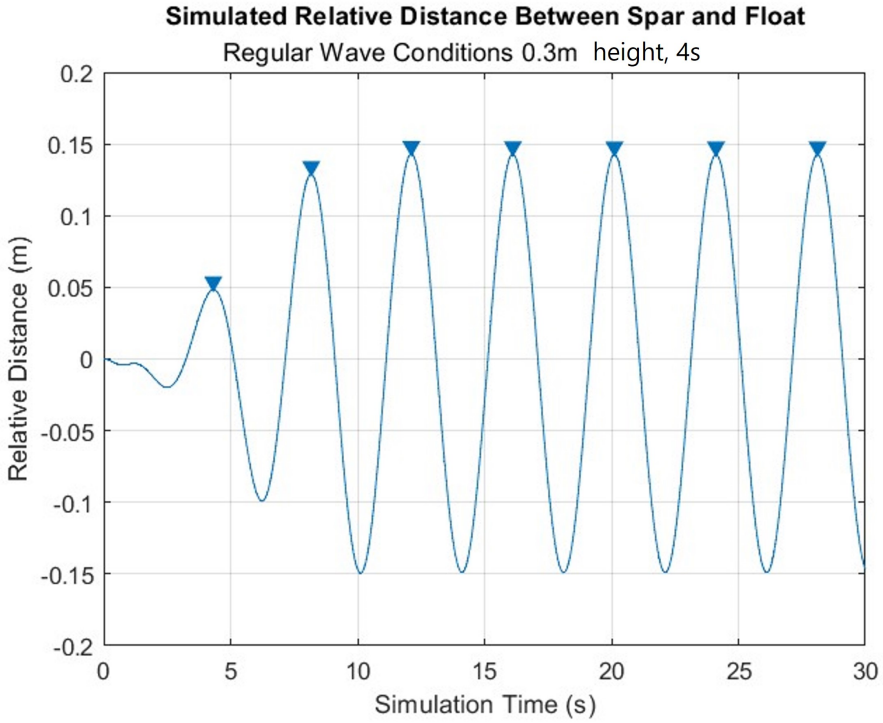

Figure 3.10: Example wave pump relative distance representation in regular wave state of 0.3m significant wave height with 4 second periods with fixed spar constraint.

CHAPTER 4

Device Upgrades

4.1 Overview

Device improvements were made prior to lab or field testing, to ensure that the wave pump would be able to survive ocean conditions for several weeks. The main motivations for these improvements included increased corrosion resistance, upgraded quality of data collection, and improved hydrodynamic stability. All three of these categories are obligatory for a well-functioning marine energy research device.

4.2 Hardware

One significant consideration for ocean-going equipment is cathodic corrosion. If metallic materials are used which are highly susceptible to corrosion, parts could break or degrade. This could cause a potential failure, or diminished operation, during an ocean field deployment. All hardware on the wave pump float which appeared to have corrosion were replaced. This included all rods, nuts, bolts, pins, and washers. These were replaced with marine grade stainless steel (316 Stainless Steel) by disassembling the wave pump device and then reassembling it (Figure 4.1), (Figure 4.2).

Locations where 316 Stainless Steel bolts came into contact with aluminum, plastic washers were used as an insulator to prevent corrosion. The springs used in conjunction with the physical constraint plates were not replaced with a marine grade steel because the existing

Figure 4.1: Wave pump float subassembly with corroded hardware removed.

Figure 4.2: Wave pump float subassembly with new 316 Stainless Steel hardware installed.

corrosion appeared superficial and unlikely to create a structural issue within a few weeks of ocean deployment.

Figure 4.3: Aluminum gantry at the top of the float buoy subassembly with new aluminum brackets retrofitted.

The L-Brackets on the aluminum frame had received some abrasion from a previous deployment, and those were replaced (Figure 4.3). The aluminum grade was 6105 and was anodized to prevent corrosion. In addition, the bracket hardware were also replaced with 316 Stainless Steel extruded nuts and bolts, and with plastic washers to act as insulators.

4.3 Underwater Electrical Connector

An underwater electrical connector was added onto the spar buoy. This addition to the wave pump device allows for more reliable data collection from the flow meter sensor. By sending the data to the DAQ module at the top of the spar, via the underwater electrical connector, the flow meter housing does not need to supply a power source or DAQ module for the sensor. It also was more reliable in preventing the data from being corrupted due to water intrusion. Additionally during the deployment, the entire data set can be retrieved from the DAQ module at the top of the spar and examined, to ensure high data quality throughout a field deployment.

To create this addition to the wave pump device, several steps were taken. First, a patch part was designed and then manufactured at a machine shop (Figure 4.4). This patch part was made of PVC, and was designed for the connector to mount onto it. Then the curved back surface was PVC cemented onto a drilled hole in the spar buoy. The connector cabling was routed up through the spar to the top of the buoy. The patch part was manufactured

Figure 4.4: Underwater electrical connector mounted to patch part, prior to adhesion to spar buoy.

using CAD files, and therefore a manufacturing drawing was not required.

The underwater electrical connector was purchased OTS from Birns Aquamate, part number: MCBH6M. The corresponding underwater cable and dummy plugs were also purchased. The cable was used to move the power and data between the flow meter sensor and the spar connector. The dummy plugs were used while the equipment remains in the lab to protect the connector pins.

The connector was first soldered onto a longer piece of cable which covers the length of the spar required, approximately ten feet (Figure 4.5). This cable was purchased OTS, and was six stranded and shielded. It was covered with a PVC conduit to protect the wire strands. Once the solder joint was completed with several layers of heatshrink to protect it, the entire length of cable was covered in several long pieces of heatshrink and conduit to protect the cable structurally and from water intrusion.

The connector was mounted to the patch piece with a nut and permanent thread-locker adhesive to prevent it from coming loose. A small, fiberglass piece at a 90 degree angle was secured to the inside of the cable to protect it, as well as bend the cable away from the

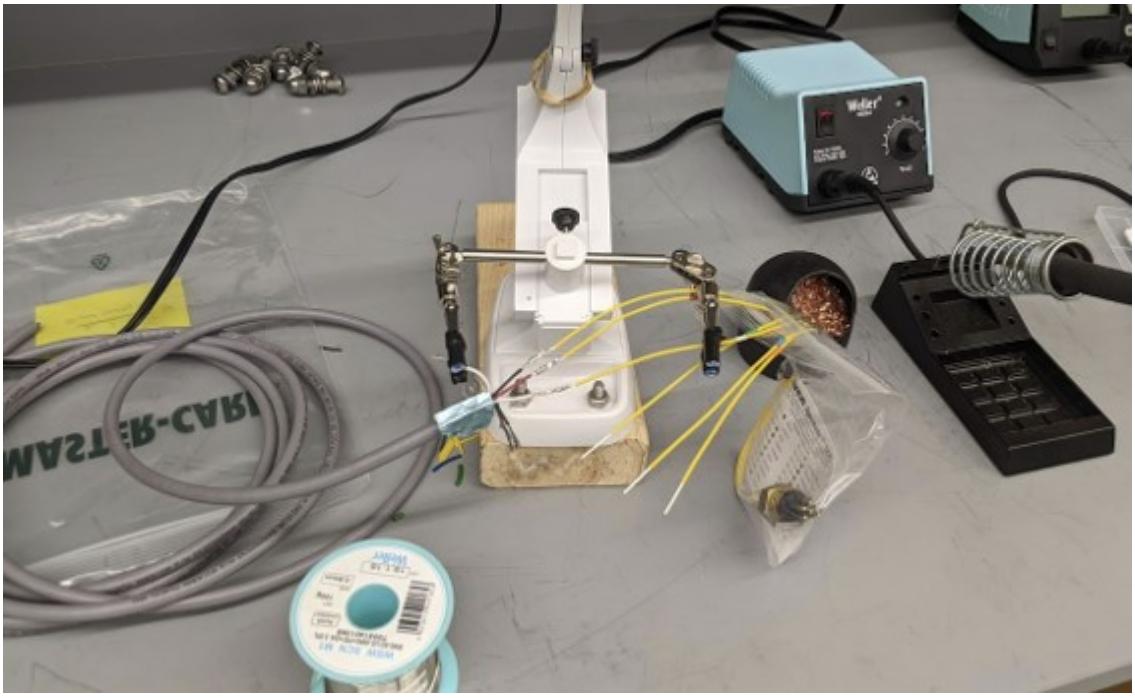

Figure 4.5: Soldering underwater electrical connector wires to OTS shielded cable to move data from underwater location along the spar to the top of the spary buoy where the DAQ module was located.

Figure 4.6: Underwater electrical connector cable routed to top of the spar buoy. Shown in picture by black cable.

inner PVC cylinder. The cable was routed up to the top of the spar (Figure 4.6). Next, the patch piece was PVC cemented to the spar using a cleaner, primer, and cement (Figure 4.7).

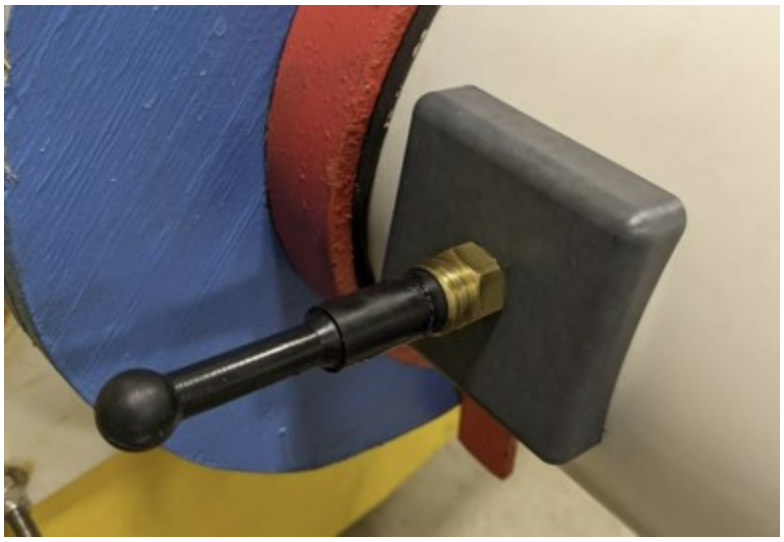

Figure 4.7: Underwater connector and patch piece subassembly fully assembled onto spar buoy.

Lastly, a silicone seal was added around the outside of the patch as a secondary waterproof seal.

Throughout the process of preparing the wave pump device for deployment, the electrical connector was tested using a multi-meter to ensure the wiring had no defects between the connector and the wires at the top of the spar.

4.4 3D Printed Flow Meter Housing Mounting Brackets

To securely attach the flow meter housing to the spar buoy, two brackets were 3D printed at the UNH Technical Services Center (Figure 4.8). These were designed to work with 316 Stainless Steel hose clamps which encompass the spar buoy and hold the brackets in place. This allows for adjustable placement of the flow meter housing. The hose clamps were lined with a neoprene foam to prevent slippage.

Two additional 316 SS hose clamps encircle the flow meter housing to securely attach it to the brackets (Figure 4.9). The brackets were printed using the densest available setting to discourage water retention. The brackets were comprised of polylactic acid plastic, and

Figure 4.8: Mounting brackets for flow meter housing installed onto spar buoy.

were designed with a lip at each end to prevent the flow meter housing from sliding out on either end. For a longterm deployment, PVC or Delrin or other similar material should be used in-lieu of 3D-printed polylactic acid. While these parts were sufficient for a short-term deployment, anything beyond a few days was not recommended for this material. Since these were manufactured using 3D printing software, a manufacturing drawing was not required.

4.5 Spar Top Plate Replacement

The plate at the top of the spar was replaced with a new design. The updated design was slightly larger. This allowed for an overhang for all four of the air vent ports at the top of the spar. These were critical for proper pump operation, however, they do pose a water intrusion risk. By designing the plate with an extended overhang, it will aid in preventing rain from intruding the air vents during an ocean deployment. The top plate also has a place for the DAQ module, lidar, and room for other small sensors to mount. The top plate has

Figure 4.9: Flow meter housing installed onto spar buoy.

a 316 Stainless Steel cable gland which routes the flow meter power and data cable to the DAQ module. This piece was made of marine grade HDPE to survive an ocean deployment. The Olsen Center at UNH manufactured the plate using water jet cutting (Figure 4.10). The manufacturing drawing for this part was included in Appendix A. The plate also required replacing the linear bearing for the piston in the center with a new linear bearing.

4.6 Built-In Ballast

Previous deployments of the wave pump required approximately thirty pounds of ballast [13] to achieve the hydrostatic stability for the system. The previous teams had used shackles around the heave plate pipe to attach the ballast. However, a built-in ballast solution would be more secure for a lengthier deployment.

Figure 4.10: Top plate of spar buoy with updated design for DAQ module and lidar mounts and enlarged overhangs to prevent water ingress.

An OTS steel pipe flange was purchased to act as this ballast. It weighed twenty-six pounds, and was covered with an anti-corrosion marine grade paint to prevent corrosion during an ocean deployment. This flange was added onto the aluminum end cap at the lower end of the spar, with extended bolts (Figure 4.11). Thirteen pounds of additional ballast were also used attached to the heave plate.

With the addition of this flange, the mounting hardware for the heave plate needed an adjustment. Two smaller bolts with a coupling nut were used for a blind mate of the heave plate pipe onto the aluminum end cap.

4.7 Lidar Target

The lidar sensor was mounted to the top plate facing upwards. This allows for the lidar cable to travel a short distance over the plate to the DAQ module to receive power and send data. However, the lidar sensor faces upwards, with nothing to register the relative distance

Figure 4.11: Ballast weight of twenty-six pounds incorporated directly onto spar buoy using OTS steel pipe flange, coated in marine-grade anti-corrosion paint.

between the spar and float. To bounce the laser signal off of an object, a lidar target was added to the float's aluminum frame.

The target was made of aluminum grade 6061 to prevent corrosion. It was a small, lightweight addition to the frame, to reduce changes to the float dynamics. It was secured to the aluminum frame using hardware designed for the extruded aluminum frame.

4.8 Waterproof Tests and Leak Repairs

During the first test of the wave pump in the UNH Engineering Tank on November 4th, 2022, a significant water leak within the main spar was detected. In a thirty minute interval, over

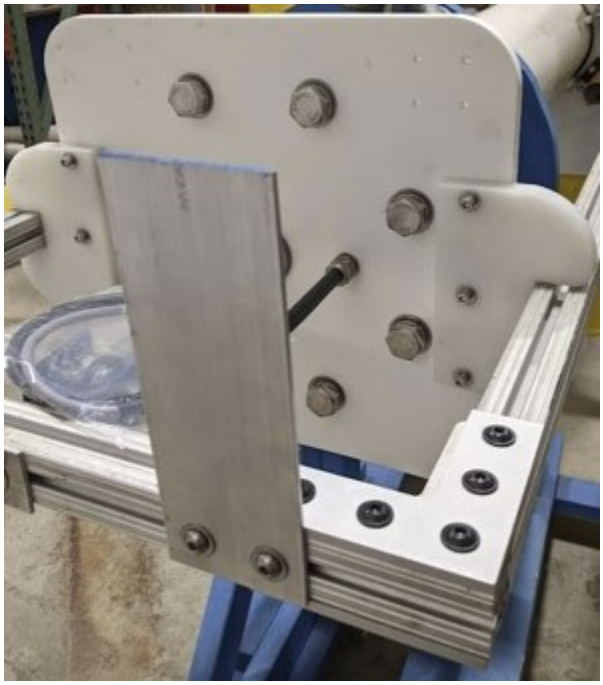

Figure 4.12: Aluminum lidar target mounted onto float buoy's aluminum gantry.

six gallons of water entered the main spar. This rate of water intrusion would be sufficient to significantly alter the device dynamics during an ocean deployment. To repair the leak, the device needed to be deconstructed, and potential leak paths for the device were individually tested.

The tests included testing the flange faces against the gaskets, the pipe flanges' radial sealing face along the main pump PVC, the inner PVC threaded coupling, the mid-point PVC coupling, and the pump's inlet and outlet PVC construction (Figure 4.13). The two HDPE plates in between the pipe flanges and gaskets were removed due to suspected gasket leaks.

In all the potential leak locations, only one leak path was determined. The pipe flanges' radial sealing faces (along the pump's main PVC segment) did not correctly adhere, and had created a pathway for water intrusion. The leak was patched with Marine Weld 8272 along the junction between the flange and pipe (Figure 4.14). Two layers were added and cured,

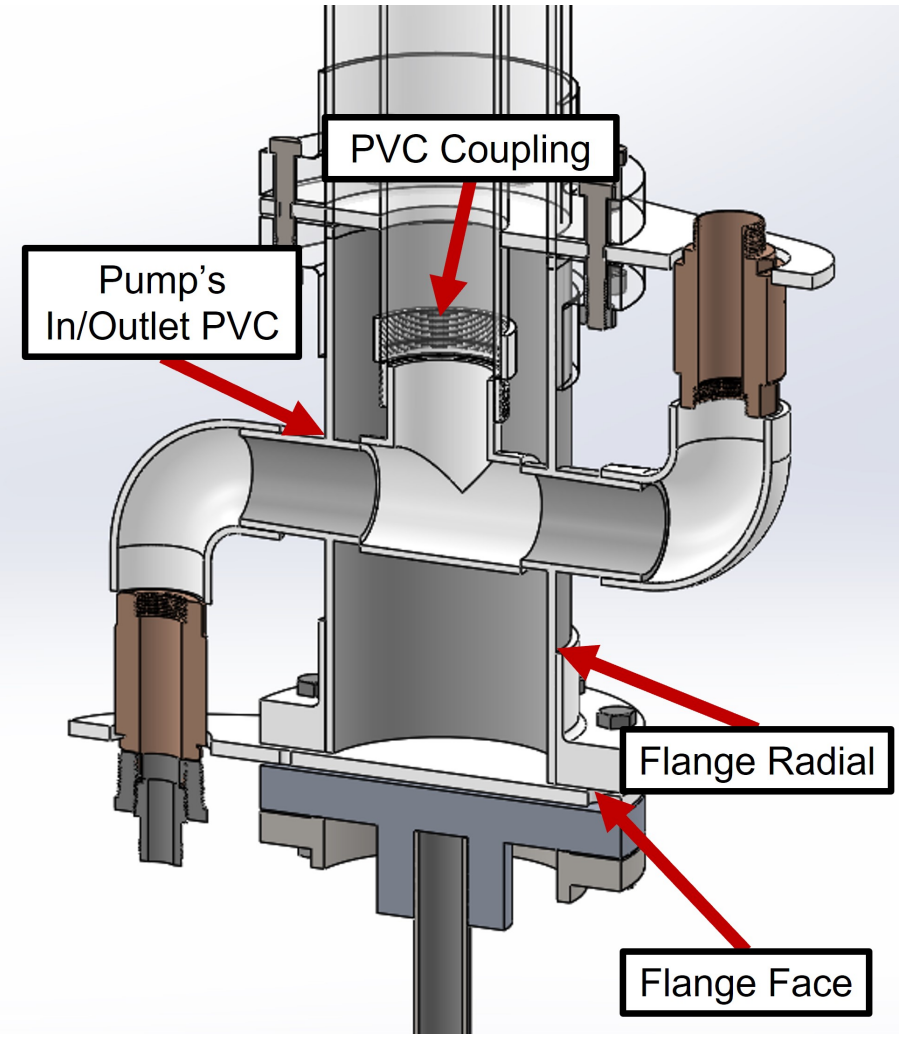

Figure 4.13: Cross-sectional view and diagram of pump section with potential leak paths identified. Diagram constructed utilizing CAD SolidWorks software.

before the entire device was reassembled and tested in the UNH Engineering Tank. After an interval of thirty minutes, there was no water found within the main spar. The piston head does appear to allow water flow past, so that the inner cylinder will fill with water. However, by using 3M 4200 FC on the inner spar pieces, this should prevent this water from entering the main spar during operation.

The torque specification on the bolts for the pipe flange attachments was forty foot-pounds, as designated on each flange.

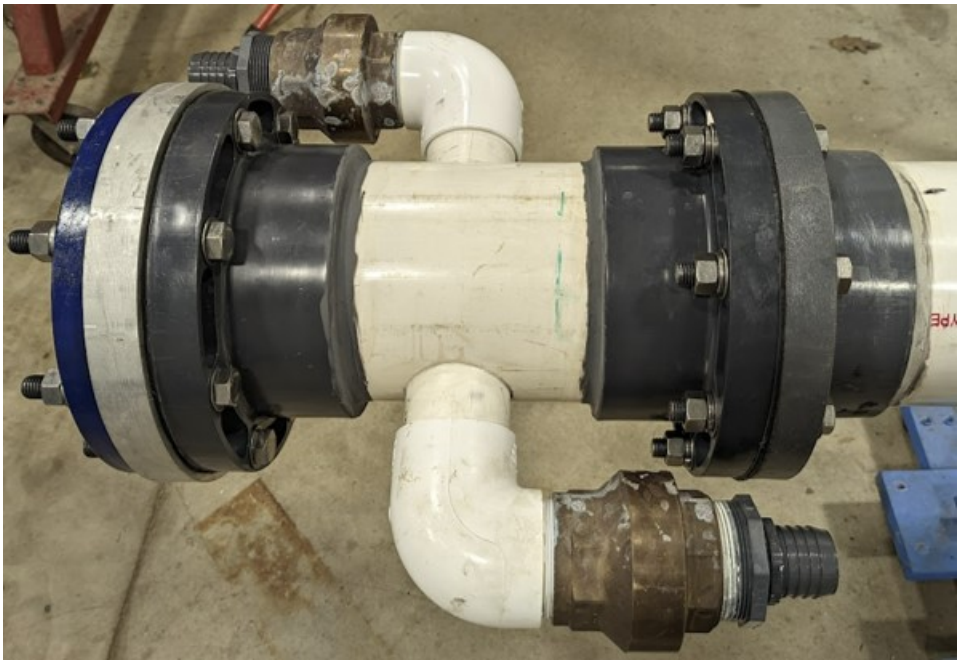

Figure 4.14: Device's pump section with marine weld applied and cured to repair leak.

4.9 Additional Flotation for Spar Buoy

After ensuring the leaks were repaired in the spar buoy, the waterline location of the spar was lower than the optimal position. To increase the waterline position, the spar required additional flotation. Calculating the difference between the current and optimal waterline locations resulted in determining the additional buoyancy required. Approximately 36 pounds of buoyancy were necessary to add to the spar.

A buoyancy collar was devised using flotation foam. The foam was molded using an 18-inch sonotube and a piece of 8-inch PVC pipe. The flotation foam used was $4\frac{lb}{ft^3}$ density, marine-grade polyurethane closed-cell pourable foam. The final result was painted with a marine based paint. The foam was held in place on the spar using neoprene and hose clamps. The manufacturing process and final result were shown in Figure 4.15.

Figure 4.15: Buoyancy collar developed to achieve ideal spar equilibrium location. Manufacturing process (left), and finished result installed on spar (right).

4.10 Pump Inlet and Outlet Hoses

The existing hoses for the pump were a typical pool type hose with many internal ridges. These ridges created additional losses in the pump flow, and were replaced by a hose with a smooth interior. These new hoses were cut to a two foot length for the inlet, and a eight foot length connecting the outlet to the flow meter sensor. The hose was constructed of clear PVC with an internal polyester structural element. The hoses were kept in place at the fittings by hose clamps. A 316 Stainless Steel mesh screen was added to the inlet hose to prevent bio-fouling of the pump. The mesh screen has openings of 0.075 inches to allow water to pass through, but prevent macroalgae from creating blockages within the pump. The mesh screen surrounded a volume of approximately one liter so that flow was less inhibited.

4.11 Marine Light for Float

The marine lights used in previous ocean deployments were no longer functioning so a replacement light was necessary. To meet the safety and NEPA requirements in the Biological

Assessment (see more detail in section 5.3), a Carmanah marine lantern, part number: M550 was purchased. A custom setting was requested for the flash pattern to meet the NEPA requirements, where the white light was on for 0.5 seconds, and was off for 1.5 seconds.

Figure 4.16: Carmanah Marine Lantern for Safety and NEPA Requirements

The bracket for mounting the marine light onto the float was modified to accommodate the new light.

CHAPTER 5

Experimental Design

5.1 Overview

An ocean field deployment of the wave pump device was a critical component of the development process. The deployment provided data to validate the numerical model. Additionally, the data from the ocean field deployment revealed device performance characteristics, exhibited its functionality in its intended environment, and revealed instances for design improvement. The plan for the ocean field deployment, laboratory tests, instrumentation selection and calibration, and the DAQ module design and manufacture are included in this section.

5.2 Site Conditions

The Isles of Shoals is an archipelago of nine islands off the coasts of Maine and New Hampshire. One of the islands, Appledore, is home to the Shoals Marine Laboratory, which is jointly run by UNH and Cornell University. From the UNH pier in New Castle, NH to the dock on Appledore Island is approximately seven miles [15].

The mooring field at Appledore Island, ME was selected as the ocean field test site for the wave pump because of the convenience of the moorings already installed. The team's familiarity with the location, vessel ability to travel to the island, and facilities on the island all made it the right choice for the field test. The deployment location was near to shore, and the radar tower maintained by SML has an Internet connected camera. This webcam

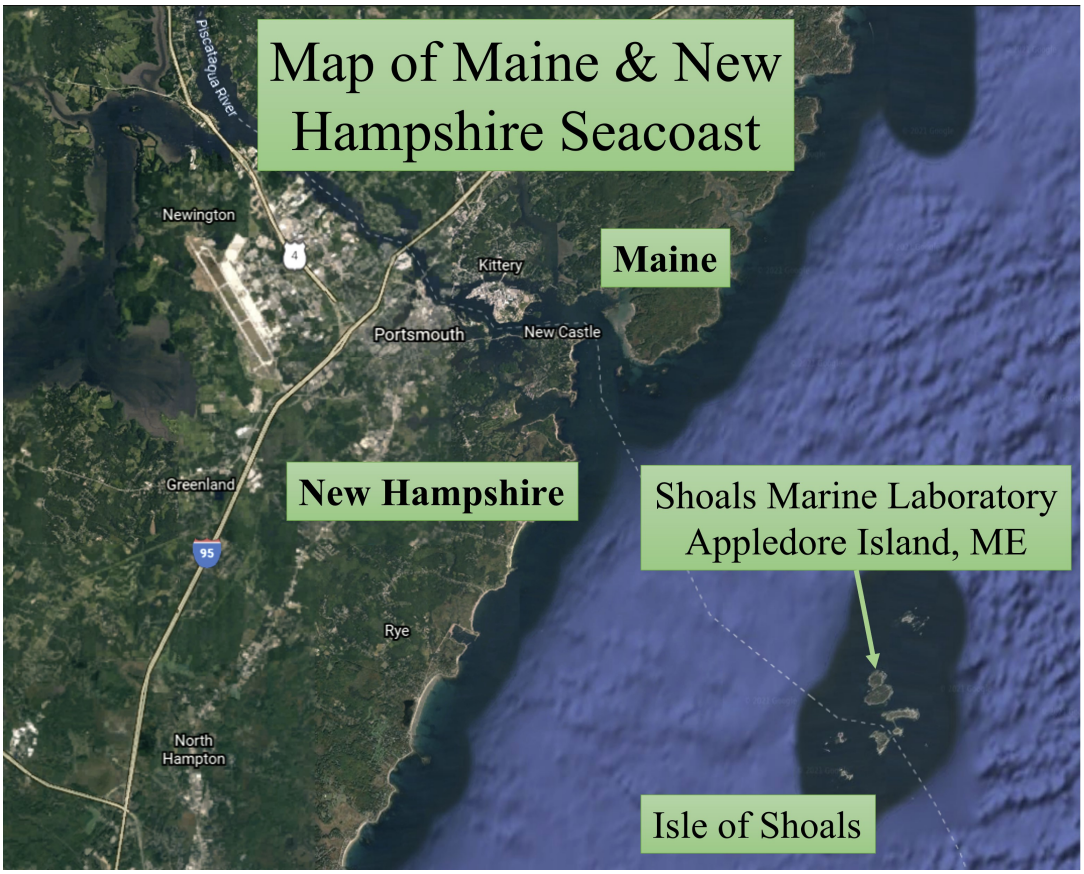

Figure 5.1: Map of Maine and New Hampshire coast with Isles of Shoals shown [15].

allowed for visual monitoring of the wave pump and Sofar Spotter buoy during deployment.

The water depth at the mooring site was twenty-five feet deep in MLLW according to the NOAA navigational chart (Figure 5.2), however SML divers report a depth of thirty-seven feet at MLLW [54]. Given the equilibrium depth of the buoy was approximately sixteen feet, there was open water beneath the device between approximately nine to twenty-one feet. This depth was sufficient for normal device operation given the wave heights at the location. Wave conditions at the Appledore mooring field during March were significant wave heights of approximately 1.2 meters, and up to 3.0 meters with periods of 3 to 5 seconds. These conditions were roughly estimated from the nearby Jeffrey's Ledge NOAA buoy data, which has been shown to be a good estimate of wave conditions at the Appledore site [14] [43]. Extensive Sea Surface Temperature (SST) and salinity data taken at another nearby

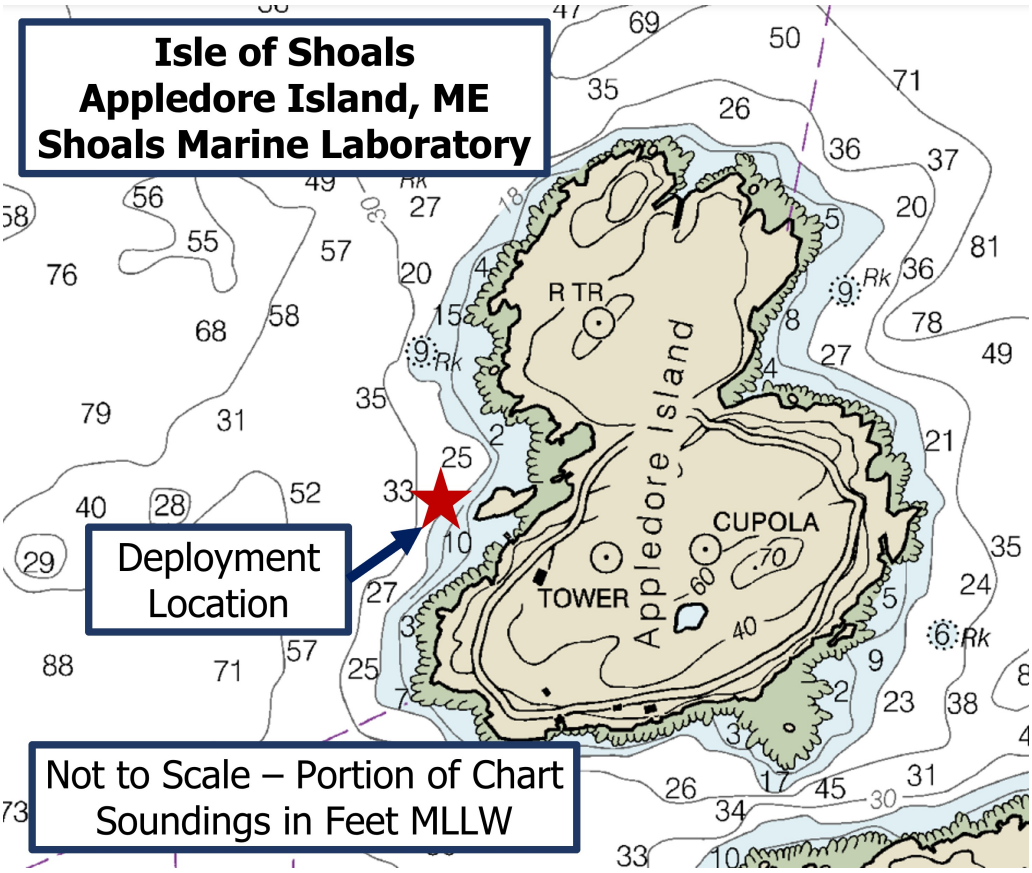

Figure 5.2: Subset of NOAA Chart 13283 containing Appledore Island [48].

location, the UNH Open Ocean Aquaculture (OOA) site were a close estimate of conditions at the Appledore mooring field. During March the average SST in 2009 was measured as 2.0°C. The average salinity from 2001 to 2008 at the surface during March was approximately 31 ppt [27].

5.3 Biological Assessment, NEPA Consultation, and Safety Considerations

Prior to conducting any in-field operations, a Biological Assessment and NEPA consultation were required. To produce the Biological Assessment, a document detailing the project was compiled. Then an environmental consultant was employed to complete a full Biological Assessment document. This document included relevant species in the project area, and any potential effects upon them due to the project. Using the BA as reference, the National

Marine Fisheries Service (NMFS) and US Fish and Wildlife Service (FWS) were consulted by the DOE on behalf of the project team. All parties agreed that 'No Effect' or 'Discountable Effects' were expected from the project activities upon species of interest in the area.

Since the device was moored, applicable safety regulations were evaluated. Considering US Coast Guard Navigation Rules and Regulations Rule 30 for a vessel at anchor [65], a flashing white light source designed for the marine environment was mounted on top of the float buoy. The flashing white light was also in accordance with concerns from Fisheries and Wildlife Service personnel, to prevent endangerment of birds. The flashing white light would follow the pattern: on for 0.5 seconds, off for 1.5 seconds on repeat. The light was mounted onto the float buoy of the wave pump device before it left the dock, and was activated aboard the R/V Gulf Challenger. The light automatically turned on at night.

To minimize potential collisions with marine mammals while in transit, the vessel traveled at a maximum speed of 10 knots. In addition, a crew member served as a dedicated spotter during each transit. Daily visual monitoring to ensure the device remained on the mooring was conducted by UNH personnel utilizing the Appledore webcam maintained by the SML staff.

5.4 Test Plan

The objective for the field test was to collect up to fourteen days of data on the device's volumetric flow rate from the outlet pipe, the device's relative motion stroke length, and nearby wave conditions. The flow rate and relative distance data were stored onboard the device, and retrieved throughout the deployment to ensure the device was operating normally. The wave pump was moored on the #5 location indicated on Figure 5.3, and the wave condition monitor buoy was moored on the #6 location.

The wave pump was outfitted with instrumentation to record the volume flow rate of water pumped. The relative motion of the float and spar was measured using a lidar sensor

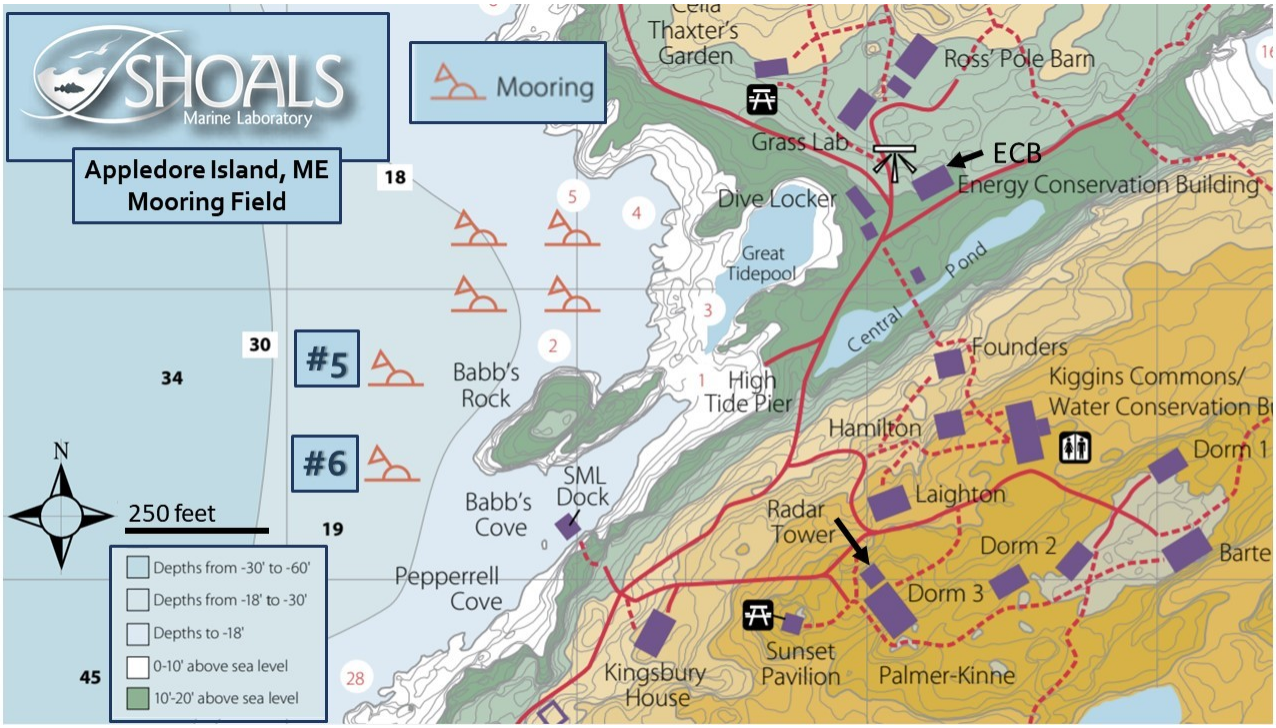

Figure 5.3: Appledore Island, ME mooring field diagram with #5 and #6 moorings indicated for field deployment [9].

mounted at the top of the spar buoy.

Clocks were used with each sensor to record time series data, and these were reset every twenty minutes with an accurate GPS time. This data was recorded on the device. A Sofar Spotter buoy was moored nearby which recorded the significant wave height, period, direction, and sea surface temperature. Additional environmental monitoring included two cameras mounted to the device, and two hydrophones on a mooring approximately three-hundred-feet away, and an on-shore webcam observing the deployment area.

Test standard IEC TS 62600-103 [26] was utilized as a reference for designing this test plan, where elements of Stage 3 (first field trials) planning were incorporated when deemed appropriate. The device scale was chosen based upon available materials for the project, and future work may include calculating a larger scaled version for commercial applications. The goal of this field test was to acquire data to assess device performance, and not necessarily for device survivability. Testing the device in the most extreme wind and wave conditions

in not part of the test objectives and may be included in future work. Due to utilizing the SML mooring, the device does not yet have its own entire mooring design completed and analyzing the mooring loads of the device was not part of this test's objectives. Nevertheless, both the test configuration and future moorings will use horizontal line attachments to allow free vertical motion of the float.

Temperature of the water being pumped by the device was not be measured.

Conditions experienced by the buoy were not expected to exceed wave heights of two meters. Weather forecasting of wave conditions informed the deployment and retrieval dates of the buoy.

5.4.1 Test Equipment

- Wave powered water pump device, heave plate, and ballast
- UNH Jere A Chase Engineering Tank (engineering tank) facility
- Mooring hardware (including rope with metal eyes and shackles, 316SS)
- Instrumentation – see detailed equipment specifications in section 5.6
- R/V Gulf Challenger, crane on the pier
- UNH CCOM truck, trailer
- UNH Jere A Chase facility's forklift

5.4.2 Test Phases

Calibrate Flow Meter Attached a hose to the fully assembled flow meter and set up a container to capture the outflow. Set the hose flow to a steady state and record the flow meter data. Measure the rate to fill the container co-currently. Use a range of flow rates to ensure good quality of calibration. Repeat after field test to verify calibration remains accurate.

Stage Gate 1: Calibration of Flow Meter produces repeatable results.

Water Intrusion Test of Flow Meter Housing Test flow meter in its completed waterproof housing by submerging in engineering tank to a minimum depth of 2m for a minimum of 24 hours.

Stage Gate 2: Flow Meter Housing remains free of water intrusion at conclusion of test.

Bench Test Instrumentation and Record Sample Data With all instrumentation outfitted to device and operating, record sample data at the bench. Artificially move float if able. Analyze data for correctness.

Stage Gate 3: All instrumentation worked as expected, sample data appeared accurate, GPS set time on sensor clocks every twenty-minutes without errors.

Tank Test Device with Instrumentation, Record Sample Data and Ballast With all instrumentation outfitted to device and operating, lift into engineering tank using crane. Outfit with appropriate ballast, and record amount of weight used. Record a sample of data and analyze for correctness. Calculate correction to ballast for saltwater deployment.

Stage Gate 5: All instrumentation worked as expected, sample data appeared accurate, no water intrusion observed on device, and ballast was approximately 30lbs.

Tank Test with Simulated Waves – Final System Check Repeat same test as above and add additional simulated waves by moving float artificially up and down using dock generated waves. Record sample of data and analyze for correctness.

Stage Gate 6: All instrumentation works as expected, sample data appears accurate, no water intrusion observed on device.

Field Test at Appledore Island Mooring Site Deploy fully outfitted device on mooring at Appledore Island, with Sofar Spotter buoy nearby for a period of 1-14 days. Monitor data

in real time for accuracy. Followed detailed process included in chapter 6 for field test.

5.5 Data Collection and Sampling Plan

5.5.1 File Storage Locations

All wave pump data were stored in the DAQ module at the top of the wave pump spar. The flow meter measured the volumetric flow rate from the device outlet pipe in gallons per minute. The relative distance was measured between the top of the spar buoy and the lidar target at the top of the float buoy's gantry by the lidar sensor. The GPS recorded accurate time series information within the main device DAQ module. The GPS had an accuracy of approximately ± 0.012 seconds for every twenty-minute data file.

Sofar Spotter buoy measured significant wave height, peak wave period, mean period, and sea surface temperature. The Sofar Spotter buoy was equipped with a GPS clock for accurate time series recording. Onboard processing of wave spectra was performed every 30 minutes. Data was stored on the buoy and processed data was uploaded to Spotter Dashboard via satellite link. Wave peak and mean direction, as well as wind speed and direction were recorded as reference information about the wave field. Pre-deployment checks on Sofar buoy were performed prior to deployment according to manufacturer instructions.

5.5.2 Sampling Techniques

Volumetric flow rate and relative motion were sampled at a rate of 1Hz and 59Hz respectively. Time series were recorded using the Arduino clock, powered by a Lithium coin cell battery. Every twenty minutes, the GPS clock in the main DAQ module reset each sensor clock, to increase timing accuracy and reduce drift to a maximum of ± 0.012 seconds. Sofar Spotter buoy collects data at a rate of 2.5Hz. Processed data was sent via satellite hourly. GPS location and time were also recorded.

5.5.3 Sample Size

The sample size varied for the volumetric flow rate and relative motion data depending upon the length of the deployment. Data storage cards of 16GB were installed into the DAQ module microSD card board to account for significantly more than 14 days of deployment. Each twenty-minute data file comprised approximately 1400 KB. Sofar Spotter buoy has a 16GB data storage card included on the buoy and sends processed data hourly via satellite link.

5.5.4 System Monitoring

Throughout the deployment, the microSD card was swapped out of the DAQ module on the device to monitor the data collection process. The data was evaluated to determine whether all the instrumentation and the device were operating normally during deployment. The wave pump device and Sofar Spotter buoy was visually monitored in real time by utilizing the Appledore webcam maintained by SML staff. This webcam was accessible via Internet, and panned to the mooring field once every minute.

5.6 Instrumentation Technical Specification Summary

Flow Meter - Digiten FL-1608 2" Water Flow Meter with Hall Sensor

- Measuring range: 10-200L/min (2.6-53gpm) ±5%
- Maximum current: 15mA (DC 5V)
- Working voltage range: DC 5-18V
- Load capacity: <10mA (DC 5V)
- Pressure rating: <1.75MPa (253psi, equivalent of 170m water depth, was deployed at roughly 2m water depth)

Garmin Lidar-Lite v3HP – High-speed Optical Distance Measurement Sensor

- Waterproof with IPX7 rating
- Range: 5cm to 40m
- Resolution: 1cm ± 2.5 to 5cm
- Working voltage range: 4.75-6V
- Current: 65mA idle, 85mA during data collection

Sofar Spotter Buoy

- Solar powered, 5x 2Watt, 6V solar panels
- Iridium SBD Satellite link
- Lithium Battery Included: 11,200mAh, 3.7V
- Wave period range: 30s to 1s
- Sampling rate: 2.5Hz
- Wave displacement accuracy: ± 2cm
- 12 lbs (excluding ballast chain), 16" X 12"
- Temperature accuracy: ± 0.1°C

Custom-Built DAQ Module Comprised of Arduino Uno, microSD storage boards, GPS clock, power management boards, lithium-ion batteries, and solar panels. Capable of storing data with time series accurate to ±0.012 seconds every twenty minutes. GPS clock consisted of an Adafruit Expansion Board compatible with Arduino Uno.

Reolink Argus 3 Pro Video Cameras The purpose of the video cameras was to observe the wave pump and its surroundings during the field deployment. They were located at the top of the aluminum structure attached to the float buoy. The cameras were manufactured

by Reolink and were Argus 3 Pros, installed with solar panels for power and 128GB on-board memory cards for storage. These cameras were motion activated, and did not record continuously.

Sound Trap ST500 Hydrophones The Sound Trap ST500 hydrophones were used to record sound in the mooring field throughout the field deployment. They were located three to four meters underwater on the same mooring as the Sofar Spotter buoy. These were set to record continuously at 144kHz.

5.7 Flow Meter Housing Design

The flow meter sensor was an off-the-shelf, Digiten 2" water flow meter with a hall effect sensor. Its internal passage way was rated to withstand a water pressure at 170m depth; however, its exterior and wiring were not leak proof. An additional housing surrounding the flow meter was required for the field deployment. The flow meter, in its housing, was mounted alongside the spar buoy approximately two meters underwater. It was connected to the output hose of the wave pump device, and measured the flow rate output of the pump.

5.7.1 Flow Meter Housing CAD Design

Designing the housing for the flow meter required two main objectives: keep the exterior of the flow meter dry and transfer the data safely to the DAQ module. Several prototypes were designed, manufactured, and tested. The final design was included here. It was composed of off-the-shelf PVC parts, an underwater electrical connector, and 3M Marine 4200 FC polyurethane. Limited machining was done on the end caps for the flow meter to pass through and for the electrical connector. The CAD design of the flow meter was shown in Figure 5.4. The overall length of the flow meter housing was approximately eight inches. The pipe fittings on either end allow for quick connection to hose and the watertight seal.

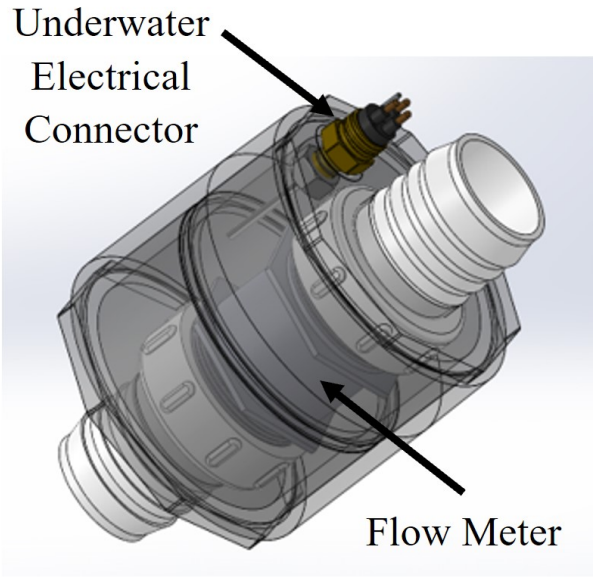

Figure 5.4: Custom designed flow meter housing assembly shown in CAD SolidWorks software.

5.7.2 Flow Meter Housing Manufacturing

The manufacturing process for the flow meter housing was comprised of three main steps. The first step required machining of the end cap PVC pieces for the hose fittings and the underwater electrical connector. Once these pieces were machined, the underwater connector was installed into one port, and a bolt with an O-ring was installed into the other as a plug (Figure 5.5).

Next, the hose fittings were installed onto the flow meter using the polyurethane and allowed to cure overnight. Additional polyurethane was applied to any gaps or bubbles the next day, and was cured for an additional twenty-four hours.

The wires between the connector and the flow meter were then soldered together. The underwater connector was from Birns Aquamate's MCIL line and has six pins. Pins 1, 3, and 5 were used from the connector to connect to the flow meter's ground, power, and data lines. Pin 1 from the connector was soldered to the flow meter's ground wire. Pin 3 from the connector was soldered to the flow meter's power wire. And Pin 5 from the connector was

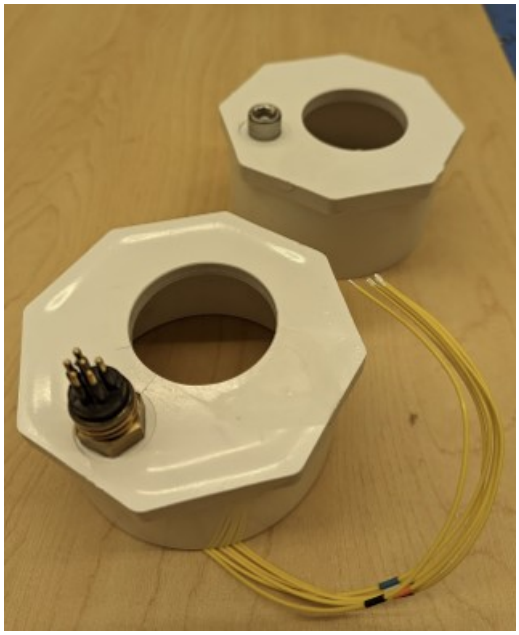

Figure 5.5: Flow meter housing manufacturing process: step 1

soldered to the flow meter's data wire. These connections were secured with several layers of heat shrink to prevent electrical shorts (Figure 5.6). A plug was placed over the underwater connector to protect its contacts prior to deployment.

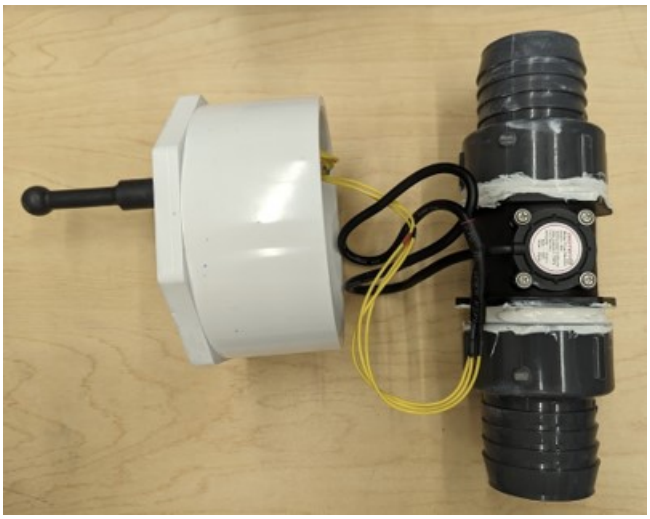

Figure 5.6: Flow meter housing manufacturing process: step 2

The final steps of the assembly process included sealing the end caps to the housing. The flow meter and fittings were sealed to the connector end cap using polyurethane around the

interior and exterior of the fitting junction. Polyurethane was then applied to the PVC end cap with the connector and the housing was placed onto it with the flow meter inside. Next the last end cap with polyurethane applied was placed into the other end of the housing. The entire assembly was placed in a hydraulic press until contact was made with the sealing faces of both hose fittings. The assembly cured for twenty-four hours, then another layer of polyurethane was applied to all the exterior sealing surfaces and allowed to cure. The final assembly is shown in Figure 5.7.

Figure 5.7: Flow meter housing manufacturing process: step 3

5.7.3 Waterproof Testing Flow Meter Housing

The custom-designed and built housing for the flow meter was tested for its impermeability. The housing assembly was weighed before and after submergence in water, and any additional mass was inferred to be water intrusion. The weight of the flow meter in its housing without

any hoses or cable attached was 3.253 pounds. It was submerged with a weight on a rope into the engineering tank to a depth of four meters (or twelve feet). This was twice the depth the flow meter was expected to survive during the field deployment. After seventy-two hours at depth in the tank, it was removed and carefully dried. A fan was used to dry the interior water passageway of the flow meter assembly after the test. The weight remained nearly the same at 3.259 pounds. A slight gain of 0.006 pounds was attributed to the 3M 4200 FC epoxy completely moisture-curing in the tank. The epoxy also discolored slightly due to this effect. This test confirmed the housing was watertight.

5.8 DAQ Module Design and Manufacture

The DAQ module was designed and built to accurately record the sensor data of the wave pump. It was housed in a waterproof box, purchased OTS. Modifications were made to the box to accommodate waterproof cable connections through the exterior for the lidar data, flow meter data, and solar panel cables. The total weight of the DAQ module was 7.2 pounds. SolidWorks CAD software was used to design the layout of the DAQ module, and plan the necessary hardware and spatial requirements (Figure 5.8).

Power The DAQ module was powered by using both batteries and solar panels. There were four separate battery packs, which have a Lithium-Ion chemistry. They have a voltage of 3.7V and energy capacity of 13,600mAh each. These were purchased from Digi-Key, part number: 3145-L37A136-4-3-2W-ND.

By utilizing an OTS power management board powering the batteries, solar panels, and Arduinos were all managed simply. The power management board was produced by DFRobot, part number: DFR0535. Once the wiring was complete (Figure 5.9), the solar panels were able to charge each battery pack, and the Arduino was able to receive power from the battery pack [8].

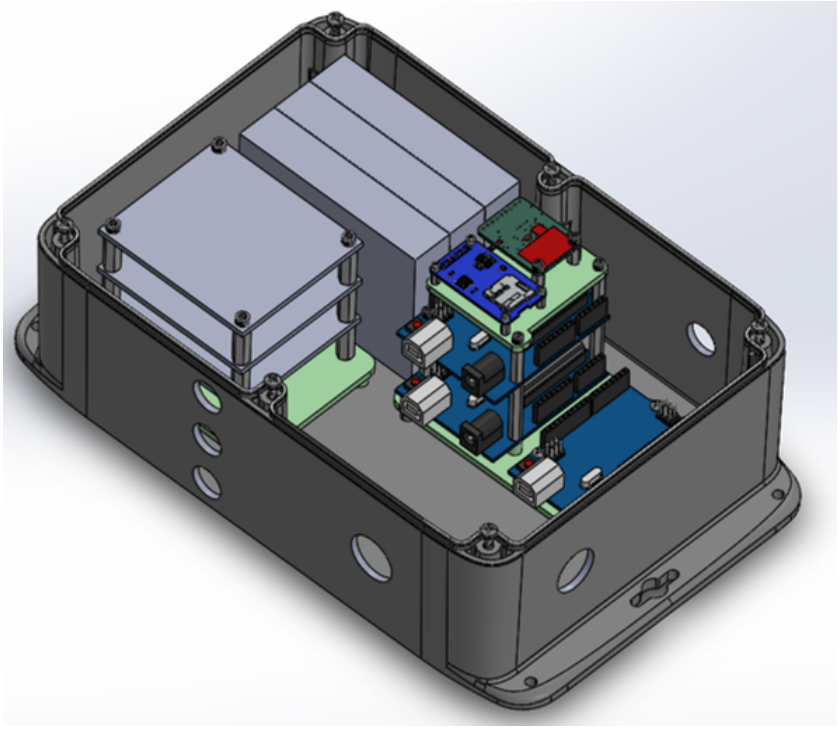

Figure 5.8: DAQ: layout and hardware planning designed using CAD SolidWorks software.

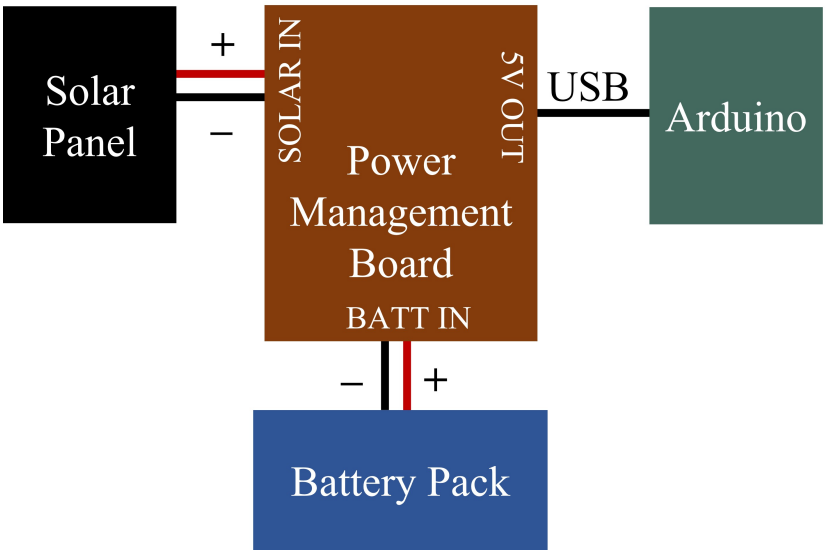

Figure 5.9: DAQ: diagram overview of power wiring circuit for individual Arduino

There were three solar panels which attach to the top of the DAQ module's waterproof box. These panels were all bolted to an aluminum plate which was Velcroed to the box lid

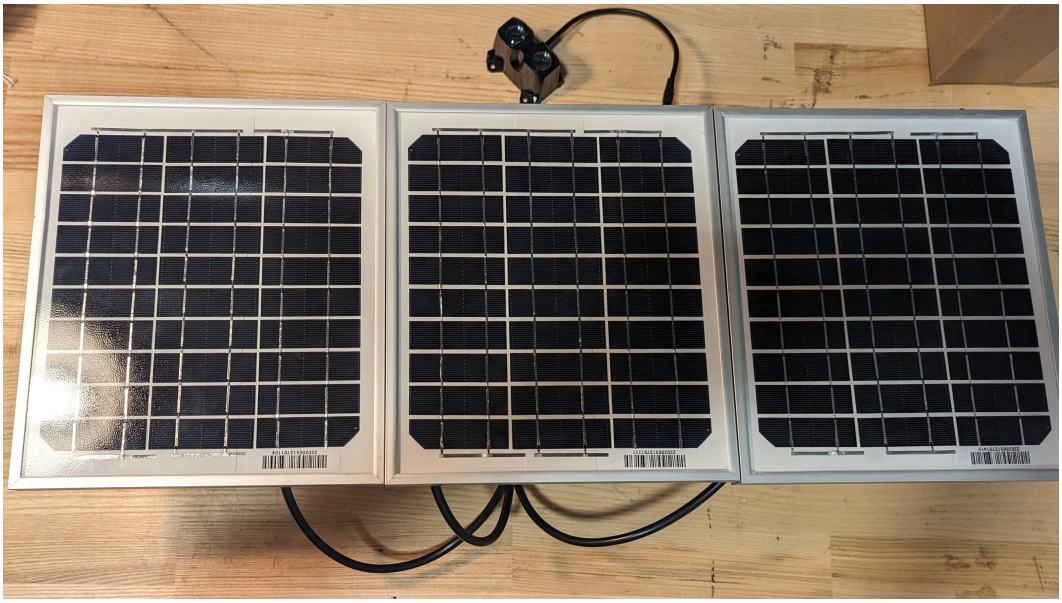

Figure 5.10: DAQ: solar panel assembly

(Figure 5.10). During deployment, the solar panels were easily removed from the box lid to access the bolts to open the box. The solar panels were 12V and 5W. Each panel weighed less than one pound each, was rated IP65 (splash resistant), and was comprised of materials that were durable in outdoor conditions. Using 3M Marine 4200 FC, the solar panel cable connections were kept secure and watertight on each panel.

The battery packs and solar panels each included wire leads to connect directly to each power management board. The Arduinos required an additional USB A to B adapter cable between each power management board and Arduino Uno.

Once the DAQ module was fully assembled and the lidar and flow meter were integrated, a series of power tests were conducted to verify the DAQ module could provide sufficient energy for the field deployment. This verification was done by first measuring the current draw of each Arduino and sensor circuit. Calculations were then used to project the run time given the battery size and solar panel output. Initially, the batteries and solar panels chosen were not sufficient to provide power. The batteries were upgraded to batteries with a higher energy capacity, and the solar panels were exchanged for more powerful ones. The batteries used in the final system were Dantona (p/n: L37A136-4-3-2W) with a 13,600mAh

capacity for each pack. Two packs were used on the lidar circuit, due to its higher current draw rates. The solar panels were 5W, 12V, and a current capacity of 0.35A. The DAQ module and sensors were then tested outdoors in cold, low light conditions in late February and early March of 2023. After approximately ten days of testing, conservative projected run times were calculated as a minimum of seven days. Given steadily increasing daylight and air temperatures predicted in March, the run time was deemed sufficient for the field test. Results from this test were included in Appendix B.

Lidar Integration Using the wiring diagram from the lidar manual [35], and the v3HP PWM example code from the Lidar Lite GitHub repository [56], the lidar was set up using an Arduino Uno and a laptop, connected by a USB adapter cable. A 1kΩ resistor was soldered into place according to the wiring diagram (Figure 5.11) to allow for correct data triggering.

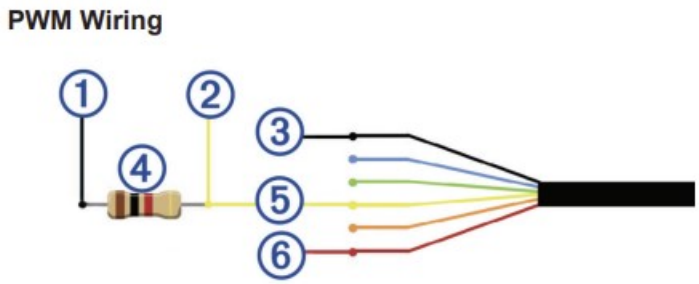

Figure 5.11: DAQ: lidar Cable Wiring Diagram [35]

The lidar cable wiring as purchased needed an extension in order to fit onto the spar top plate. Three additional wires were soldered onto the cable harness to account for this extra length (Figure 5.13).

After the lidar was physically integrated to the DAQ module, example code from the manufacturer was modified and uploaded to the Arduino to properly collect data. This code is included in Appendix C. Arduino codes for the flow meter and data writing operation

Table 5.1: Details for lidar cable wiring diagram [35]

Item	Description	Notes
1	Trigger Pin on MicroController	Connect to trigger pin on microcontroller
2	Monitor Pin on MicroController	Connect one side of resistor to mode control connection device and the other to a monitoring pin on microcontroller
3	Power Ground (-) Connection	Black Wire
4	1kΩ Resistor	
5	Mode Control Connection	Yellow Wire
6	5VDC Power (+) Connection	Red Wire, Sensor takes 4.75 to 5.5 VDC, Max was 6VDC

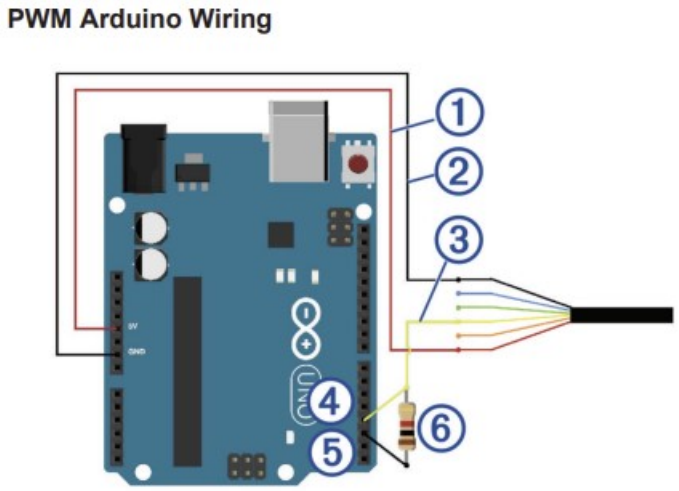

Figure 5.12: DAQ: lidar and Arduino wiring diagram [35]

Table 5.2: Details for lidar and Arduino wiring diagram [35]

Item	Description	Notes
1	5VDC Power (+) Connection	Red Wire, Sensor takes 4.75 to 5.5 VDC, Max was 6VDC
2	Power Ground (-) Connection	Black Wire
3	Mode Control Connection	Yellow Wire
4	Monitor Pin on Microcontroller	Connect one side of resistor to mode control connection device and the other to a monitoring pin on microcontroller
5	Trigger Pin on Microcontroller	Connect to trigger pin on microcontroller
6	1kΩ Resistor	

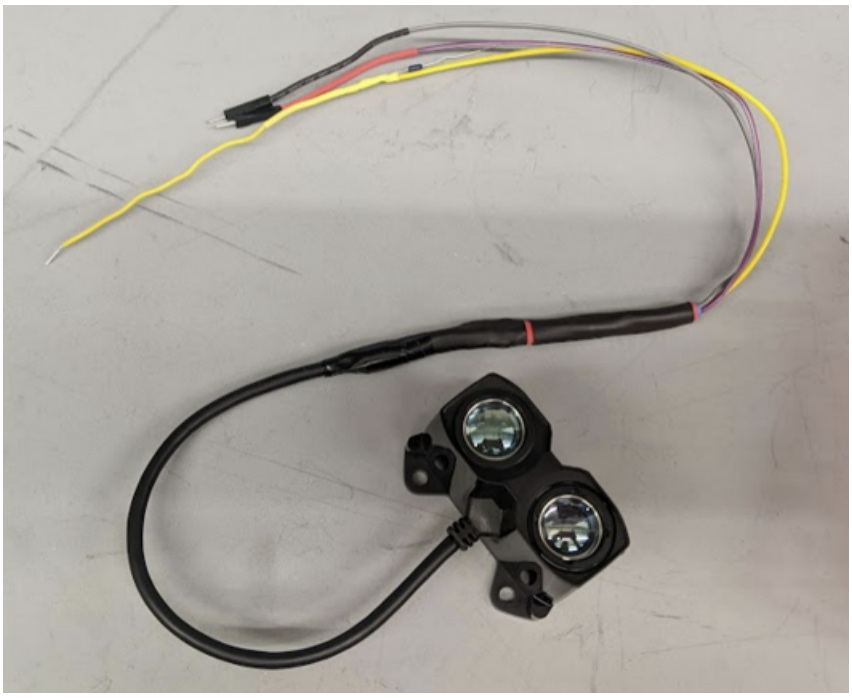

Figure 5.13: DAQ: lidar with cable extension and resistor

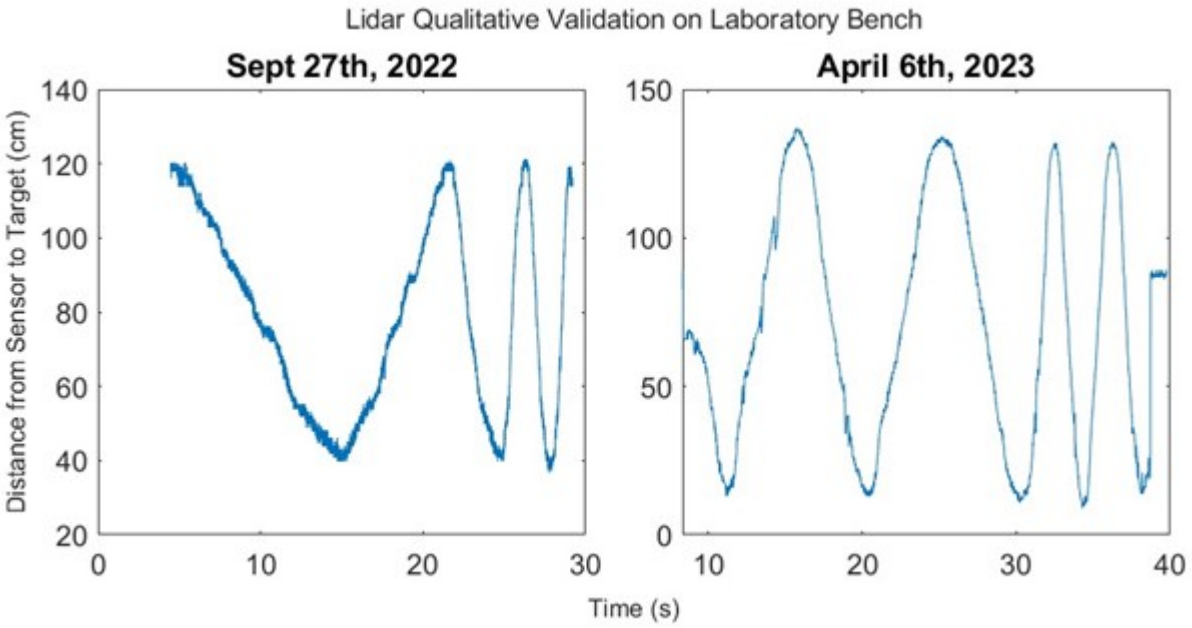

Figure 5.14: DAQ: lidar qualitative functionality result

were also included in Appendix C.

A quality check of the lidar was conducted on a lab bench. The lidar, connected to the DAQ module and using the data recording microSD card feature, was powered on.

The vertical space above the lidar was measured and marked at the approximate locations expected during deployment: 40 and 120 centimeters (approximately 15 to 47 inches). A target above the lidar was moved by hand between these two points, in a manner expected during the field deployment. The lidar collected data at a sampling rate of 59Hz. The results from this qualitative test were included in Figure 5.14. The lidar was tested in the same manner after the deployment, except that the range of test distances increased to include 20cm and 140cm. These lidar quality checks indicate that the lidar quickly responded to a rapidly moving target. The accuracy of the lidar measurement was reported by the manufacturer as ± 5cm at distances less than 2 meters with a resolution of ± 1cm [35]. Variation between trials was expected to be due to human manipulation of the target at approximate distances.

A second, post-deployment calibration was completed using an image tracking software, Kinovea [33], to validate the lidar measurement. The lidar was placed on a level surface with a white wall in the background. The white wall aids the image tracking software in increasing its accuracy. To calibrate the image tracking software, a vertical strip of electrical tape 17cm in length was measured and taped to the wall. In the image tracking software, a line was placed over the strip of tape, and set to 17cm in length. This indicates to the software that the length of the line in pixels was equivalent to 17cm in the real world. The image tracking software was given two targets, one was the lidar (which does not move), and the target (which was moved by hand over the lidar). The lidar was connected to the DAQ module to record the data and was powered by a laptop computer. The target was moved between just above the lidar sensor, up to a minimum distance of 140cm which was measured out on the wall prior to beginning the calibration video. A screenshot from the image tracking software is included in Figure 5.15.

The results from the post-deployment lidar calibration were shown in Figure 5.16. The lidar measurement from the DAQ module was shown in blue and the Kinovea image tracked trajectory of the target was shown in orange. The orange line was slightly narrower for

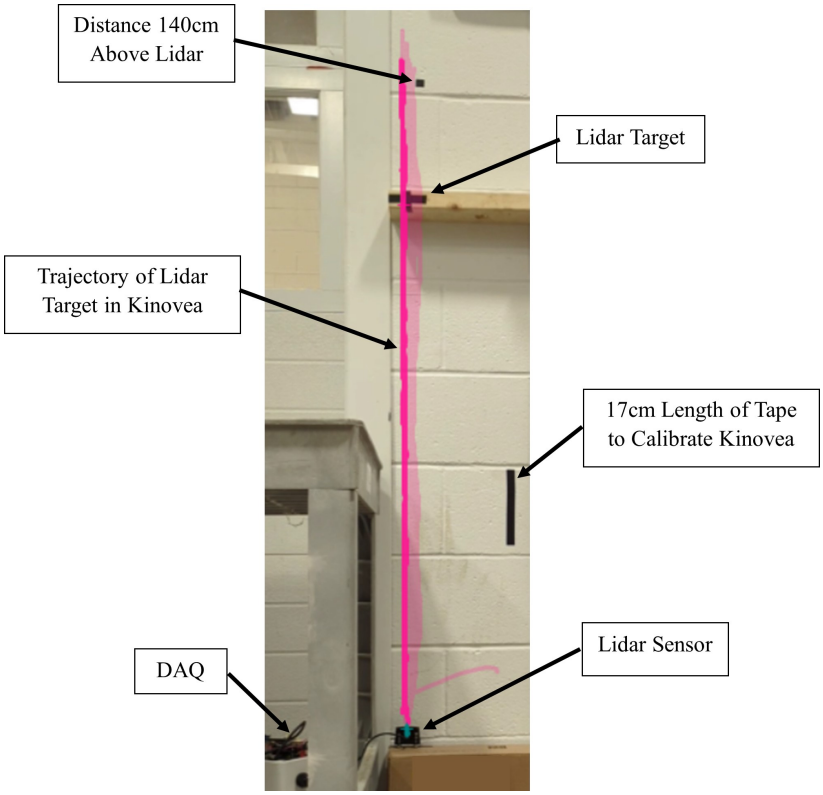

Figure 5.15: DAQ: lidar Kinovea calibration set up on June 15th, 2023

visibility. The image tracked line closely aligned with the lidar measurement, indicating the high degree of accuracy and precision of the sensor. The lidar was expected to have an accuracy of $\pm$ 5 cm, and the image tracking also has a degree of error associated with the drift of the target location throughout the video. The correlation between these two signals was found using the Matlab 'corrcoef' function and was found to have an R value of 0.976 and a P value of 0, indicating a near perfect positive correlation that is statistically significant. This test indicates that the lidar sensor measurement was reliable during bench testing after the deployment.

Flow Meter Integration and Calibration Details During flow meter integration to the DAQ module, a flow meter outside of its housing was used to bench test the code. The flow meter wiring and code was derived from a BC Robotics product tutorial available online [7]. Due to the nature of the flow meter, a sampling rate of 1Hz was the fastest available

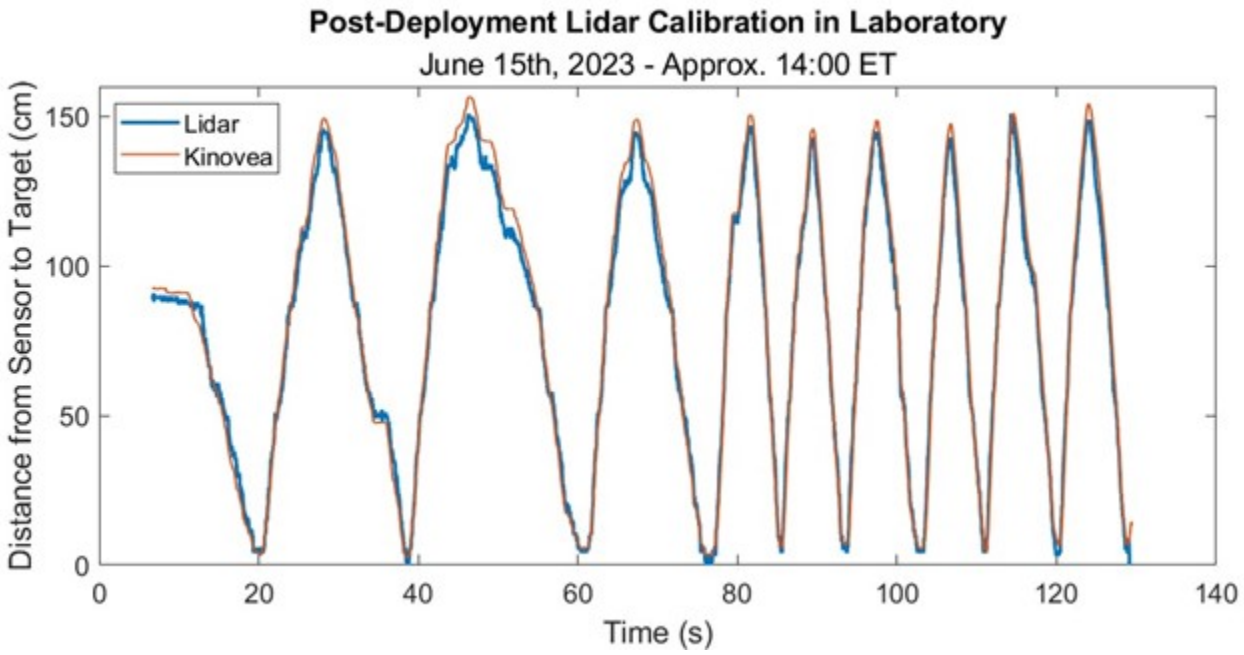

Figure 5.16: DAQ: lidar Kinovea calibration result post-deployment

with an acceptable data resolution. During the calibration test, the sensor specific volume coefficient given in the code was changed to reflect the actual volume flow rate for the sensor. This value was changed from 2.25mL to 83 and 1/3mL, because the sensor produces twelve pulses per liter [21].

To calibrate the sensor and validate the flow rate readings, the set up was tested in the laboratory.

The flow meter calibration was also validated for its accuracy prior to and after the field deployment. The flow meter calibration set up is shown in Figure 5.17. The flow meter in its housing was electrically connected to the DAQ module using a pigtail cable. A submersible pump, control valve, and two-inch diameter, eight-foot-long hose were connected to the flow meter housing. The submersible pump was placed in the engineering tank to draw water for the test. The outlet of the flow meter was angled such that the flow would return to the tank. The DAQ module was connected to a computer to display the instantaneous flow rate using the Arduino IDE Serial Monitor. The valve was adjusted for each test, beginning

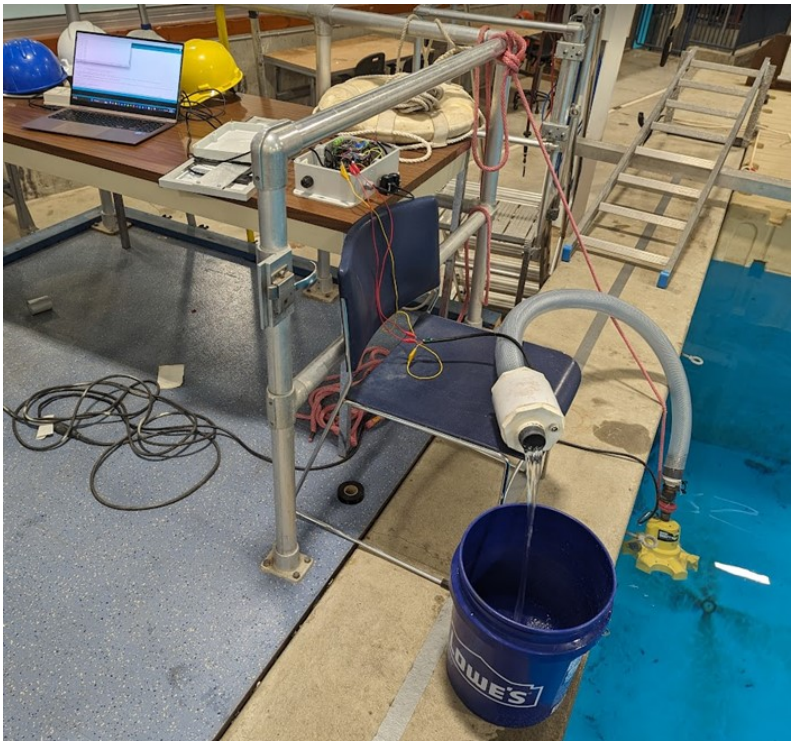

Figure 5.17: DAQ: flow meter calibration set up on June 25th, 2023

with the valve open enough to allow flow, then a quarter turn opening adjustment for each new test. As each test was run, the instantaneous flow rate was read from the computer once reaching steady state. The flow rate was then measured independently with a bucket and timer. After reaching steady state flow with the same valve position, the bucket was moved under the flow stream. After 15 seconds, the pumped volume was measured, and a flow rate was recorded. The pre- and post-deployment flow meter calibration was combined in Figure 5.18, to indicate the quality of the sensor throughout the field deployment. The two flow rates, from the DAQ module and from the timing method were compared before and after the field test.

The resolution or uncertainty in the flow meter reading was approximately $\pm$ 5 liters per minute, which were reflected in the error bars on Figure 5.18. Additionally, an instantaneous flow rate from the DAQ module was read once the flow achieved steady state. If the numbers appeared to be between two values, both were used and averaged together. However, this was

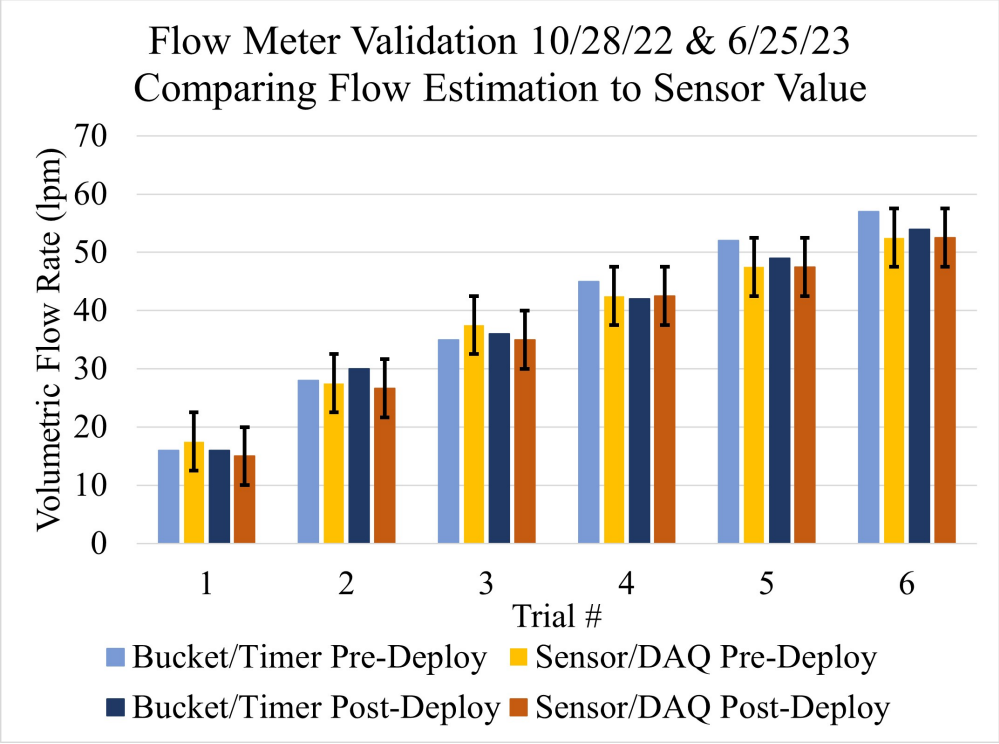

Figure 5.18: DAQ: flow meter validation result from both pre- and post-deployment

not always done and increases the uncertainty in the sensor and DAQ module measurement. There was also some error expected from the timing method due to human reaction time, and volume estimation which was measured in two-liter increments on the bucket. The same methods were used after the deployment to ensure the calibration remained in good condition throughout the field test. The timing method and DAQ module reading were in good agreement for this pre-deployment validation exercise, where the timing method falls within each uncertainty region for all six trials. The same was true for the post-deployment validation, with identical results from the sensor and DAQ module for the last three trials. The bucket and timing method results more closely agree with the sensor and DAQ module result for the post-deployment test, likely due to having practiced the method more extensively prior to the test. From this validation, it appears that the flow meter sensor behaves similarly after the field deployment as it did prior, and the sensor appears to have an accurate data result, with a $\pm$ 5 liter per minute resolution.

GPS Integration The GPS module integrated into the DAQ module was Adafruit Ultimate GPS Breakout board. The wiring diagram used was derived from the Adafruit manual [2]. The code used [24], produces the GPS date, hour, minute, and second into the data collection stream.

The pins were soldered onto the GPS board and wiring connections made according to the wiring diagram (Figure 5.19).

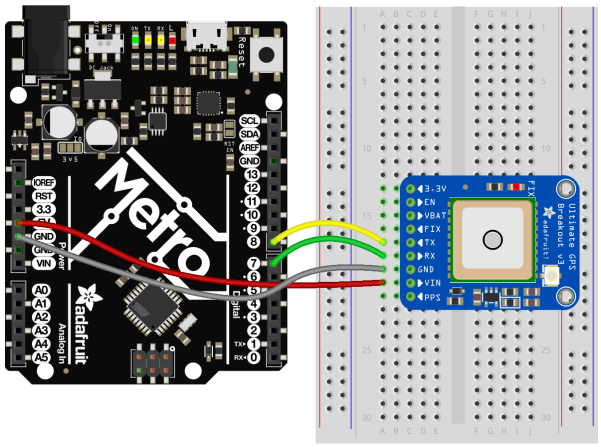

Figure 5.19: DAQ: GPS wiring diagram to microcontroller [2]

MicroSD Storage Integration The Arduino Uno which received the lidar, flow meter, and GPS data also wrote the data to a microSD card. This was done by utilizing a MicroSD Card Breakout Board. The wiring between the Arduino and MicroSD breakout board was completed according to the wiring diagram [1], and the code used created a new file every twenty minutes containing time, flow rate, and relative distance measurements. The internal Arduino clock time was also recorded on each data file.

Arduino Unos To minimize energy requirements, the data for the lidar, flow meter, and GPS were all written onto the same microSD card. Additionally, storing the data this way synchronized the data onto the same clock system. This task of transferring data between Arduinos was accomplished by using both analog and digital communications. The analog

or serial communication code was created [29]. The wiring for the analog communication between the two Arduinos requires three wires: a common ground, pin 0 of flow meter Arduino to pin 1 of data storage Arduino, pin 1 of flow meter Arduino to pin 0 of data storage Arduino. The digital or I2C communication code was created [52]. The wiring for the I2C communication also requires three wires: a common ground, pin A4 to A4, pin A5 to A5. The Arduino Uno internal clock has an operating frequency of 400kHz. It has an accuracy of +/-0.06 seconds in a twenty minute interval. Each twenty-minute interval as a new data file was recorded, the Arduino internal clock was reset using GPS time. The code for timing and creating data files was created by referencing earlier projects using wave pump project [20]. The Arduino code for the GPS and data storage operations were in Appendix C.

3D Printed Brackets and Wire Management 3D printed brackets were designed and created so that the Arduino, GPS, MicroSD, and power management boards could all be secured within the DAQ module's enclosure safely. By screwing these boards down, there was less of a chance that the boards could become damaged during an ocean deployment or have their electrical connections come loose. This was accomplished using a variety of hardware including metal standoffs, to space the board stacks to reduce overheating and accommodate the limited space available in the DAQ module's enclosure. Wire connections to the Arduino boards were all M-F pins secured with acrylic adhesive. Wires were managed with cable ties and holders to prevent undue tension and stress.

Overall DAQ Module Diagram A simplified, overall wiring diagram summarizes the interconnects amongst all the components within the DAQ module (Figure 5.21). This diagram indicates how items were powered, and how data was transferred through the system. It does not show the individual wiring connections, but represents a broad overview. Red arrows indicate one part providing power to another, and green arrows indicate a data

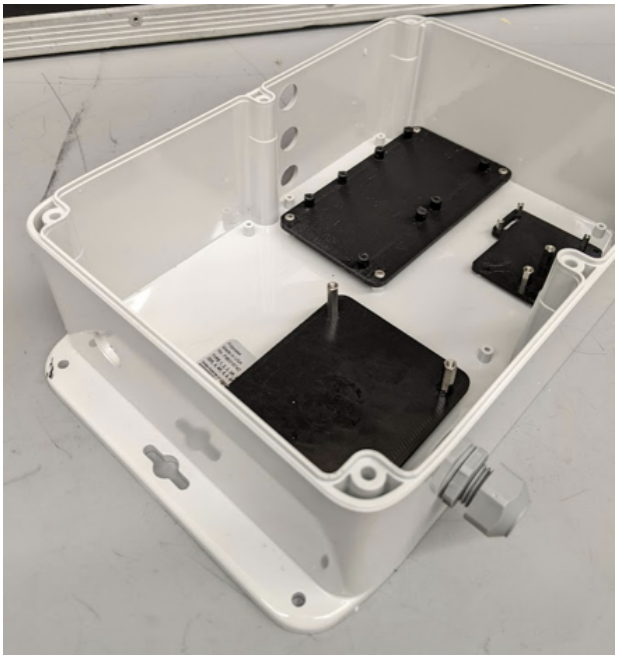

Figure 5.20: DAQ: OTS housing with 3D printed brackets and ports drilled for cable routing

transfer from one item to another.

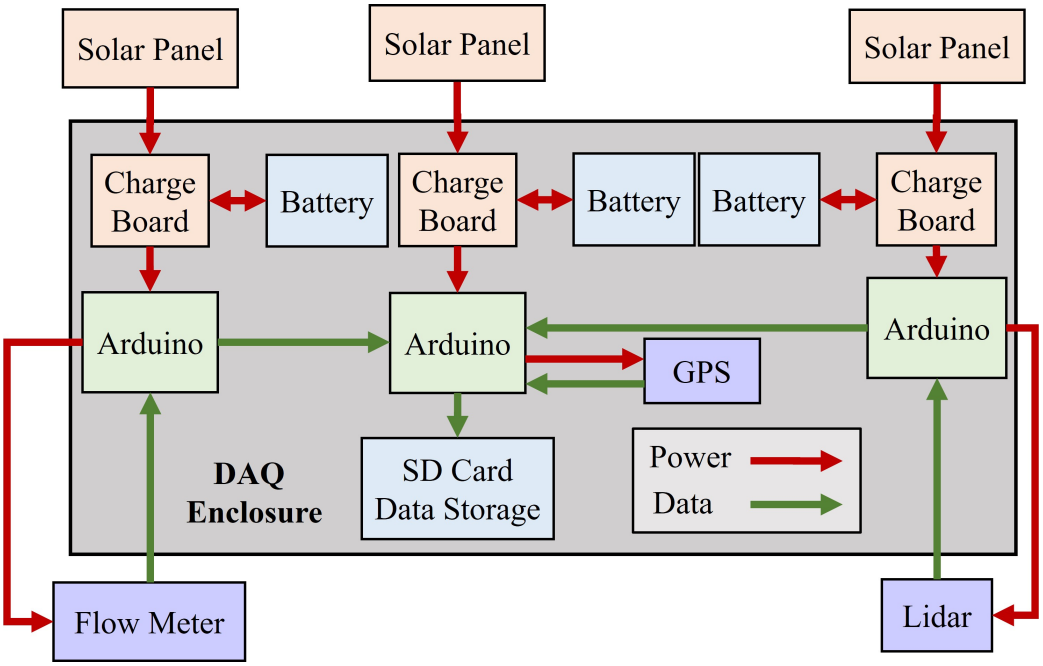

Figure 5.21: DAQ: simplified overall wiring diagram

The top plate of the spar buoy is shown in (Figure 5.22) with the DAQ module installed.

The DAQ module was shown with the cover off. The lidar was installed on the top plate, with its DAQ module wiring complete. The flow meter cable was connected to the DAQ module. The solar panels were on the cover underneath the DAQ module, with the stainless steel cable coverings shown. During deployment, the lid was reattached with six screws to create the waterproof enclosure. In the midst of deployment, the cover was removed and the microSD card with data was retrieved, without needing to move the wave pump device from its mooring.

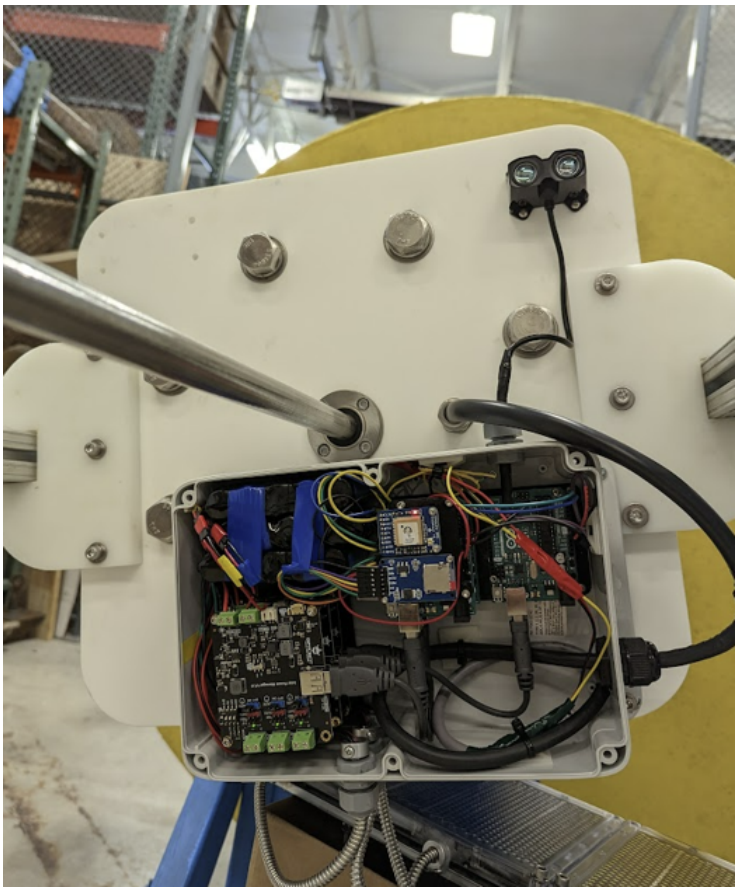

Figure 5.22: DAQ: fully assembled onto wave pump with cover off

CHAPTER 6

Ocean Field Deployment

6.1 Overview

This section includes details on the final laboratory test, mooring designs, and ocean field deployment process. To prepare for and conduct the ocean field deployment, a final laboratory test was completed. This final tank test comprised the wave pump device fully assembled with the flow meter, lidar, and DAQ module operational. The device and instrumentation was analyzed for functionality before undertaking the field deployment. In preparation for the field deployment, review of the mooring plan and hardware for both the wave pump device and Sofar spotter buoy moorings was completed. Moorings and logistics were discussed with all members of the team, including the boat captain. The detailed process for completing the field deployment was also included in this section.

6.2 Tank Test Fully Assembled Device

Prior to conducting the ocean field deployment, the fully assembled device was tested in the engineering tank. The first test on November 4th, 2022. This test revealed a leak in the spar buoy as detailed in 4.8. After repairs were complete, and the instrumentation was fully integrated and calibrated a test in the engineering tank to verify overall reliability and operation was required.

The wave pump device was outfitted with the instruments for the field deployment: flow meter, lidar, and DAQ module. This instrumented wave pump was tested in the engineering tank on February 21st, 2023. Small surface waves were generated in the tank by rocking a

floating dock up and down. A photograph of the test set up is included in Figure 6.1.

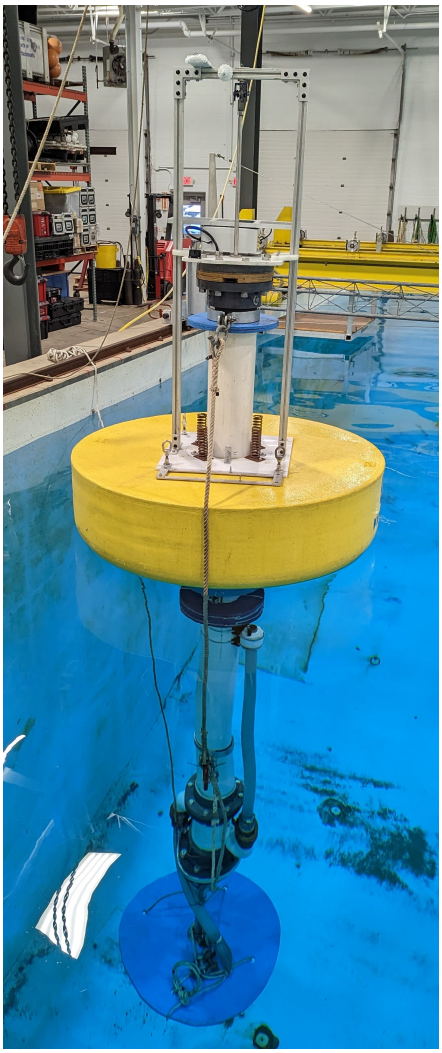

Figure 6.1: Pre-deployment tank test fully assembled wave pump device with instrumentation.

The data collected from this test were evaluated and indicated that the sensors and DAQ module were working as expected. The lidar and flow meter data collected by the DAQ module during the engineering tank test is shown in Figure 6.2. The lidar data was shown in the top plot as a relative distance. The relative distance plot mainly oscillates around 75cm distance, which indicates the distance between the lidar sensor and its target when the device was at equilibrium. The total amount of pumped water during this twenty-minute period was 43.1 gallons. The average flow rate was 2.2 gallons per minute. The average

stroke height was determined by using a peak detection formula and subtracting the valleys from each peak. Then those values were averaged. The average stroke height was 9.5cm, and the significant average stroke height (average highest 1/3) was 13.7cm. The average stroke period was calculated by subtracting each successive peak time from the previous and averaging those values together. The average stroke period was 1.34 seconds. From observations during the tank test, the average stroke height and period values appear to be accurate. The average relative velocity was $6.3\frac{cm}{second}$.

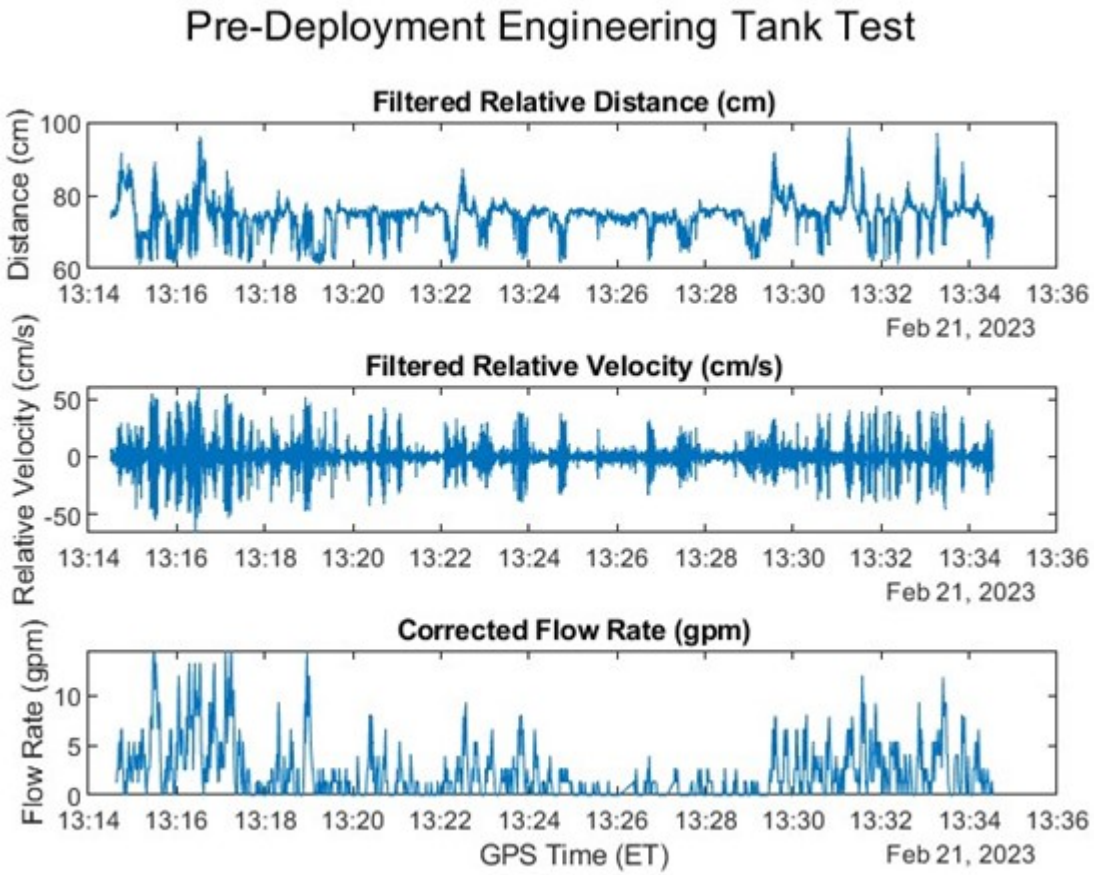

Figure 6.2: Pre-deployment tank test fully assembled wave pump device with instrumentation result summary.

6.3 Mooring Diagrams

6.3.1 Wave Pump Device Mooring

The mooring system for the wave pump was developed prior to the field deployment. The design for the wave pump mooring was intended to have minimal effect upon the heave motion of the float buoy. This mooring comprises new $\frac{3}{4}$-inch thick, nylon lines which had galvanized thimbles spliced into each end. The tensile strength of the lines was 12,800 pounds. Two six-foot and one eight-foot-long lines were connected in a y-shape bridle as shown in Figure 6.3. Chafe gear was attached to the shorter line sections, to prevent abrasion where they contact the yellow float buoy. The mooring design includes cotter pins or mousing wire to close all shackles. The mooring bridle connects to an 18-inch mooring buoy, with a swivel to the mooring chain. An additional 12-inch subsurface float was used to connect to the chain, as well as an A4 sized fender buoy at the top of the mooring buoy. Typically, a 32-inch mooring buoy was used to float the chain; however, the collection listed of mooring floats was sufficient to float the mooring chain. The subsurface connection for the mooring line likely increased its survivability at sea.

A lifting bridle made of the same line, with galvanized thimbles on either end, attached at both the upper and lower ends of the spar. It was comprised of one six-foot and one eight-foot length so that the center rests over the device's center of gravity. A lifting link in the center allows for safe lifting operations of the wave pump device. Chafe gear was also placed along the lifting bridle at the abrading location along the yellow surface float.

The 18-inch mooring buoy and mooring line bridle is shown in Figure 6.4, left. The attachment point between the mooring lines and surface float is shown in detail in Figure 6.4, right.

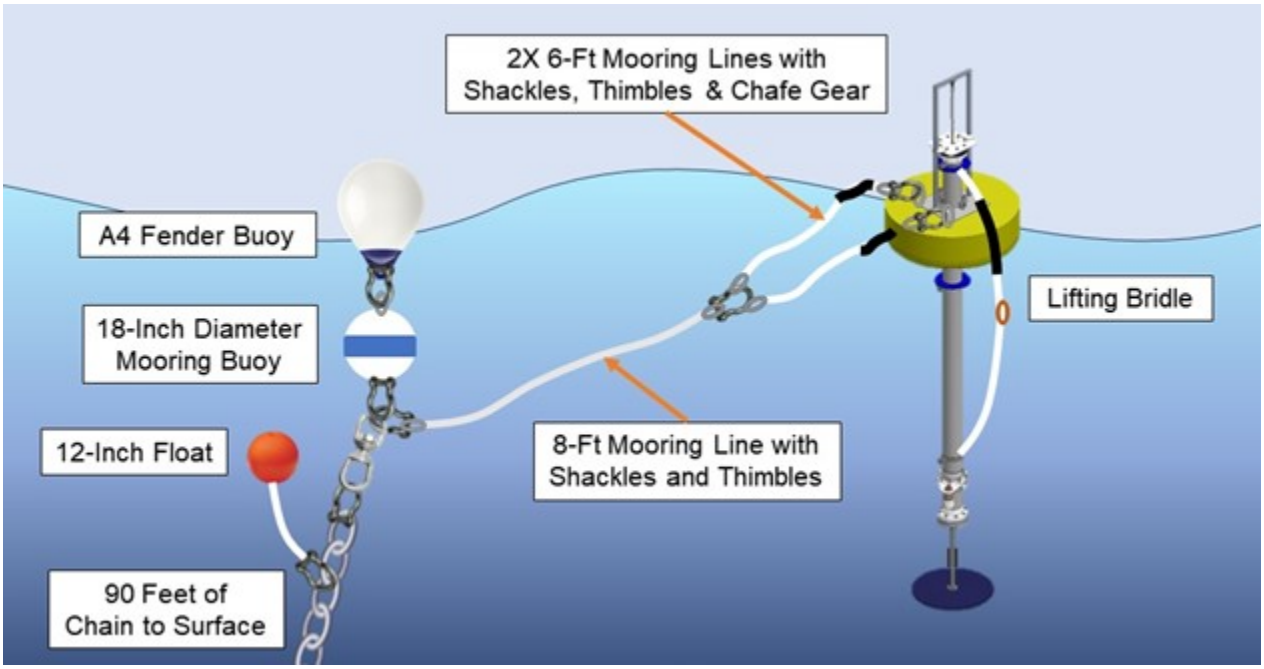

Figure 6.3: Mooring diagram for wave pump device for ocean field deployment.

Figure 6.4: Wave pump mooring components prior to deployment. Y-shape bridle and long mooring line connect to swivel, shackles, and buoy (left). Y-shape bridle connections to float eyehooks with shackles (right).

6.3.2 Sofar Spotter Buoy and Hydrophone Mooring

The mooring diagram for the Sofar Spotter buoy is shown in Figure 6.5. The Sofar Spotter buoy was an instrument which measures wave and wind conditions, air temperature, and

location. It was located on a separate mooring to capture data of the wave field independently of the wave pump device. For this mooring set up, the SML winter mooring post was left in for the duration of the deployment. The Spotter mooring comprised a nearly fifty-foot-long piece of polypropylene line with floats and weights interspersed throughout its length. The floats and weights create an "accordion" effect when the buoy was in the water, which allows the Spotter to freely travel in the waves without significant drag forces exerted upon the Spotter by the mooring line. This increases the Spotter's ability to collect accurate data. On either end of the mooring line was a five-foot-long rubber coated chain, which helps act as a ballast weight under the Spotter, as well as prevent abrasion. Swivels and shackles allow for freedom of rotation, and prevention of entanglement of the mooring to itself. All shackles were seized with mousing wire to prevent them from becoming undone during the deployment. Two hydrophones were installed along the mooring line rope using two hose clamps and three heavy duty zip ties each.

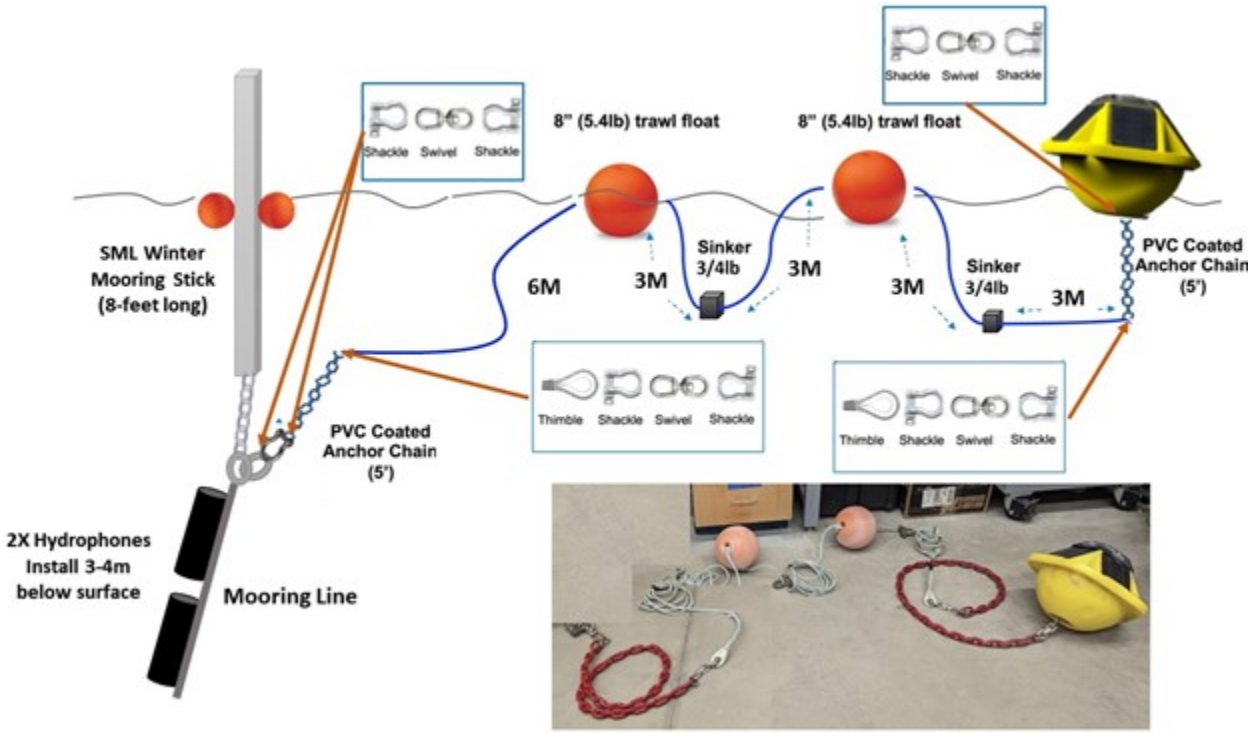

Figure 6.5: Sofar Spotter field deployment mooring diagram and detail photograph of actual components.

6.4 Wave Pump Device Ocean Deployment

Loading, transport, and deployment activities were performed by trained personnel and crew of the R/V Gulf Challenger, all of which have extensive experience deploying the wave pump and similar devices into the ocean environment. The team has detailed knowledge of the environment and typical conditions at the Isles of Shoals, including the proposed deployment site. Included here were the steps that taken to complete the ocean field deployment process.

6.4.1 Logistics and Pre-Deployment Planning

The R/V Gulf Challenger was reserved in advance for deployment and retrieval. Confirming dates and weather capabilities with the captain prior to deployment was critical for a successful deployment. The UNH CCOM truck and a dual axle flatbed trailer was also reserved in advance for transporting the wave pump to and from the laboratory in Durham to the pier in New Castle, NH. The deployment dates were confirmed with the Shoals Marine Laboratory staff for availability of their moorings. All supplies and tools were organized prior to the deployment day in the laboratory, to ensure all equipment required was transported to the pier.

6.4.2 Transit to Pier

The sensors, DAQ module, marine light, hoses, heave plate, and ballast were removed from the wave pump prior to transport. These items were driven separately to the pier in a car to reduce potential damage to the device or electronics.

A flat-bed trailer and truck were used to transport the wave pump Figure 6.6 from the Chase Ocean Engineering building in Durham, NH to the UNH pier in New Castle, NH on March 20th, 2023. The wheel sections were removed from blue device stands, which were then placed onto the trailer. The float was secured to the bottom stopper plate using a piece of line. The wave pump device was loaded onto the trailer using the lifting bridle and a

forklift at the laboratory. Three heavy-duty tensioned straps and ropes were used to keep the device in place on the trailer.

Figure 6.6: Wave pump loaded onto flatbed trailer with stands and straps.

The remaining equipment was loaded into the truck including: mooring lines, shackles, output hoses, Sofar spotter buoy, heave plate, weights, zip-ties, and extra supplies and tools. At the pier, a crane was used to lift the wave pump off the trailer, and onto the deck of the pier Figure 6.7.

Figure 6.7: Unloading the wave pump device from the trailer using the crane pier.

6.4.3 Preparation on the Pier

Once the device was secured at the pier, the heave plate, ballast, and lower intake hose with filter were installed (Figure 6.8, left). The shackles shown on the heave plate add up

to thirteen pounds of additional ballast required. The lower intake hose was approximately two feet long and was secured to the heave plate pipe with a hose clamp. The outlet hose was installed along with the flow meter sensor in its waterproof housing (Figure 6.8, right). The hoses and flow meter were secured using hose clamps of various sizes. The flow meter sensor data cable was installed and secured using cable ties. The marine Carmanah light was installed onto the surface float bracket (Figure 6.9). The light was programmed to flash a white light for $\frac{1}{2}$ of a second every 1.5 seconds. This specification meets the NEPA permitting requirement.

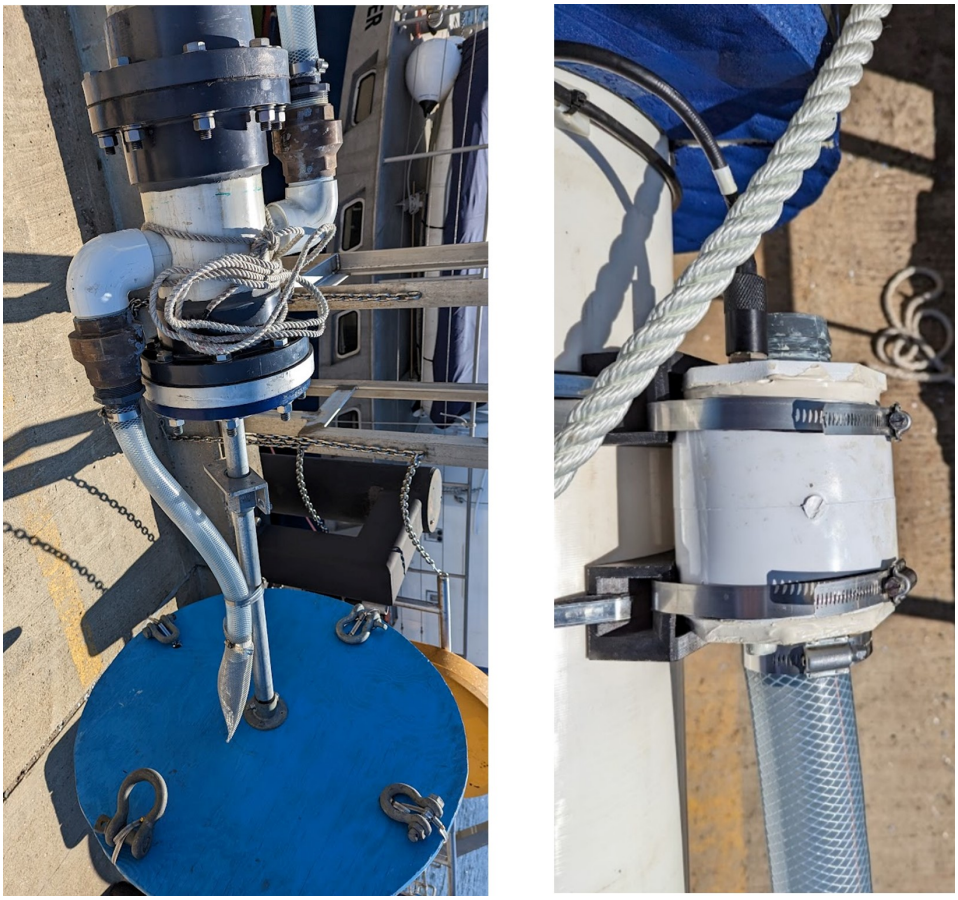

Figure 6.8: Heave plate, ballast, lower intake hose installed to spar on pier (left) and upper intake hose, flow meter housing, and cable installed to spar on pier (right).

The DAQ module was installed onto the plate atop the spar buoy (Figure 6.10). The flow

Figure 6.9: Marine Carmanah light installed onto surface float bracket for visibility at night and to meet NEPA permitting requirements.

meter data cable was routed through the cable gland and necessary electrical connections were made. The lidar was installed onto the spar plate. The DAQ module was briefly powered on, and the lidar and flow meters were briefly tested for quality of their electrical connection. The lidar was tested by moving an object over the sensor, and the flow meter was tested by blowing through the housing prior to installing the hose. Data appeared for both sensors which indicated they were in good working order. The batteries were removed until the morning of the device deployment. The data card was cleared and re-inserted to the DAQ module.

The motion-triggered video cameras and their solar panels which provide power were installed atop the float buoy gantry (Figure 6.11). These were installed with a combination of hardware and cable ties.

At 9:00AM ET March 21st, 2023, the device and gear were loaded onto the R/V Gulf Challenger (Figure 6.12 and Figure 6.13). The pier's crane, and device's vertical riser stands were used to safely stow the device onto the deck of the ship. The device was kept in place

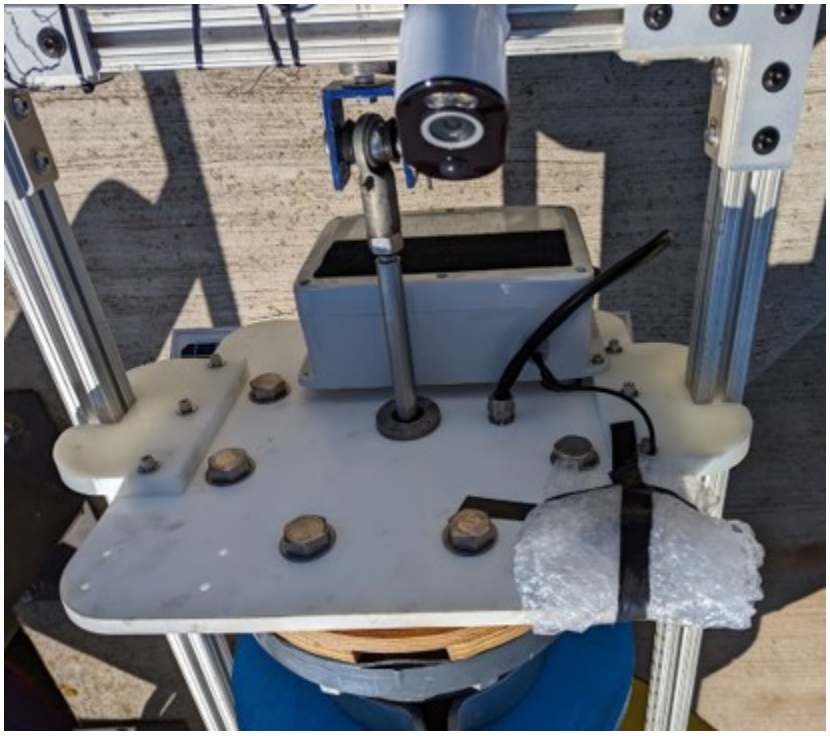

Figure 6.10: DAQ module and lidar installed onto spar top plate.

using tensioned straps and rope. The device was placed onboard such that the top of the spar was facing towards the bow of the ship and the heave plate hung over the stern. The aft gates of the vessel were removed to accommodate the length of the wave pump device. The remaining gear was loaded onto the vessel.

6.4.4 Transit to Mooring Site

The ship departed from the pier at 9:25AM enroute for Appledore Island, ME. The weather conditions were sunny, light breeze, and calm seas. During the transit to the mooring site, the batteries were installed into the DAQ module, instruments were powered on, and data began recording. The Sofar Spotter buoy was also turned on using the magnet method, LED status lights indicated a good GPS fix and that it was in good working order. Arriving on site (GPS coordinates: 42° 59' 16.1" N, 70° 37' 8.5" W) at 9:50AM, the #5 mooring was picked up by the boat crew and tied off to the port-rear cleat (Figure 6.14). The mooring

Figure 6.11: Motion triggered video cameras, solar panels, and lidar target installed onto float gantry.

bridle was installed onto the wave pump, and the shackles on the float eye hooks were seized with mousing wire.

6.4.5 On-Site Mooring Installation

At 10:10AM, the wave pump lifting line was secured to the boat's hydraulic winch, running through the A-frame. A quick release was installed between the lift line and the winch line. The device was lifted out over the water using the A-frame and lowered into the water (Figure 6.15). The quick release was used to detach the lift line from the winch line. The device was oriented upright during the deployment by pushing on the float's upper gantry. The mooring bridle from the device was tied off mid-ship on the starboard side while the mooring was prepared (Figure 6.16).

The winterized mooring post was pulled on board using the winch and A-frame (Figure 6.17, left). Safety lines were iteratively used throughout the process to decrease the likelihood of losing the mooring overboard. The mooring rope was pulled aboard, and the

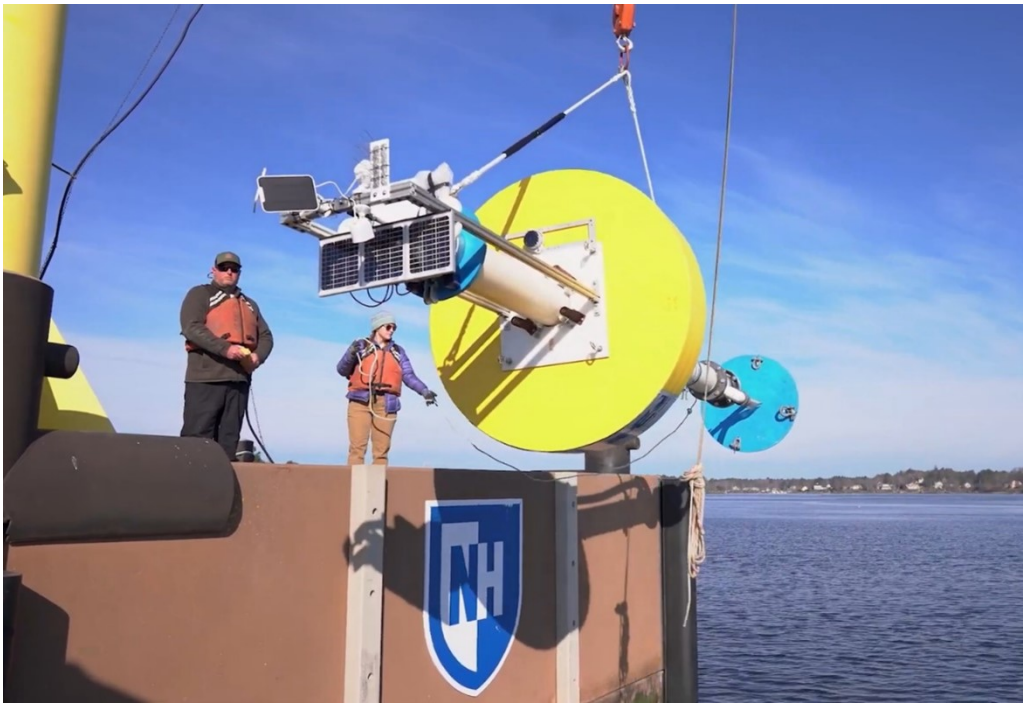

Figure 6.12: Loading operation of wave pump device from pier onto R/V Gulf Challenger, from deck of ship facing towards pier.

mooring chain was held by both the winch and safety line while the mooring post and rope were removed. A 26-pound buoyant trawl float, a 113-pound buoyant mooring ball, and one of the Gulf Challenger's A4 sized fenders were used in conjunction to float the mooring chain and attach the wave pump's mooring bridle (Figure 6.17, right). The mooring operation for the wave pump was completed at 11:20AM.

At the #6 mooring, approximately 300 feet southwest from the #5 mooring (GPS coordinates: 42° 59' 14.8" N, 70° 37' 10.4" W), the mooring post was picked up using the winch. At this location, the mooring post and rope were left in place. The rope was hauled up so that there was sufficient space to install the two ST500 hydrophones using hose clamps and cable ties (Figure 6.18, left). The hydrophones were oriented facing downwards, with a six-inch gap between them. These hydrophones were submerged approximately 3-4 meters depth. The Sofar Spotter buoy and its mooring were attached to the mooring with cotter-pinned shackles. The Spotter mooring was flaked out on the deck of the ship, and the mooring stick

Figure 6.13: Loading wave pump device onto R/V Gulf Challenger using pier crane, facing towards ship. Vertical riser stands (two used, one shown) on ship deck to support device.

was lowered back in the water, utilizing the quick release. The Spotter mooring was then paid out by hand until the Spotter was gently tossed overboard (Figure 6.18, right). This mooring operation was completed at 12:10PM.

Throughout the deployment, the Sofar Spotter Dashboard account was monitored to ensure data was being uploaded.

Prior to leaving the mooring field, the DAQ module data was retrieved, and a new microSD card was inserted. At 12:30PM the ship left the SML mooring field to return to the pier. The ship arrived at the pier at 12:55PM.

6.5 Device Monitoring During Field Test

The device remained on the mooring from March 21st to March 30th, 2023. Monitoring of the device on the mooring was conducted by observing it through the SML Radar Tower webcam. On March 23rd, 2023, at 9:00AM, the UNH Galen J small vessel was taken to the mooring field to recover data and swap batteries from the DAQ module. The vessel was tied alongside the device's float buoy, utilizing the eye hooks and boat's mooring lines

Figure 6.14: R/V Gulf Challenger with device on-board, attached to #5 Mooring in SML mooring field, prior to deployment procedures.

(Figure 6.19). Data were collected, and batteries were swapped. The batteries' voltages (an indication of remaining battery energy capacity) were included in Appendix D.

Observing from the webcam, on March 26th at 12:44PM wave conditions of 3-5 feet from the northwest, and winds of 30 knots were present in the mooring field. These conditions caused the wave pump device to turn onto its side. In this orientation, the device was in a stable equilibrium position Figure 6.20. Once conditions had returned to a safe state for small vessels, on March 28th at 11:00AM the Galen J vessel was used to right the wave pump device. Data were retrieved and the batteries were again swapped from the DAQ module. The video cameras mounted to the float were checked for functionality and found to be in working order. One of the video cameras' microSD cards were swapped to collect some of the video data.

One of the mooring lines from the bridle was moved from the top of the float to the

Figure 6.15: Deploying wave pump device off stern of R/V Gulf Challenger using hydraulic winch, A-frame, and quick release.

bottom of the float, to prevent the device from rotating onto its side again.

The device was returned to normal operation and was monitored after this visit. During a significant storm, from the west, with wave heights 4-6 feet on March 30th at 2:40AM, the device detached from the mooring. The device floated ashore on Appledore Island, where it was retrieved using the Galen J vessel (Figure 6.21, left). Both mooring bridle lines were still attached to the float, and the main mooring line from the mooring to the bridle was still attached to the mooring. The shackle connecting these three lines was missing entirely from the assembly. Given these circumstances, the most likely cause of failure was a lack of cotter pin used to secure the shackle during the deployment process. Reviewing pictures from the deployment procedure also indicate that a cotter pin was not used at this shackle (Figure 6.21, right).

When the wave pump device detached from the mooring few items were lost or damaged. The heave plate and mounting shaft were lost, and the inlet pipe to the wave pump was damaged. Other minor items were lost or damaged during this event.

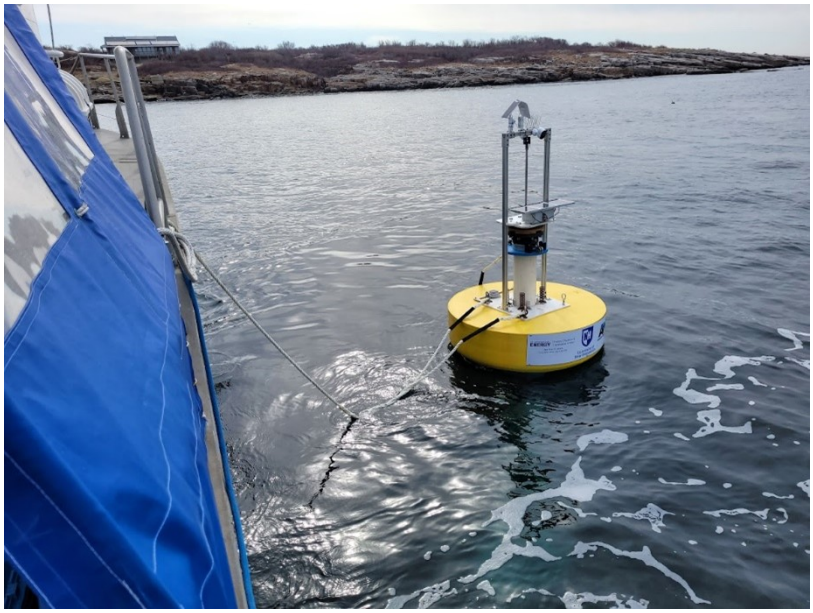

Figure 6.16: Deployed wave pump tied off to starboard side of vessel during mooring chain operations.

6.6 Device and Instrumentation Retrieval From Field Test

On March 31st at 8:00AM, the Galen J vessel was used to retrieve the wave pump device. This retrieval was coordinated with the highest tide of the day. Tying the vessel to the SML high tide dock, team members went ashore, and pushed the wave pump off the rocks. A line was tied around the base of the spar and secured to the Galen J vessel for a tow operation back to the New Castle pier (Figure 6.22). The boat speed averaged three knots for the duration of the towing procedure. Once back at the pier, the crane was used to lift the device out of the water (Figure 6.23), and a forklift was used to stow the device in the parking lot until the flat-bed trailer and truck could be used to bring equipment back to Durham, NH.

April 3rd, 2023, at 8:30AM the Gulf Challenger returned to the mooring field. This operation included collecting the Spotter buoy and hydrophones from the #6 mooring. Additionally, the #5 mooring buoys and remaining lines were collected, and replaced with the

Figure 6.17: Wave pump mooring (#5), removal of winter mooring stick and rope (left), wave pump device fully deployed on mooring, facing towards NH coast (right).

seasonal 32-inch mooring buoy used by SML. All the remaining equipment was recovered and stored back at the Jere A. Chase Ocean Engineering building in Durham, NH.

Figure 6.18: #6 mooring with hydrophones installed onto rope (left), Sofar Spotter buoy and mooring fully installed (right).

Figure 6.19: Galen J vessel tied alongside wave pump at mooring to collect data, March 23rd, 2023.

Figure 6.20: Wave pump device on mooring, stable on its side after rough wave conditions.

Figure 6.21: Wave pump device ashore on Appledore Island, ME, March 31st, 2023 (left). Shackle with missing cotter pin during deployment process March 21st, 2023 (right).

Figure 6.22: Towing wave pump device to New Castle, NH using Galen J vessel.

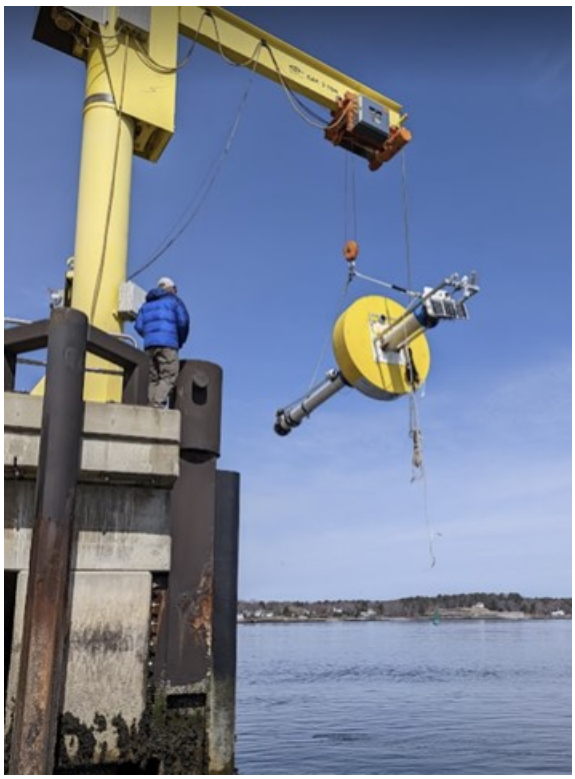

Figure 6.23: Wave pump retrieval using the pier crane.

CHAPTER 7

Data Processing and Results

7.1 Overview

The results from the ocean field deployment analyzing the wave pump performance were included in this chapter. A review of hardware durability was covered for both the device and the DAQ module. Data processing methods are included for GPS time data, flow meter, lidar, and spotter buoy. The results, correlations, and statistical analyses for these items are examined. A brief review of the hydrophone data and video data are included. Overall device performance characteristics are derived utilizing statistics and relative motion RAO's. Field data and accompanying Matlab processing files can be found online at the Marine and Hydrokinetic Data Repository (https://mhkdr.openei.org/submissions/499).

7.2 Hardware Review for Survivability

The wave pump device survived well during the field deployment. If the device had not come free of its mooring, its unlikely that any damage to its hardware would have occurred. There was only one instance of corrosion, however it did not lead to any critical failure. The ballast ring at the bottom of the spar corroded somewhat over the course of the deployment period (nine days). The material was anodized steel, and additionally coated with marine grade anti-fouling paint. However a corrosion resistant steel should be used in the future. There was an insignificant amount of water intrusion to the main spar of the device from the field deployment. This was most likely due to the imperfect polyurethane seal at the top of the spar.

Other damage to the device was incurred as a direct result of the mooring failure. The heave plate, heave plate mounting rod, and lower intake hose were broken off and not recovered. The inlet PVC elbow of the pump section appeared to break off as a result of interaction with the rocky shore. This included a loss of the inlet check valve (Figure 7.1).

Figure 7.1: Damage incurred to wave pump section's elbow and inlet check valve due to interactions with rocky shore.

The video cameras and solar panels were also not sufficiently rugged to survive the beaching of the device. One of the logo panels installed on the float was lost, likely in the float's interaction with the rocky shore.

Overall, the DAQ module, instrumentation, float buoy, spar buoy, all critical major hardware, and internal pump components survived well throughout the deployment and device beaching. The majority of the device was able to be re-used, and demonstrates survivability through severe ocean wave and weather conditions.

7.3 DAQ Module Performance from Field Test

The DAQ module's power system supplied sufficient power throughout the field deployment period. The batteries were swapped out twice during the field deployment, however this was not necessary. In the weather conditions during the field deployment, the DAQ module's batteries were projected to last a minimum period of 54 days. Details on DAQ module's power performance were included in Appendix D.

One defect of the DAQ module's design was apparent during the field deployment. The plastic lid of the DAQ module became deformed when using a power drill to install and uninstall the closure screws. Additionally, at least one of the screws became stripped during this process when using a power drill. In the future, it is not recommended to use a power drill with plastic parts when out in the field. This was fixed out in the field using a left-handed drill bit and pliers. A spare DAQ module enclosure lid was used to replace the deformed lid. No water intrusion was evident to the DAQ module during the field deployment.

7.4 GPS Time Stamp Processing

The GPS time stamp included in the DAQ module's field data required minimal processing to be useful in the data analysis. This process included a four hour subtraction from the time stamp to convert from UTC to EDT.

To create the most accurate time stamp throughout the data using the GPS, a correction was applied. Since there appeared a lag in the GPS data of several seconds at a time this correction was applied in Matlab. This correction identified the first instance were the second data changed consecutively from one to the next. This instance was chosen as the correct and most accurate GPS time. Using the time array with the most accurate GPS time, the Matlab 'retime' function was applied, with the lidar's sampling rate of 59Hz driving the linear interpolation throughout the twenty-minute time file. Since the GPS accuracy was reported on average as approximately 100 nanoseconds [2], the time stamp instance selected was

accurate to 100 nanoseconds. The rest of the clock accuracy throughout the twenty-minute file then relies upon the Arduino's ability to sample at 59Hz consistently. The Arduino Uno has an internal clock mechanism accurate to 50ppm or 0.06 seconds for each twenty-minute period. However, the correction occurs five times on average each twenty-minute file, so the overall GPS accuracy was ±0.012 seconds at any given time on average. In 54 of the 480 data files, the ability to repeat the correction was not possible. In those instances, an GPS time stamp accuracy of only ±0.06s at any given time can be expected on average.

7.5 Flow Meter Data Analysis

The flow meter records data at a rate of 1Hz. The data files were analyzed using Matlab. The flow meter and lidar data were stored on the same microSD card with a synchronized GPS time stamp in the DAQ module. Because the lidar records at a rate of 59Hz and the flow meter records at a rate of 1Hz, erroneous and extraneous zeros were added to the flow meter data (i.e. 58 per second). The first step in the flow meter analysis was to remove these zero values while preserving the actual zero flow rate data values. Next, outliers were removed from the flow meter data, such that only the 0th to 99th percentile of data remains. This results in an average loss of 0.87% of data, the minimum removal was 0% and the maximum was 1.06% from the 480 twenty-minute files comprising the entire data set when the wave pump was operational (roughly 6.7 days). Outliers were likely caused by electrical anomalies, but their removal does not significantly skew the averaged data, since they comprise on average 0.87% of values. The flow rate time averaged data throughout the wave pump's field deployment were shown in Figure 7.2. There was a gap in the data in Figure 7.2, which represents when the wave pump had turned onto its side and was not operational. The maximum twenty-minute average flow rate for the deployment was 16.53gpm, the minimum was 0.31gpm, and the average was 4.61gpm.

A small section of non-averaged example data was also included in Figure 7.3. This

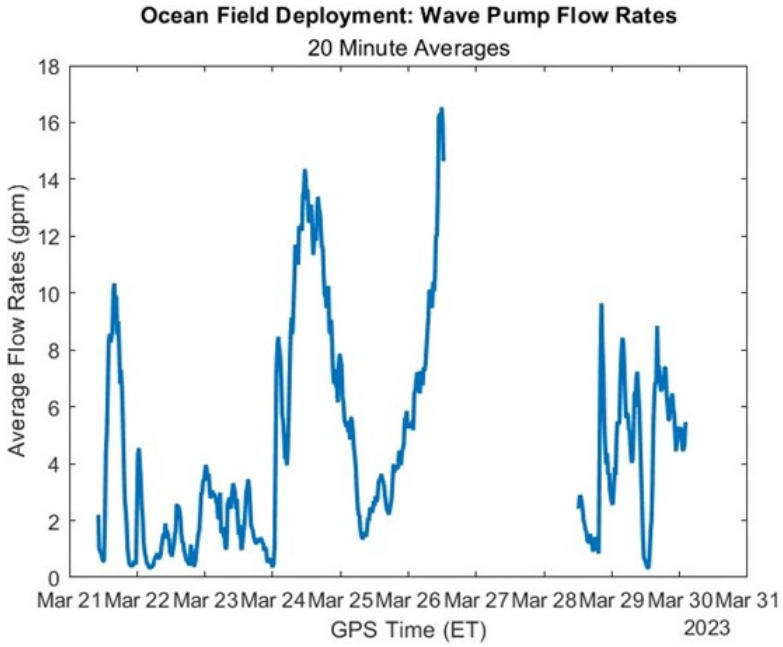

Figure 7.2: Ocean field deployment flow rate values in gallons per minute from the wave pump. Gap in data was attributed to wave pump downtime.

example was a small time series of field data. In the 480 twenty-minute periods that comprise the entire field data set, the flow rate data was averaged in each to produce Figure 7.2.

7.6 Lidar Data Analysis

The lidar and DAQ module records data at a rate of 59Hz. The data recorded was the distance between the lidar sensor mounted to the top of the spar, and the lidar's target which was mounted to the top of the float's gantry. The distance between these two indicates the relative distance between the float and spar. The lidar data was processed using both time series and frequency domain analyses in Matlab. If any values exceeded the maximum distance between the sensor and target (134 centimeters), they were removed from the data set. Values exceeding 134cm were impossible, due to the physical stroke limits of the device, which stayed intact throughout the field deployment. Since the target extents did not move during the deployment, these were the physical bounds of the lidar data. Next, a custom

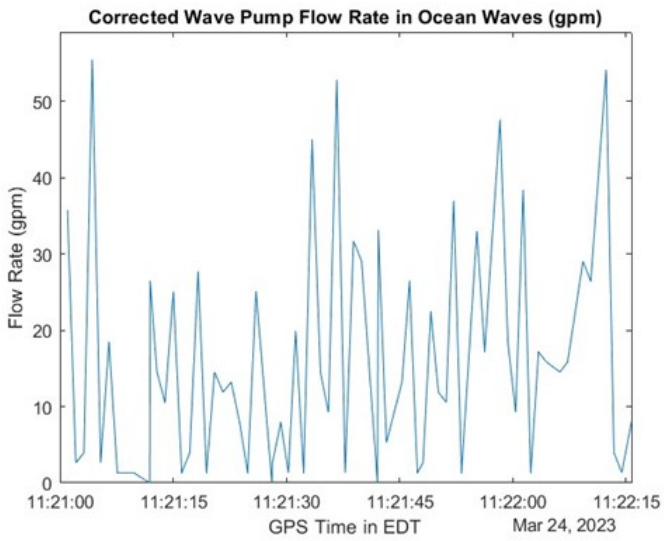

Figure 7.3: Example of corrected flow rate data from field deployment shown in gallons per minute. The sample rate was approximately 1Hz.

digital low-pass filter was applied to the data using the Matlab functions 'designfilt' and 'filtfilt'. Since most of the wave data occurs with periods ranging from 2s to 5s according to the Spotter data, the digital filter was applied using these frequency bounds, and then tuned to get the closest correlation between the Spotter and lidar data. The filter specifications include the least-squares method, with an order of 300, passband frequency of 2.5Hz and a stopband frequency of 5Hz. After filtering, outliers were removed using the function 'rmoutlier' using the moving median method, over a twenty-seven second sample window. The data was then smoothed using the function 'smoothdata', with the Savitsky-Golay filter over a single element window. The Savitsky-Golay filter smooths using a quadratic polynomial, and tends to have higher accuracy for rapidly changing data [57]. The change to a sample time series data segment through this processing method was shown in Figure 7.4.

The next phase of the lidar analysis was finding a metric to compare to the Sofar Spotter buoy data. If the lidar data stroke heights were found, which theoretically correspond to wave heights, and the highest third of these values were averaged together, the result was a metric which can be compared to the Spotter significant wave height data. Using the Matlab

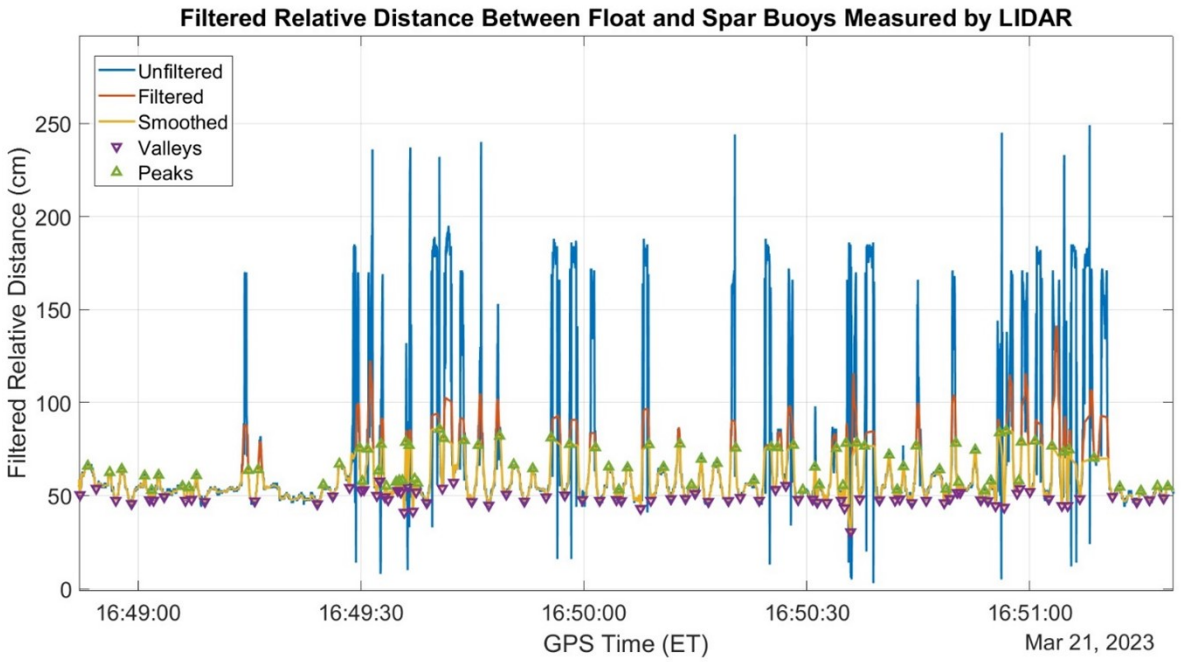

Figure 7.4: Time series example of lidar data segment with processing techniques applied.

'findpeaks' function, and a minimum peak prominence of 4 centimeters, both the peaks and valleys were found in each twenty-minute sample. The minimum peak prominence value was chosen to reflect the waves which would register, or those larger than the sensor accuracy of ± 2 centimeters. Valleys were then subtracted from each previous peak, resulting in a stroke height measurement. If any stroke heights exceed the device limits of 132 centimeters, the data was replaced with 132 centimeters. Out of the 480 twenty-minute samples, this replacement occurs only once with the above processing methods in place (March 28th at 12:34:38).

Finally, the stroke heights highest third values were averaged for a comparable metric to the Spotter data. This comparison was included in subsection 7.10.2, and a correlation calculation was included. Only the significant stroke heights for which less than 10% of the lidar data was removed by the 'rmoutlier' function, and less than 1% was replaced when applying the physical bounds of the possible stroke length were included in the correlation. 417 of the 480 twenty-minute samples (or 87%) match both specifications. After the wave

pump tilted over in the storm, and was subsequently righted, the lidar data do not correlate as well. For this reason, the five-day period from March 21st to March 26th of lidar data will be used in most of the data comparison. More detail on this was included in subsection 7.10.2.

To validate the method used to process the lidar data, four videos taken from the Appledore Radar Tower's webcam were analyzed using image tracking software, Kinovea. These videos were taken all near the same time, on March 26th, 2023, between 11AM and 12PM. Each video was approximately 45 seconds in duration. The wave conditions during this time were some of the highest over the course of the deployment, which allows validation of the lidar measured stroke extents. In Kinovea, the length of the float's gantry, 165.1cm, was used to calibrate the image tracking. Two targets were used, one located approximately at the top of the gantry where the lidar target was located, and one at the top spar plate, where the lidar was located.

Some error was expected in the magnitude of the stroke measurements due to inaccuracy of the image tracking. The videos were taken from approximately 320 meters away, and the wave pump's movement in the waves would cause the image tracking software's calibration to become less accurate. The trajectories for both targets were uploaded to Matlab. By subtracting them from each other, creating an accurate timing vector, and using 'findpeaks' function the average stroke heights of the wave pump were calculated from the video. These were compared to the average processed lidar stroke heights and corresponding average periods. A summary table of these results was included in Table 7.1.

Table 7.1: Summary of image tracked trajectories compared with processed lidar data

Video #	Kinovea Period (s)	Lidar Period (s)	Kinovea Stroke Ht (cm)	Lidar Stroke Ht (cm)	% Diff. Period	% Diff. Stroke Ht
1	2.692	2.718	22.538	30.221	0.96	29.1
2	3.038	3.137	30.416	34.609	3.21	12.9
3	2.747	2.575	25.300	31.859	6.46	23.0
4	2.739	2.550	23.512	31.720	7.15	29.7
Averages	2.804	2.745	25.442	32.102	2.13	23.1

The percentage difference between the Kinovea trajectory stroke periods captured from the radar tower video and the processed lidar data was very small, at an average of 2.13% over the four videos. This indicates that the period captured in the processed lidar data,

and the video were closely correlated. The stroke heights have an average percent difference of 23.1%, which was a more substantial difference. This magnitude difference was expected, given the difficulty of accurately tracking the motion from the video taken far from the wave pump in storm conditions. Additionally, as the wave pump moves in the waves, the image tracking was less likely to maintain an accurate calibration. From this comparison, the methods used to process the lidar data appear to match quantitatively with the image tracked videos, where some variation was expected.

7.7 Sofar Spotter Data Analysis

The Sofar Spotter buoy records many different streams of data. These include a GPS epoch time, latitude, and longitude. It also records the sea surface temperature, wind speed, and direction. Wave motion was measured at a rate of 2.5Hz by capturing displacement in X, Y, and Z coordinate directions from an average location. Over time this average location adjusts to account for drift with onboard filters. The motion data was analyzed using the Spotter Data Parsing Script [46] to correct for phase distortion and recover the sea surface elevation data. The error of the Spotter buoy data was characterized by: "The motion package has a 2cm root mean square (RMS) error in a good signal environment under control conditions. Field errors in significant wave heights were upper bound by 20cm corresponding to errors in the order of 5cm on the signal," [25]. Onboard statistical processing of the wave motion data was also stored on the device, including variance density spectra and co-spectra.

The Z-displacement data was shown in Figure 7.5, where it was trimmed to match the times at which the wave pump device was deployed. The orange color indicates the time when the wave pump was not operational. Most of the wave heights throughout the length of the deployment were approximately 0.3 meters (or 1.0 feet) as shown in Figure 7.5. The maximum wave height captured by the Spotter buoy during the wave pump's operation was 1.5 meters (or 5 feet).

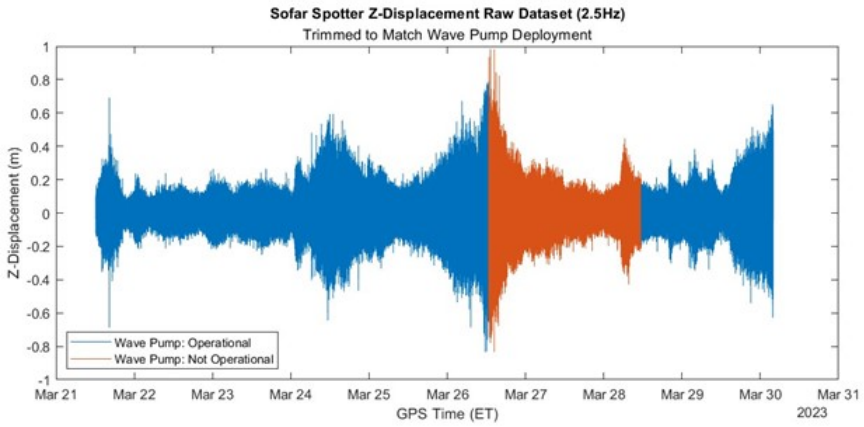

Figure 7.5: Sofar Spotter Z-displacement raw data for length of wave pump deployment.

A shortened subset of Figure 7.5 was included in Figure 7.6, to indicate the nature of the wave elevation data.

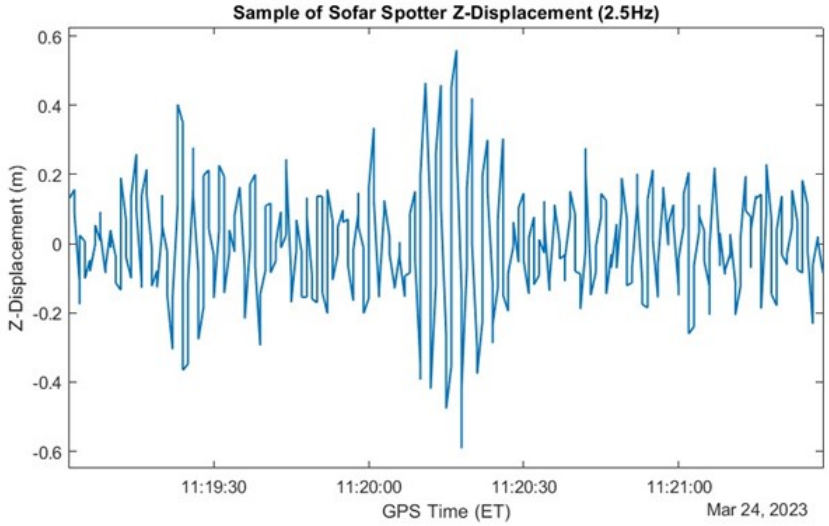

Figure 7.6: 150 second sample of Sofar wave elevation data (2.5Hz).

At a sampling rate of 2.5Hz, the Spotter should accurately capture waves with a period as small as 0.8 seconds according to the Nyquist frequncy sampling principle. In the 30-minute averaged wave statistics, shown in Figure 7.7, the minimum wave period was given as 2 seconds, the maximum was 6.1 seconds, and the average was 3.2 seconds. The minimum significant wave height was 0.26 feet, the maximum was 3.08 feet, and the average was 0.89

feet.

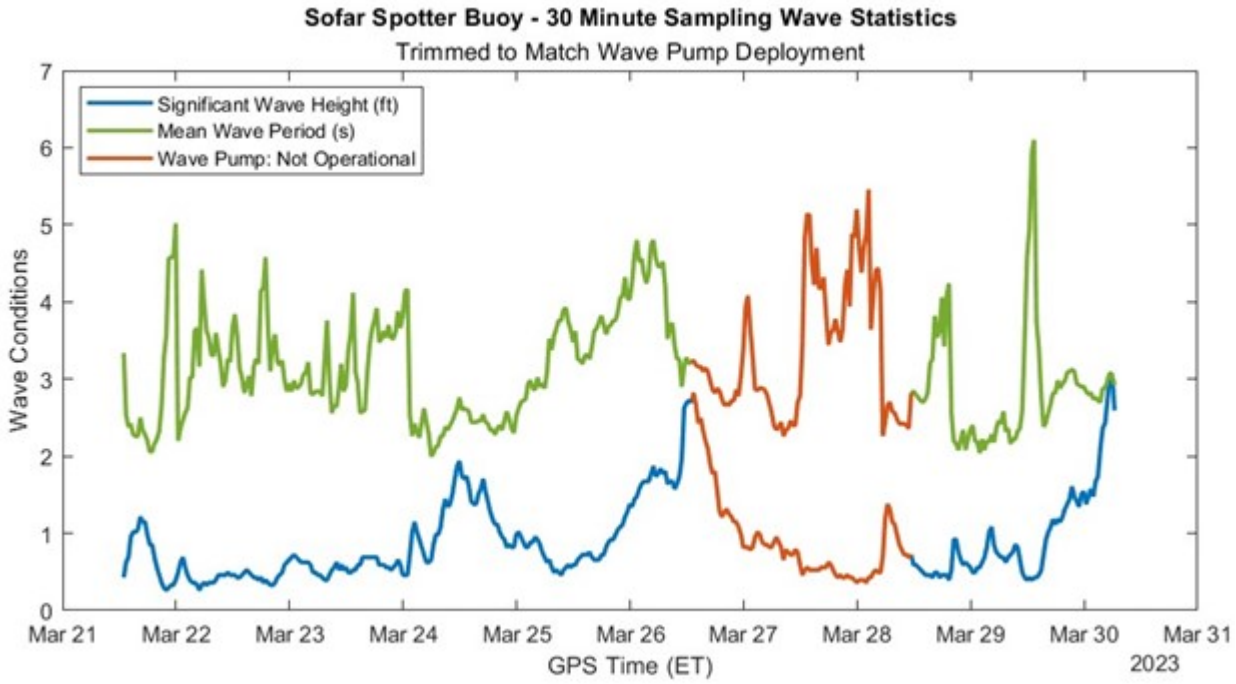

Figure 7.7: Sofar Spotter buoy thirty-minute sampling wave conditions including significant wave height in feet and mean wave period in seconds. Orange location on graph indicates time when wave pump was not operational. Analysis performed using Sofar's spectral density methods.

The Z-displacement data was also analyzed using time series statistical methods, in the same way as the lidar data (i.e., 'findpeaks' Matlab function and averaging the highest third values). To create a better comparison, the data was segmented into twenty-minute sections (instead of thirty-minute sections) to match the lidar data. The difference between the twenty and thirty-minute segments was insignificant throughout the data set. The difference between the spectral energy density method and the time series, statistical method was noticeable. Shown in Figure 7.8, the two methods for analyzing the Spotter data were shown.

The method analyzing the Spotter data in a time series format produced results which were smaller than the spectral energy density analysis. The Z-coordinate, or elevation wave

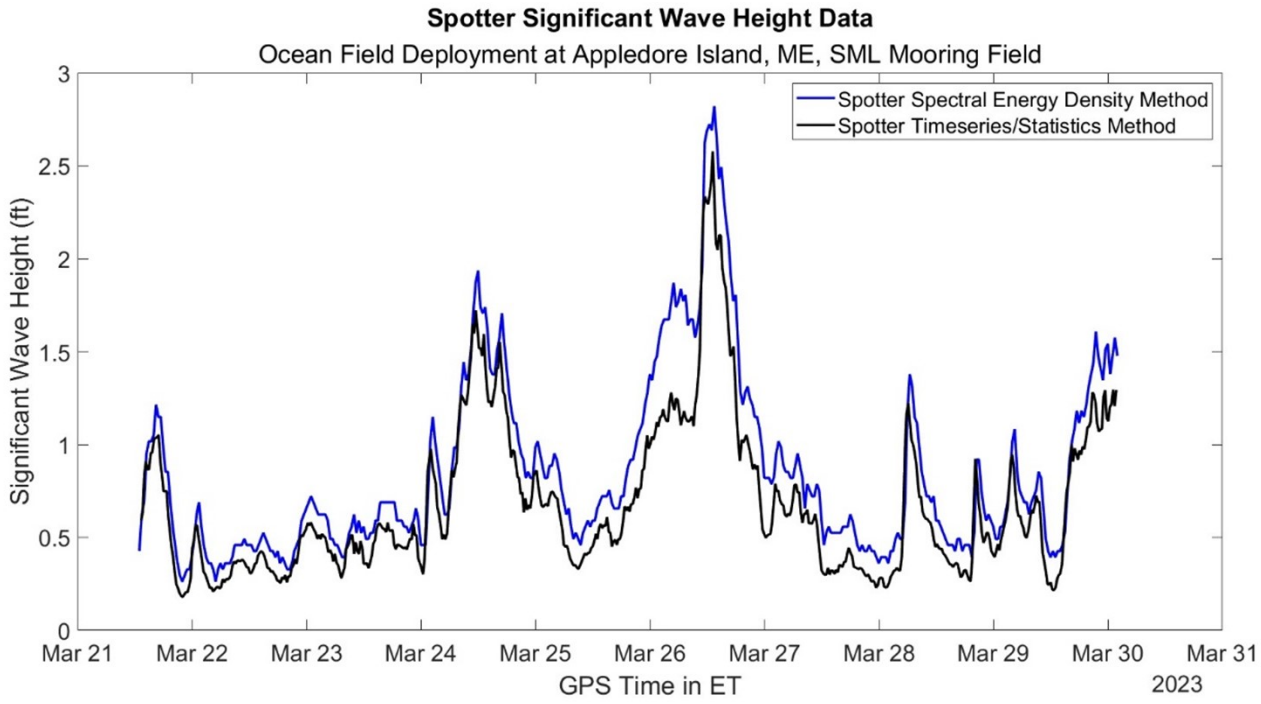

Figure 7.8: Spotter data analyzed two ways: Sofar's spectral energy density and time series/statistical analysis in Matlab.

data from the Spotter buoy was the only input for the time series result. The spectral energy density format used the displacement in the X- and Y-coordinate directions, along with the elevation data, to produce the significant wave height calculation [59]. The results were still closely correlated, with an r-value of 0.97 ± 0.003 (tolerances shown for the 95% confidence interval). The p-values were sufficient to indicate a statistically significant result (equal to 0). In the interest of comparing lidar and Spotter data in the most similar way, data shown in Figure 7.8 on the black line will be compared to the lidar analysis. The most significant difference between the data shown in Figure 7.8 occurs approximately in the mid-morning of March 26th. The explanation for this discrepancy was attributed to the weather conditions at that time. Prior to the wind speed and wave heights increasing from the north-western direction (i.e., directly facing the mooring field), which was accurately captured around noon time, diffracted waves with long period swell from the east were accurately captured in the spectral energy density analysis, but not the time series analysis [60]. Thus, the time series

values appear smaller than the average spectral energy density values for that approximate nine-hour span.

7.8 Hydrophone Data Analysis

The two ST500 hydrophones mounted to the #5 mooring line at an approximate depth of 3-4 meters recorded continuously from March 21st, 2023, beginning at approximately 15:00 ET, and ending on April 3rd, 2023, at approximately 08:00 ET. The sampling rate was 144kHz. After listening to portions of selected files throughout the deployment, it appears that both hydrophones recorded successfully throughout the deployment. The 5600 serial number hydrophone was mounted slightly above the 5592 serial number hydrophone on the mooring line, by approximately six inches. In the few audio files which were reviewed, sounds which were identified include: waves, mooring chains, Spotter mooring swivel and shackles interacting, birds calling, and boat propellers. Several boat propellers correlate with known vessels in the area at the time, whether from the Galen J, R/V Gulf Challenger trips or other boat trips out the island observed on the webcam. A record of known boat trips to the island is included in Appendix E. An unidentified noise was detected through listening to several audio files, which could possibly be the wave pump's piston motion inside the cylinder. This noise has not been comprehensively reviewed or confirmed as belonging to the wave pump. A twenty-seven-second sample was analyzed, where the potential piston noise was identified occurring nine times recorded on hydrophone serial number 5592, March 22nd, 2023, at 09:01:43 to 09:02:10 ET. Through signal spectrum analysis [72] the potential piston sound occurred at 356Hz at a magnitude of -65dBV^2. The signal was detrended and normalized about peak unity during the analysis (Figure 7.9). The magnitude of this sound was 15dBV^2 lower than the peak observed at 30 to 40 Hz. The peak at 30 to 40 Hz was likely the ambient noise conditions present in the mooring field, indicating this sound was less than ambient noise conditions.

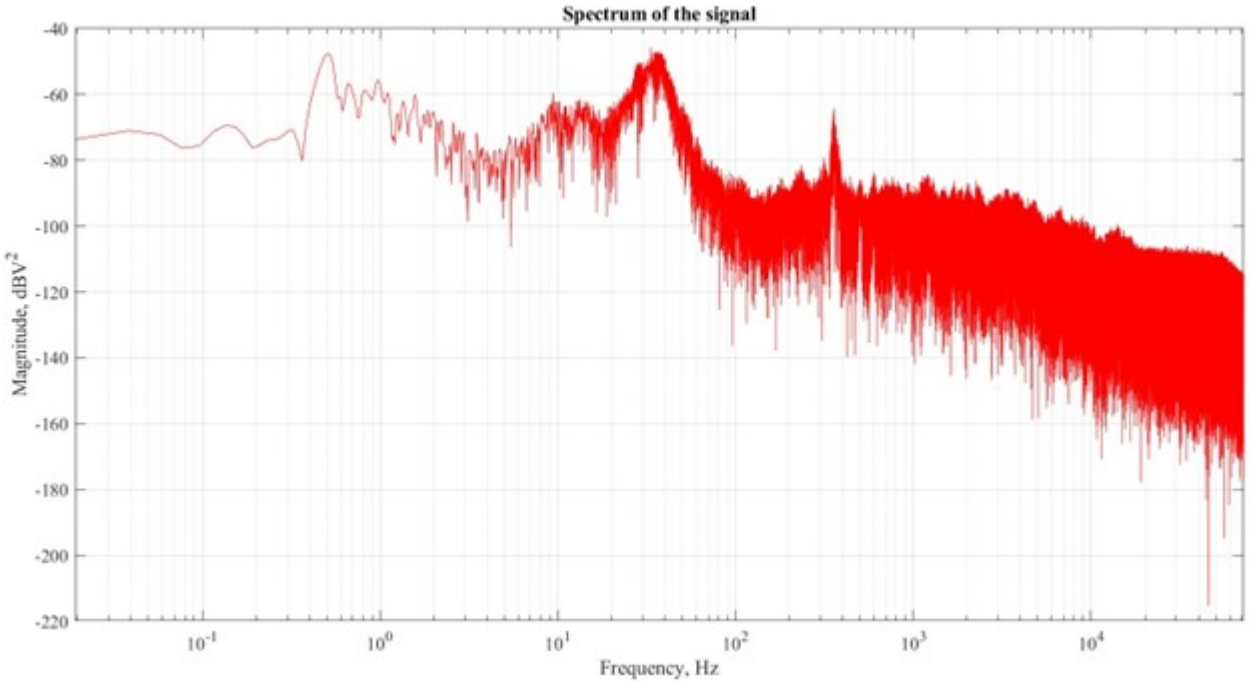

Figure 7.9: Potential noise from the wave pump piston recorded during deployment from hydrophone 5592 on March 22nd, 2023, at 09:01:43 to 09:02:10 ET.

A more comprehensive review of the hydrophone data is required to determine whether these sounds can be attributed to the wave pump. Additionally, a more thorough review and processing of the data should be conducted to determine whether marine mammals were present in the area during the deployment, and whether the wave pump had any considerable effect on those marine mammals. This determination can aid in future environmental permitting efforts. The hydrophone data were approximately 700GB in size, and were kept on a separate solid state drive device at the Jere A. Chase Laboratory.

7.9 Onboard Device Video Data Analysis

The motion-triggered video cameras attached to the top of the device intermittently recorded from March 21st to March 29th, 2023. Two cameras were installed onto the top of the float gantry, facing downwards at an angle to capture the waves near the device and a partial view of the float. Most of the captured footage shows the surrounding wave conditions, and on

instances with larger waves typically more videos were captured. The videos were reviewed at twice normal speed. Both adult and juvenile herring and black back gulls occasionally interacted with the wave pump and mooring. Interactions included foraging and roosting behavior. No gulls appeared harmed during these interactions. For future field deployments, durable and non-toxic materials should be used with consideration for gull interactions. In Figure 7.10, some screenshots were shown from the gull interaction videos.

In certain wave conditions, the mooring was observed causing a repeated, fast semi-rotation of the wave pump. As the large waves pass by, in the trough the mooring lines were slack, and then when another crest passes a jerking motion on the mooring lines caused an approximate 90-180° partial rotation about the spar buoy's vertical axis. This was observed in the cameras several times throughout the deployment. This observation indicated that future mooring systems for this device should have a three-point system to reduce wear. A detailed list of observations and additional screenshots from the video data were included in Appendix F.

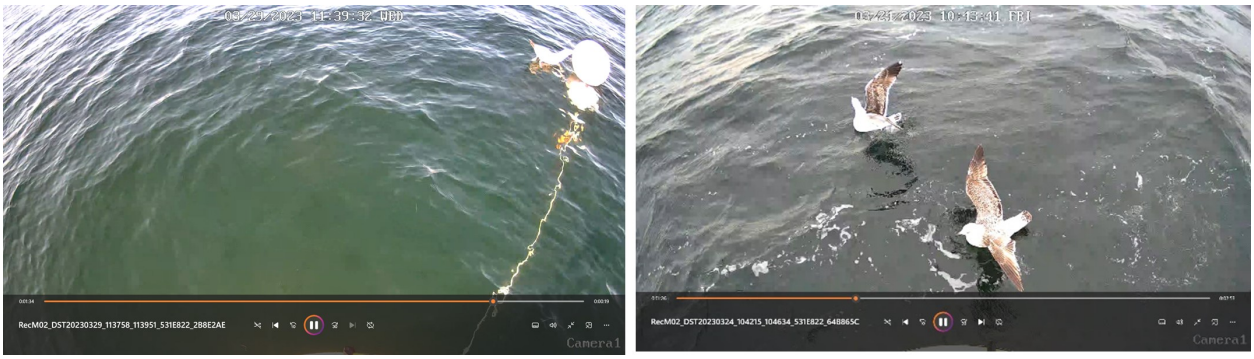

Figure 7.10: Juvenile herring gulls interact with wave pump float.

7.10 Data Correlations

7.10.1 Flow Meter and Spotter Comparison

The flow meter data appeared to consistently respond to the wave forcing throughout the deployment period. In Figure 7.11, the twenty-minute averaged Spotter data was analyzed

using a time-series approach to determine significant wave height in feet. Compared against this data was the flow meter data, also averaged in twenty-minute increments, in units of cubic meters per hour. The units were intentionally chosen to best reflect the visual relationship between the wave heights and flow rate, despite one set being in feet and another in meters. After the device was righted, the flow meter data maintains a strong correlation with the significant wave height data, however it was less strong of a correlation (Figure 7.11). The r-value correlating the flow rate to the significant wave height data for the period of March 21st to the 26th was 0.94 ± 0.01 with a p-value of 5.9e-164. This was a very strong positive correlation, indicating that in larger waves, the flow rate of the device was increased. After the device was righted, for the period of March 28th to March 30th, the r-value decreased somewhat to 0.71 ± 0.1 with a p-value of 6.1e-19.

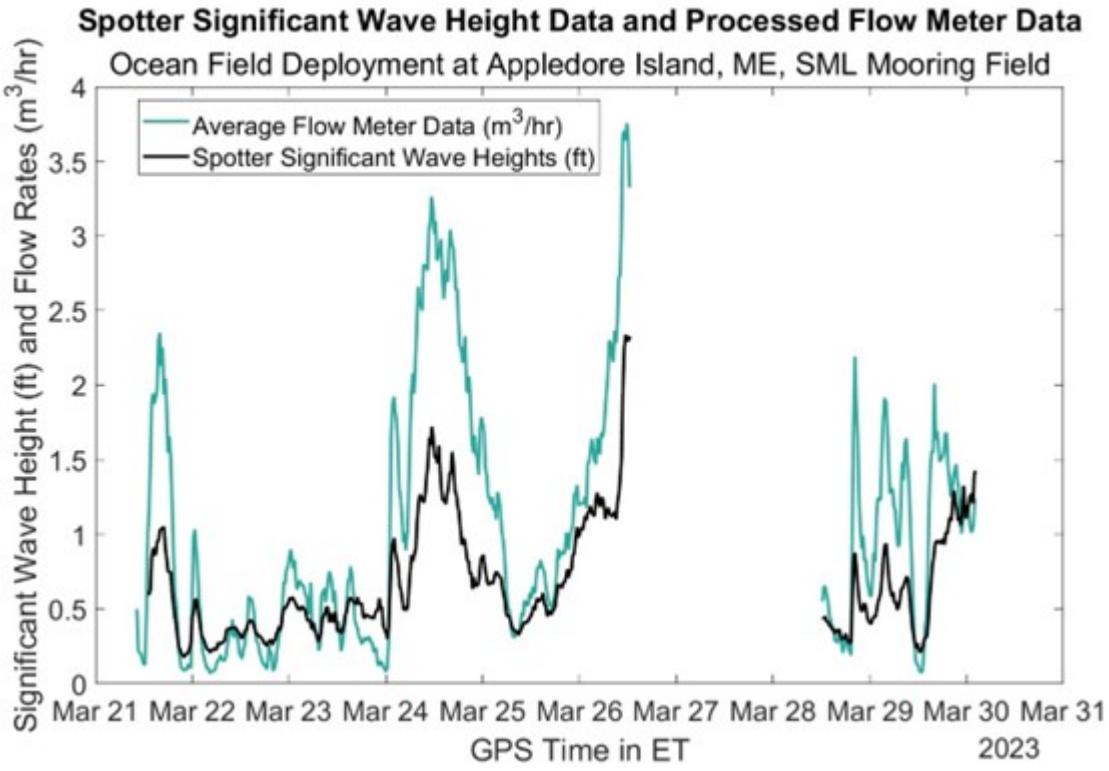

Figure 7.11: Spotter significant wave heights in feet for twenty-minute averages, analyzed using time-series approach compared with twenty-minute averages of flow meter data in cubic meters per hour. Missing portion of graph attributed to wave pump in-operation.

It was unclear what caused this decrease in correlation, but could be related to the lidar's similar issue. An electrical issue in the DAQ module may have caused imperfect flow meter data during this period; however, upon returning to the lab both the flow meter and DAQ module performed similarly in the calibration as they had prior to deployment. Another potential cause of the decrease in correlation may be due to physical change to the device. For example, pumping would be inhibited due to an increase in friction between components that were worn or damaged in saltwater. Upon returning to the lab, components of the device were examined, without obvious evidence of any defects in the device.

7.10.2 Lidar and Spotter Comparison

Lidar data in Figure 7.12 which was represented by the orange "*" symbol indicates that it was comprised of data for which less than 10% was removed during the 'rmoutlier' function, and less than 1% was removed during the initial bounding adjustment. These 417 twenty-minute averaged points were compared with the Sofar Spotter twenty-minute averaged significant wave heights for the same period (shown by the black line). The correlation between these two sets of data was a moderate to strong positive correlation before the device tips over on March 26th, and a moderate to strong negative correlation after the device tips over. The r-values before and after the device tips over were 0.79 $\pm$ 0.04 and -0.69 $\pm$ 0.10 respectively. The p-values for both correlations indicate statistical significance (2.4e-74 and 4.3e-17 respectively). The strong positive correlation before the device tips over indicates that the wave pump device was both responsive and dynamically efficient in a range of wave conditions. Since the Spotter buoy was measuring wave height, and the lidar was measuring relative distance between two floating bodies, the values were not expected to perfectly correlate or match. The negative correlation after the device tips over suggests an issue with the lidar data quality. The lidar was calibrated after the deployment, without reproducing any inverse relationship as seen in the field data. It was unclear why the lidar malfunctioned during this time of the field deployment (from March 28th to March 30th). It was possible

an electrical connection within the DAQ module was maligned in some way during the field deployment but was subsequently fixed upon returning to the lab. The lidar target was mounted to the float buoy's gantry, and if during the deployment it became misaligned with the lidar sensor, this may have caused the errors seen in the data.

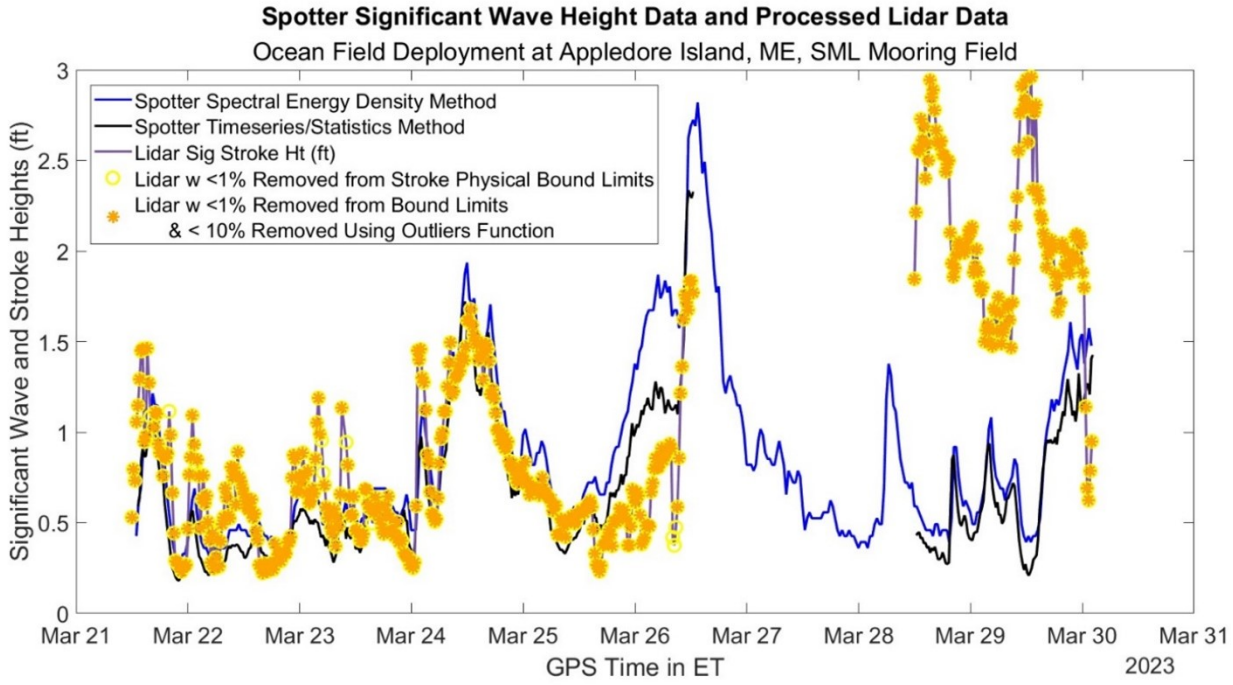

Figure 7.12: Processed lidar data shown as significant stroke height with Spotter significant wave heights analyzed in two ways. Quality of lidar data shown with symbols.

7.11 Device Performance Characteristics

7.11.1 Relative Motion RAO

The relative motion Response Amplitude Operator (RAO) for the system was calculated by using only the data prior to the wave pump turning over in the field (period between March 21st and March 26th). Three distinct twenty-minute data files of lidar relative distance data, all corresponding to different wave state conditions were chosen to perform the RAO analysis. The data were equalized about the zero point by subtracting 63.8cm from each entry. 63.8cm

was determined to be the equilibrium zero point by examining the data with the calmest wave conditions, and finding the most common value. The data was also converted from centimeters to meters for comparison to the Spotter data. The Spotter elevation data (in meters) was compiled into a twenty-minute segment with synchronous time to the lidar data. A spectral energy density analysis for both the lidar and Spotter data sets was completed using the 'pwelch' function in Matlab [50]. The relative motion RAO was produced using:

$$RAO = \sqrt{\frac{S_{relativedistance}}{S_{wave}}}, \tag{7.1}$$

[64] where:

$S_{relativedistance}$ = Spectra from lidar data

S_{wave} = Spectra from the Spotter data.

The spectral energy from the lidar and Spotter data were used in Equation 7.2 to calculate relative motion RAO, which was then plotted against the spectral frequency. Since the Spotter's sampling rate was slower than the lidar, the Spotter's maximum frequency was used to truncate the lidar's spectral energy density. The Spotter's sampling rate was 2.5Hz, and using the Nyquist frequency, a maximum frequency of 1.25Hz was used in this analysis.

The three RAO's from different 20-minute compilations were shown in Figure 7.13. Each plot indicates the date and time for the beginning of each file, as well as its corresponding Spotter measured significant wave height and wave period. These three plots appear to be similar in form and magnitude. Two major peaks occur on the smoothed plot, at approximate wave periods of 2.9 seconds (or a frequency of 0.35 Hz) and 8.3 seconds (0.12 Hz). These peaks occur mainly in the larger wave states. In the smaller wave condition, the response was markedly more damped. This indicates that the greatest relative motion in the wave pump occurs in wave periods of 2.2 seconds for the given field data in larger wave conditions. There was a gradual tapering of the RAO at frequencies higher than 0.45Hz, indicating that as wave periods become smaller, there was a similar, but slightly smaller heave response in

the system. At the lower frequencies, the heave RAO maintains a level above one for wave periods greater than fourteen seconds, even for the smallest wave condition observed in this comparison. At wave periods beyond fourteen seconds, there was a rapid drop in RAO, suggesting little relative motion occurs in the system due to wave periods beyond fourteen seconds. In addition to plotting the three relative motion RAO responses in Figure 7.13, a smoothed version of each result was also plotted together (see bottom right). This smoothed RAO allows a visual comparison of the three RAO's. Since these smoothed RAO's closely align, while representing different sea states, this was an indicator of the wave pump device's linearity.

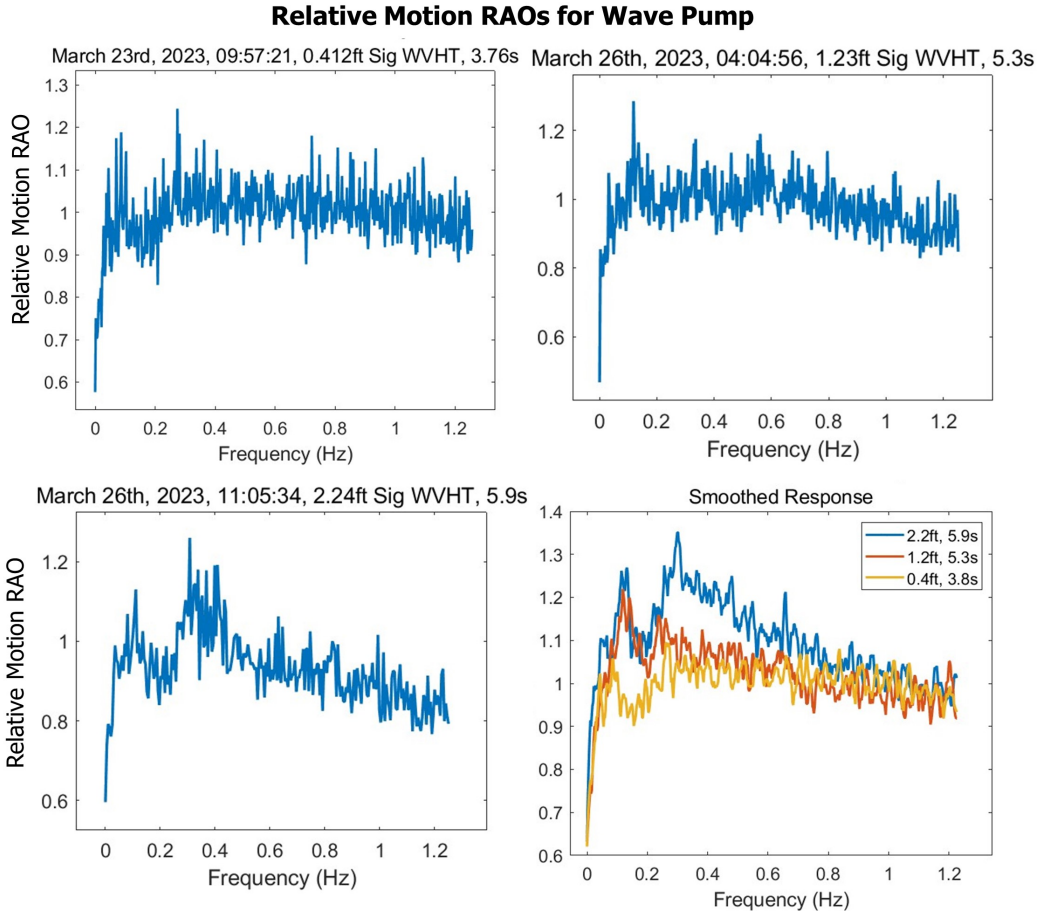

Figure 7.13: Relative motion RAO for wave pump from March 2023 field deployment, three different wave conditions represented (top and bottom left). Smoothed plot of all three RAO's (bottom right).

7.11.2 Performance Map

To begin characterizing the performance of the wave pump device in various wave conditions, the average flow rates measured for given significant wave heights and periods were shown in Figure 7.14. Only wave periods of less than seven seconds were chosen to be represented in this performance map. A clear positive trend was apparent between greater wave heights and increased flow rate, which confirms the correlation between these two data sets. Given the limited amount of twenty-minute averaged files (approximately 350), the trends for period were less clear in Figure 7.14. With additional data collected in more various wave conditions, the performance map can be more fully evaluated.

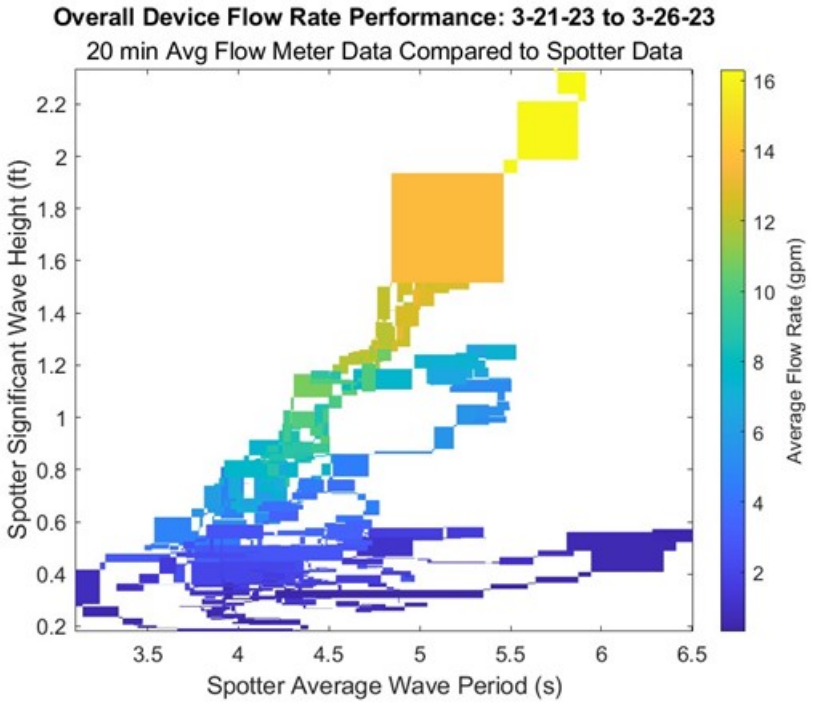

Figure 7.14: Performance map for wave pump device which shows pumped volume flow rates in given wave conditions including period and significant wave height from Spotter device.

The Spotter significant wave heights were plotted against the flow rates for each twenty minute average set, for the first five days of field data. These were plotted in a loglog format to ascertain whether a power law, or linear relationship in log format, exists between the

two data sets. In Figure 7.15, the field data is shown along with a line plotted with a power of two.

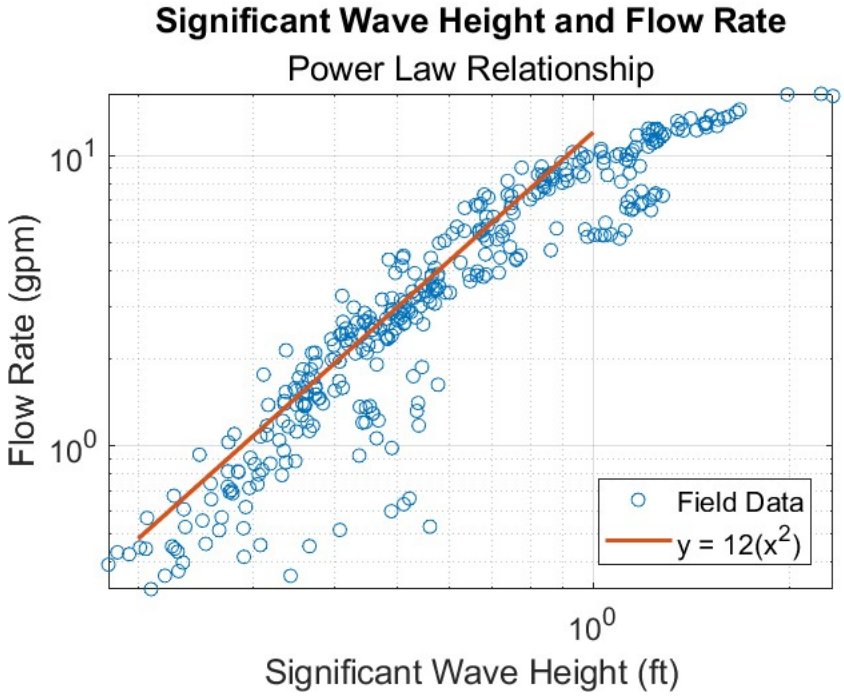

Figure 7.15: Relationship between significant wave height (shown in feet, from Spotter buoy) to the synchronous average flow rates (shown in gpm). Additional line plotted with a power of two relationship to indicate proportionality between significant wave height and flow rate.

The equation representing the fit line on Figure 7.15 was:

$$y = 12(x^2), \tag{7.2}$$

where:

y = corresponding flow rates

x = Spotter significant wave heights.

For significant wave heigts between 0.2 and 1.0 feet, the field data closely aligns with the equation shown on Figure 7.15. This indicates that the relationship between significant wave heights and flow rate is proportional to a power of two, for the segment of the field data with 0.2 to 1.0 significant wave heights. Since the available power in the waves is also

proportional to significant wave height with a power of two relationship, it follows that the energy used to pump water and produce a flow rate would have a similar relationship.

7.12 Efficiency

The efficiency of the wave pump device was calculated using the field data from the period of March 21st through March 26th. The average flow rates for each twenty-minute period of data were utilized in these calculations. The Spotter wave condition data were also used to determine the theoretical available power for the calculation. The device efficiency was calculated using:

$$Efficiency = (\frac{PumpPower}{PowerAvailable}) \times 100. \quad (7.3)$$

Two additional expressions represent Pump Power and Power Available, which substitute into Equation 7.3 to complete the expression.

$$PumpPower = Q \times \rho \times g \times h \quad (7.4)$$

[49], and

$$PowerAvailable = \frac{\rho \times g^2 \times T \times H^2}{32\pi} \times \phi_{float} \quad (7.5)$$

[19], where:

Q = Average Volume Flow Rate, m^3/s (varies, from flow meter field data)

ρ = Density of seawater = 1025 kg/m^3

g = Gravitational acceleration = 9.81 m/s^2

T = Wave Period, seconds (varies, from Spotter field data)

H = Significant Wave Height, meters (varies from Spotter field data)

ϕ_{float} = Diameter of the float buoy = 1.524 m.

The equation Equation 7.5 assumed that the waves are regular (single-frequency), whereas in the field, the waves are irregular (form a spectra). To increase the accuracy of this efficiency calculation, the equation to represent power available from a spectrum of waves should be used.

In Equation 7.4, h represents all the major and minor losses in the wave pump device. This value was also calculated separately for each twenty-minute data file, based on the average flow rate. Additionally, it was also calculated separately depending on which region of the device the water was moving through. These were condensed into two main sections: hose and PVC, where the hose had a diameter of roughly 0.053 meters and the PVC had a diameter of roughly 0.102 meters. The expression for h, total losses was given by:

$$h = \Sigma MajorLosses + \Sigma MinorLosses \quad (7.6)$$

[49]. The expressions for major and minor losses were:

$$MajorLosses = f_d \times \frac{L}{D} \times \frac{V^2}{2g}, \quad (7.7)$$

and

$$MinorLosses = k_{total} \times \frac{V^2}{2}, \quad (7.8)$$

[49] where:

h = total losses, meters

V = Velocity of water (used average flow meter data divided over corresponding pipe area)

L = Length of pipe (varied)

D = Diameter of pipe (varied).

A table with a comprehensive list of lengths and diameters of pipes were included in Appendix G.

The Colebrook-White function [16] in Matlab was used to determine the f_d value. This function required the Reynolds number and relative roughness value inputs. The Colebrook equation is:

$$\frac{1}{\sqrt{f_d}} = -2.0 \times log(\frac{\frac{e}{D}}{3.7} + \frac{2.51}{Re \times \sqrt{f_d}}), \quad (7.9)$$

[49]. The Reynolds number was calculated separately for each twenty minute period and for each section of the device. Reynolds number, Re, is represented by:

$$Re = \frac{\rho \times V \times D}{\mu_{sea}}, \quad (7.10)$$

[49] where:

e = absolute roughness of PVC = 1.524e-6 m [49]

μ_{sea} = viscosity of sea water at 40°F = 0.00167 $\frac{Ns}{m^2}$ [63]

The k_{total} value of 7.53m was estimated using reference values from [49]. The features of the wave pump device included: inlets, reductions, enlargements, check valves, elbows, and

a tee-fitting. The k values for all of these features were added together to estimate the k_{total}. A table is included in Appendix G for these calculations.

This estimation of major and minor losses does not perfectly capture the losses occurring within the pump, due to its piston chamber. Future work may involve measuring the actual pressure differential across the pump to obtain more accurate efficiency calculations.

The average device efficiency for the five days at sea was 0.1% with the maximum efficiency value occurring in the greatest wave height condition of 0.5% (Figure 7.16). While these efficiencies were low, they indicate that there was significant room for improvement in the wave pump design. The ability to pump more water, given the available wave power, was extensive.

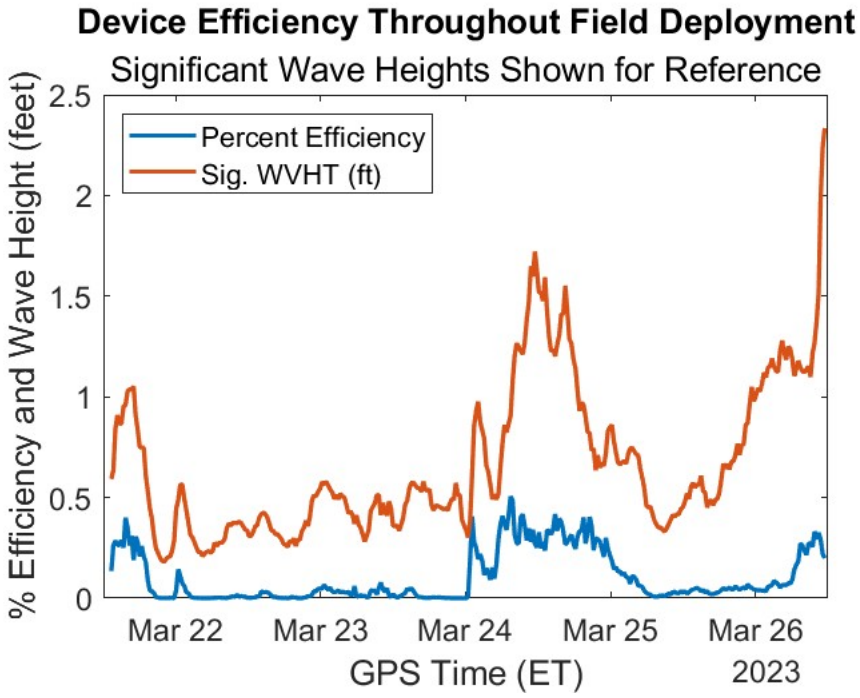

Figure 7.16: Calculated device percentage efficiency throughout the field deployment, shown alongside significant wave heights in feet measured by the Spotter buoy.

CHAPTER 8

Validation of WEC-Sim Numerical Model Using Field Data

8.1 Overview of Methods

To validate the WEC-Sim numerical model, the Z-direction elevation data from the Sofar Spotter buoy was used as an input for the wave conditions to the model. Only data from the first five days of field data (file numbers from 1 to 365) were considered for the analysis to achieve the most accurate results.

The WEC-Sim numerical models were set up to run with each Spotter elevation data in batches of seven and nine on the UNH's Premise High Performance Computing (HPC) cluster. Computations were performed on Premise, a central, shared HPC cluster at UNH supported by the Research Computing Center and PIs who have contributed compute nodes. Each simulation had a run time on the Premise cluster of approximately six days. Given the shared resource of the Premise cluster, a limited number of WEC-Sim simulations were chosen. Twenty-minute field data files which had a range of wave heights and periods were selected to be simulated in WEC-Sim, to provide validation for a range of wave conditions.

The result from each WEC-Sim run was analyzed using a custom Matlab script. The inlet and outlet flow rates from the check valves, and the relative position between the float and spar were the two major data results from each WEC-Sim trial. A shortened example graph for inlet and outlet flow rates from a WEC-Sim trial is shown in Figure 8.1. Similarly to the regular wave generated WEC-Sim flow rate example, as the inlet valve experiences flow, the outlet valve remains closed (i.e. has zero flow rate). The flow rate peaks and durations were no longer consistent throughout the sample, which reflects the wave state

observed in the field.

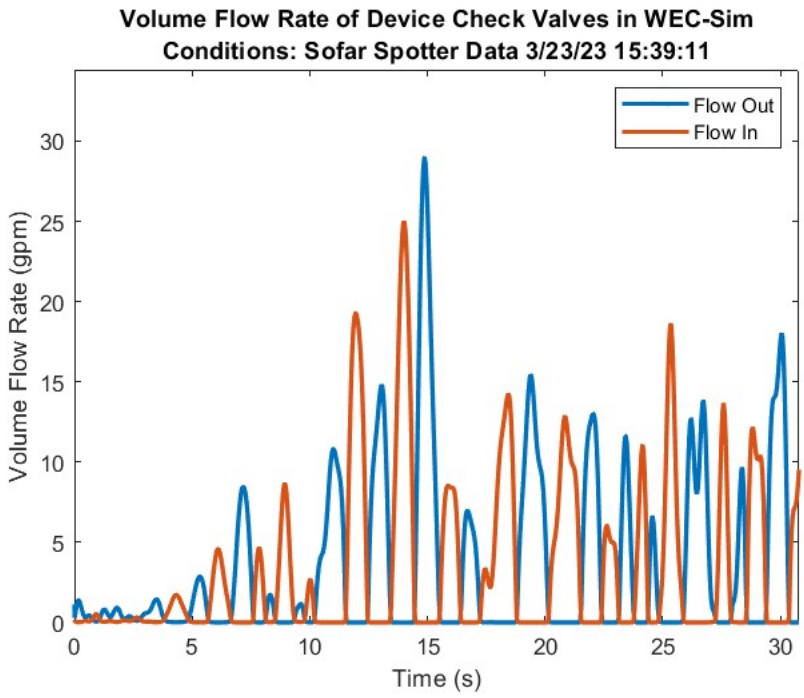

Figure 8.1: Thirty second example of WEC-Sim simulated instantaneous inlet and outlet flow rates in gallons per minute.

For each WEC-Sim sample (up to twenty minutes), the total pumped volume was calculated using Matlab's 'trapz' function, which performs a trapezoidal numerical integration using the simulation time and the outlet flow rate data. The total pumped volume value was then divided by the total elapsed time of the simulation to determine the average flow rate in gallons per minute.

To ensure accuracy of the model (and its ability to follow principles of mass conservation), the total pumped volume from the inlet was compared to the outlet for all sixteen trials. This calculation was performed again utilizing the 'trapz' function for both the inlet and outlet flow rate data. The difference between the inlet and outlet total pumped flow was then calculated. The average difference in pumped volume for all sixteen trials was 0.17 gallons. This value was small compared to the volumes of water pumped during each trial, and thus exhibits conservation of mass in the numerical model.

A thirty second example graph for the relative position between the float and spar buoys is shown in Figure 8.2. The position was shown in feet, with major peaks identified.

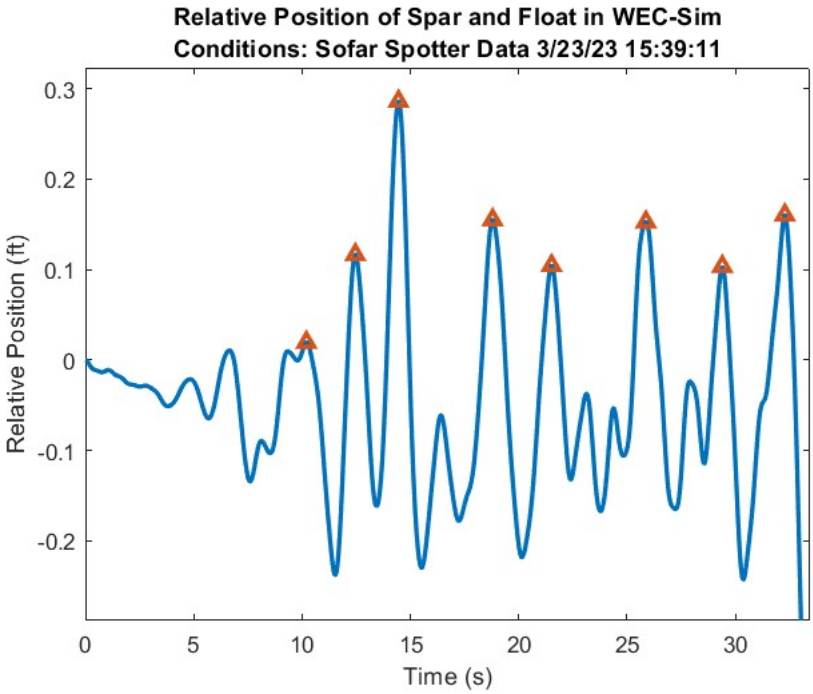

Figure 8.2: Thirty second example of WEC-Sim simulated relative position between float and spar in feet.

The average stroke height was calculated from each WEC-Sim run in a manner similar to calculating the lidar stroke heights. The relative position simulated data were evaluated for peak and valley values and locations using the Matlab 'findpeaks' function. A minimum prominence of four centimeters was chosen to match the method used in the lidar analysis. Using the peak and valley information, valleys were subtracted from previous peaks throughout the vector. Then these stroke heights were averaged together. The WEC-Sim relative position data was output in meters, so a conversion to feet was included.

The average stroke period was determined using the information obtained in the 'findpeaks' operation. The locations for each peak were subtracted from the previous value to yield the wave periods from the WEC-Sim simulation. These values were then averaged to determine average stroke period. The units for average stroke period were in seconds.

The WEC-Sim simulations were submitted in two separate batches of seven and nine. The first seven simulations were all identical in WEC-Sim set-up code, with only the input of wave elevations varying from file to file. These seven all had a Simulink model constraint with six degrees of freedom (6 DOF) for the spar body. The next nine simulations differed in that the spar constraint was changed to fixed.

The start times for each trial number and corresponding wave conditions were included in Table 8.1 for reference. Additionally, the length of time for which WEC-Sim was able to simulate each twenty-minute wave condition file accurately was included as 'WEC-Sim Time.'

Table 8.1: WEC-Sim and Field Data Trial Start Times and Wave Conditions

Trial #	Start Time (ET)	Sig. WVHT (ft)	Wave Period (s)	Constraint	WEC-Sim Time
1	3/21/23 17:19	0.91	2.3	6 DOF	490 seconds
2	3/22/23 00:59	0.56	2.4	6 DOF	1190 seconds
3	3/23/23 05:55	0.41	2.8	Fixed	1190 seconds
4	3/23/23 09:57	0.41	2.7	Fixed	1190 seconds
5	3/23/23 10:57	0.41	3.2	Fixed	1190 seconds
6	3/23/23 15:39	0.56	2.6	6 DOF	545 seconds
7	3/24/23 08:00	1.20	2.3	6 DOF	675 seconds
8	2/24/23 09:07	1.23	2.4	Fixed	1190 seconds
9	3/24/23 14:09	1.23	2.5	6 DOF	309 seconds
10	3/24/23 14:41	1.20	2.4	Fixed	1190 seconds
11	3/25/23 20:04	0.68	3.7	6 DOF	235 seconds
12	3/26/23 04:04	1.23	4.5	Fixed	1190 seconds
13	3/26/23 10:45	1.99	3.0	Fixed	1190 seconds
14	3/26/23 11:05	2.24	3.0	Fixed and 6 DOF	1190 and 85 seconds
15	3/26/23 12:05	2.29	3.3	Fixed	1190 seconds

Calculating percent differences between WEC-Sim results and field data was completed by:

$$\%Difference = \left(\frac{(Value1 - Value2)}{\frac{Value1+Value2}{2}}\right) \times 100, \tag{8.1}$$

Relative motion RAO's were calculated for the field and WEC-Sim data, utilizing the Spotter wave conditions data for both. A smoothed version of the RAO's were used for visual and statistical comparison.

The correlation between the two smoothed relative motion RAO's was found using Mat-

lab's 'corrcoef' function. Some RAO vectors were resampled to match vector lengths. The 'corrcoef' function in Matlab is governed by:

$$p(A,B) = \frac{1}{N-1}\sum_{i=1}^{N}(\frac{A_i - \mu_A}{\sigma_A})(\frac{B_i - \mu_B}{\sigma_B}), \tag{8.2}$$

[18] where:

p = Correlation coefficient

N = Number of observations

A,B = Smoothed RAO vectors for field data and WEC-Sim

μ = mean deviation

σ = standard deviation.

Root-mean-square (RMS) deviation was also calculated for each trial's set of relative motion RAO's, to determine the similarity between simulated and field results. The Matlab function 'rmse' was used for this calculation, and is governed by:

$$E = \sqrt{\frac{1}{n}\sum_{i=1}^{n}|A_i - F_i|^2}, \tag{8.3}$$

[51] where:

E = Root-mean-square deviation

n = Number of observations

A,F = Smoothed RAO vectors for field data and WEC-Sim

8.2 WEC-Sim Results and Discussion

With the 6 DOF constraint, there were errors in six of the seven simulations associated with the results after a varying amount of time. Prior to the errors occurring, the flow rate and relative position results appear to be accurate. These errors were attributed to the lack of simulated mooring and balanced hydrostatics in the model. In larger wave states the errors

occur sooner. To produce simulation results to match the twenty-minute field trial run times, the fixed spar constraint was applied to the next nine WEC-Sim trials.

Averages of flow rate, stroke height, and stroke period were calculated from each WEC-Sim simulation. Each of these average values from the WEC-Sim model simulations were compared with their synchronous average values from the flow meter and lidar field data. The summary plot which contains these sixteen average comparisons is in Figure 8.3. For trial number fourteen, the same file was run with both spar constraint conditions: 6 DOF and fixed.

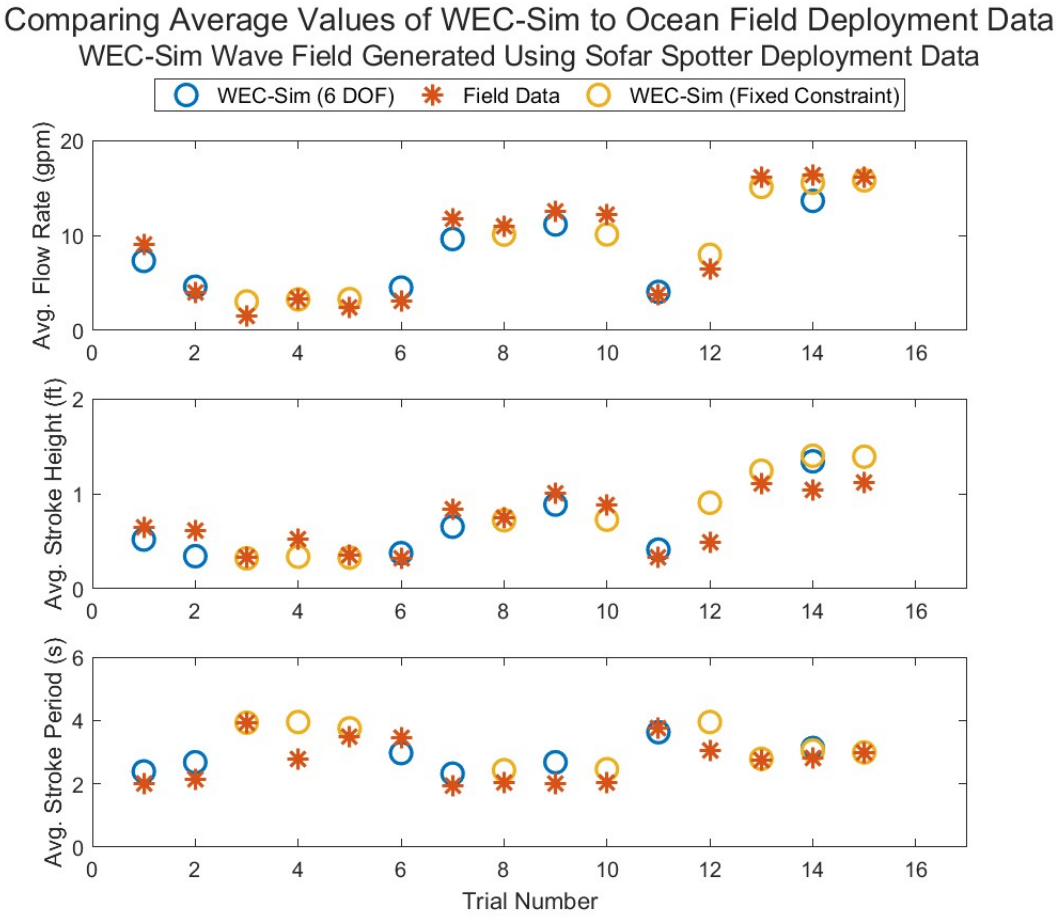

Figure 8.3: Comparing average values of WEC-Sim numerical model to corresponding ocean field deployment flow meter and lidar data. The WEC-Sim wave fields for each trial were generated using the Sofar Spotter field data.

Figure 8.3 indicates a consistently close relationship between the field data and WEC-Sim simulations for average flow rate, stroke height (or relative position), and stroke period. Amongst the sixteen trials average percent differences were calculated to indicate the accuracy of the model relative to the field data. The flow rate average percent difference between the WEC-Sim model and the field data was 18.8%. The example calculation for percent difference is shown in Equation 8.1. This indicates that the field data collected agree with the numerical WEC-Sim model with an average difference of 18.8%. The same average percent difference calculation was performed for the stroke heights, which yielded agreement with an average difference of 22.1%. The average stroke period had an average percent difference amongst the sixteen trials of 15.6%. These low average percent differences indicate that the WEC-Sim numerical model was similar to the collected field data for the device. A table with all average values from the WEC-Sim and field data comparison is included in Appendix H.

8.2.1 WEC-Sim Relative Motion RAO's

The position data from the WEC-Sim model simulations were also analyzed for relative motion RAO, and compared to the lidar field data relative motion RAO. This motion comparison in the frequency domain was an indicator of accuracy for the WEC-Sim model. Figure 8.4 is an example of a relative motion RAO comparison between the WEC-Sim and lidar field data for the 6 DOF constraint. The relative motion RAO plots match consistently throughout the frequency range. Two main peaks occur, the smaller one at 0.05 Hz (or twenty second wave periods), and the largest peak occurs at 0.42 Hz or (2.4 second wave periods). These peaks match closely at the frequency and at magnitude. This indicates that the most relative motion was seen at waves of 2.4 seconds, and that the result from both WEC-Sim and the field data was consistent. A smoothed result was shown for both cases as a visual aid in determining trends. The smoothed result was obtained by using the Matlab function 'smoothdata', which calls a Savitsky-Golay filter over a twenty element sliding window [57]. At very low frequencies, the WEC-Sim and lidar field data RAO's tend

to match, indicating that for both the simulation and in the field the float and spar both act as wave followers at very low frequencies. This behavior was expected for this design.

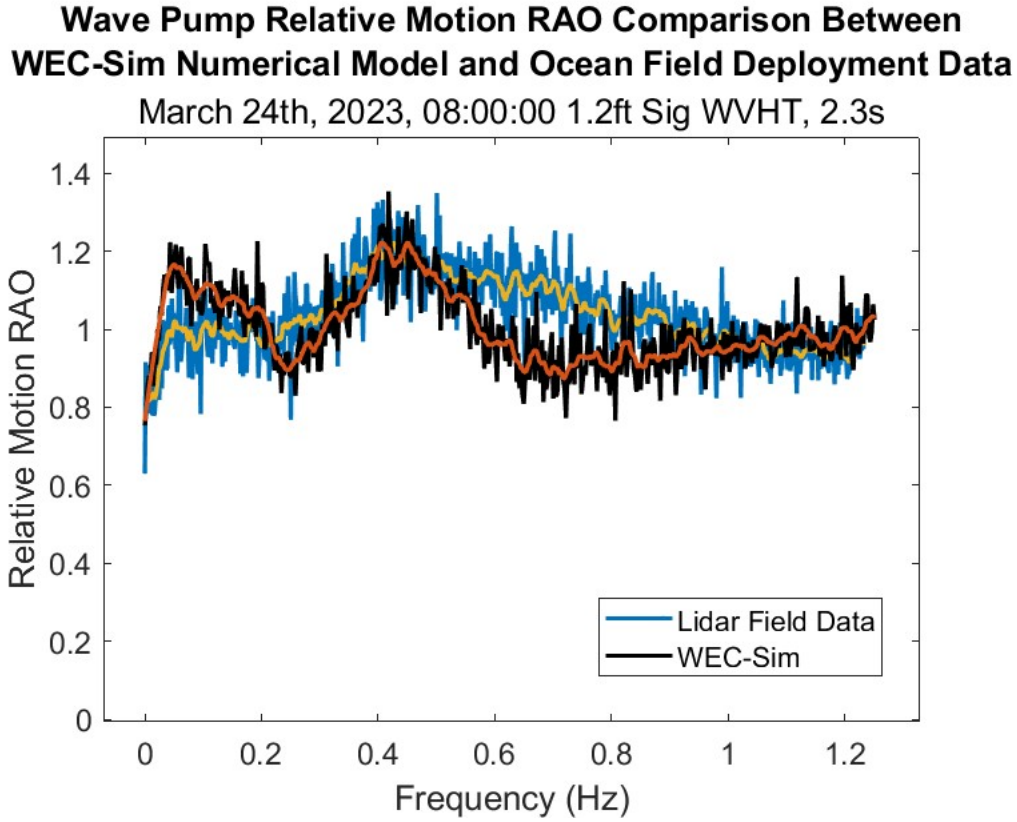

Figure 8.4: 6 DOF spar constraint example plot of WEC-Sim relative motion RAO and lidar field data relative motion RAO. Wave conditions used were Sofar spotter elevation data. Smoothed result shown for both cases for visual comparison.

For Figure 8.4 the R value was 0.378. The correlation was a moderate to weak positive correlation and was statistically significant. For all the simulations with a 6 DOF constraint, the average R value was 0.524, which was a moderate positive correlation. All the R values for the seven 6 DOF constrainted examples were statistically significant. The higher correlations for the 6 DOF constraint condition tend to be in smaller wave conditions.

Figure 8.5 is an example of relative motion RAO comparison between WEC-Sim and lidar field data for the fixed constraint. The two RAO's consistently overlap, similarly to the 6 DOF example. However, one notable exception was that at very low frequencies, the

WEC-Sim RAO has a larger magnitude than the lidar field data RAO. This was due to the fixed spar constraint, since at low frequencies the spar was no longer a wave follower, and appears as relative motion which would otherwise not be present.

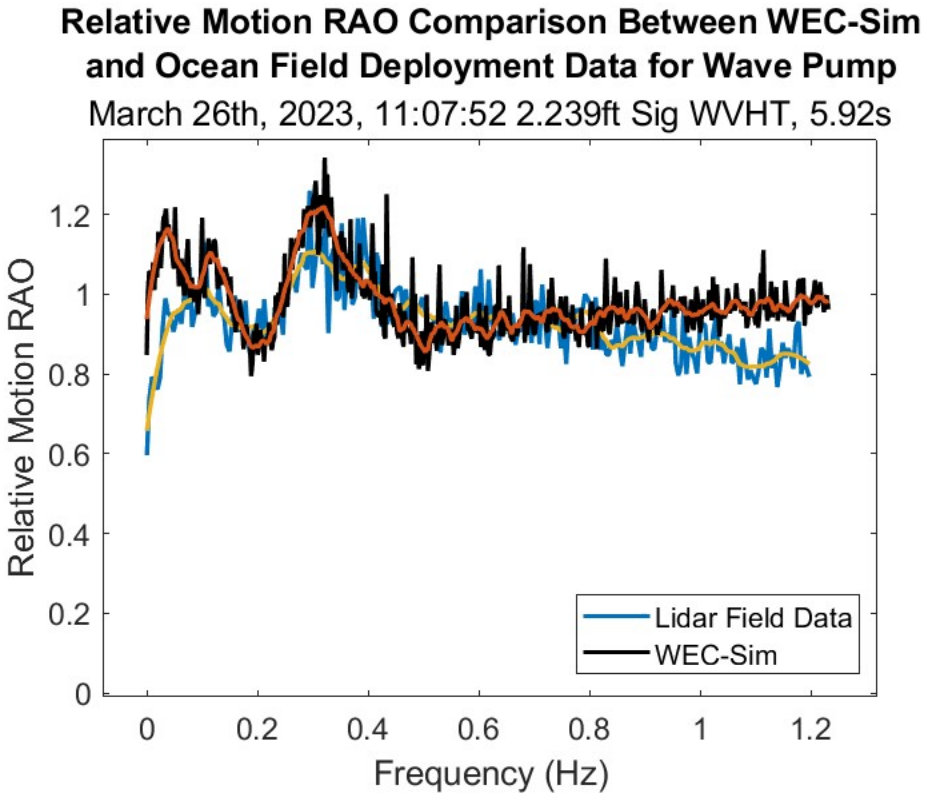

Figure 8.5: Fixed spar constraint example plot of WEC-Sim relative motion RAO and lidar field data relative motion RAO. Wave conditions used were Sofar spotter elevation data. Smoothed result shown for both cases for visual comparison.

For Figure 8.5 the correlation R value was 0.426, which was a moderate positive correlation. All the R values for the nine examples were statistically significant, with the exception of trial number 12. Excepting trial number 12, the average R value for the examples with the fixed spar constraint was 0.385. This average was less positively correlated compared to the 6 DOF constrained spar examples. It was expected that the simulation with the fixed spar constraint would less accurately represent the field data, which had a spar constrained by a mooring only. The mooring from the field deployment was specifically designed to have a reduced effect upon the heave motion of the float buoy, and allow the spar to closely mimic

a 6 DOF constraint. All the relative motion smoothed RAO correlations between WEC-Sim and field data for all simulations were included in Table 8.2.

Root-mean-square (RMS) deviation was also a measure of similarity between simulated and actual results. For the smoothed relative motion RAO's, RMS was calculated between values and was included in Table 8.2. For nearly all trials, the maximum RAO value was approximately 1.2. The values of the RMS deviation calculations were small in value ranging from 0.045 to 0.117, and comprise approximately 4% to 10% of the maximum RAO value. This indicates a high degree of similarity between the simulated and field data smoothed RAO plots amongst all the trials.

Table 8.2: WEC-Sim and Field Data Trial Smoothed Relative Motion RAO Correlations and Root-Mean-Square (RMS) Deviation

Trial #	Start Time (ET)	R-Value	P-Value	RMS Deviation
1	3/21/23 17:19	0.472	< 8.5e-4	0.064
2	3/22/23 00:59	0.555	< 8.5e-4	0.091
3	3/23/23 05:55	-0.021	< 1.25e-11	0.083
4	3/23/23 09:57	0.287	< 1.25e-11	0.072
5	3/23/23 10:57	0.315	< 1.25e-11	0.045
6	3/23/23 15:39	0.524	< 8.5e-4	0.062
7	3/24/23 08:00	0.378	< 8.5e-4	0.102
8	2/24/23 09:07	0.683	< 1.25e-11	0.078
9	3/24/23 14:09	0.378	< 8.5e-4	0.102
10	3/24/23 14:41	0.567	< 1.25e-11	0.086
11	3/25/23 20:04	0.245	< 8.5e-4	0.087
12	3/26/23 04:04	-0.062	0.154 (Not Significant)	0.079
13	3/26/23 10:45	0.443	< 1.25e-11	0.098
14 (6 DOF)	3/26/23 11:05	0.426	< 1.25e-11	0.117
14 (Fixed)	3/26/23 11:05	0.209	< 8.5e-8	0.098
15	3/26/23 12:05	0.385	< 1.25e-11	0.102

Three example plots were shown in Figure 8.6 for smoothed relative motion RAO for the 6 DOF spar constraint. These plots contain the WEC-Sim RAO result compared with the time-synchronous field data RAO result. Each of the three examples were chosen to represent three distinct wave states encountered in the field. The WEC-Sim RAO magnitudes closely match the lidar field data magnitudes throughout the frequency range. At very low

frequencies, the lidar and WEC-Sim result match very closely. In wave states with smaller wave height conditions, the largest peak occurs at a lower frequency. However, in the larger wave state condition, another peak was present for waves with a period of approximately 2 seconds. This indicates the most relative motion occurs in waves with 2 to 3 second period in the larger wave states.

In Figure 8.7, three additional example plots were shown, with a fixed spar constraint. These plots were also selected to cover a range of wave states present in the field during the deployment. The magnitudes match similarly to the previous plot throughout the frequency range, with a notable exception. At very low frequencies, the WEC-Sim reports larger RAO magnitude than the field data. This was expected since the spar was fixed in the WEC-Sim simulation, so at very low frequencies waves would report an artificially high relative motion. Otherwise, the fixed model predicts the response of the wave device very accurately, given how closely the WEC-Sim and lidar results match.

In summary, the WEC-Sim numerical model was an accurate representation of the physical wave pump device. Given nearly the same wave input data measured by the Sofar Spotter buoy, the numerical model was able to predict the average flow rate within 18.8%. Using the model in design optimization efforts should take into effect this percentage of uncertainty.

For the lidar or relative motion data, the WEC-Sim and field data reported an average similarity within 22.1% for stroke height and 15.6% for stroke period. Since processing the lidar field data may have been less accurate for some periods of time than others, it was expected that its percent difference would be slightly higher. The small percent difference for the stroke period between the field data and WEC-Sim model indicates a closer match, however this may also be attributed to the lidar data processing. The WEC-Sim model appears to be an accurate estimation of wave pump motion within a degree of uncertainty of 15 to 20%.

The RAO's for both the fixed and 6 DOF constrained spar were closely matched for

each of the sixteen trials simulated. The 6 DOF constrained spar cases were more closely matched than the fixed spar, with an average correlation r-value of 0.524, indicating an moderate positive correlation. With the fixed spar average correlatino r-value of 0.385, a moderate to weak positive correlation. Additionally the fixed spar had more dissimilarities to the field data at lower frequencies, due to the nature of the constraint.

Other factors beyond lidar processing methods that may have contributed to dissimilarities between the field data and WEC-Sim was the collection location of the Sofar Spotter data. In the field, this wave elevation data was recorded approximately three-hundred feet away from the device. However, in WEC-Sim, these wave conditions occur at the device at the time given. Meaning that the WEC-Sim simulation was not able to exactly recreate the wave conditions experienced by the wave pump device in the field.

Overall, the 6 DOF constraint was the more accurate numerical model. For future modeling efforts or device optimization, the 6 DOF modeling case can be used with a 15% to 20% accuracy for flow rate and relative motion. While the WEC-Sim model for this application is not highly accurate, it provides an adequate indicator of design performance. With the addition of an accurately modeled mooring to the WEC-Sim simulation, more accurate results would likely be obtained. Tuning the model for its characteristic values, such as discharge coefficient, could also increase the model's accuracy.

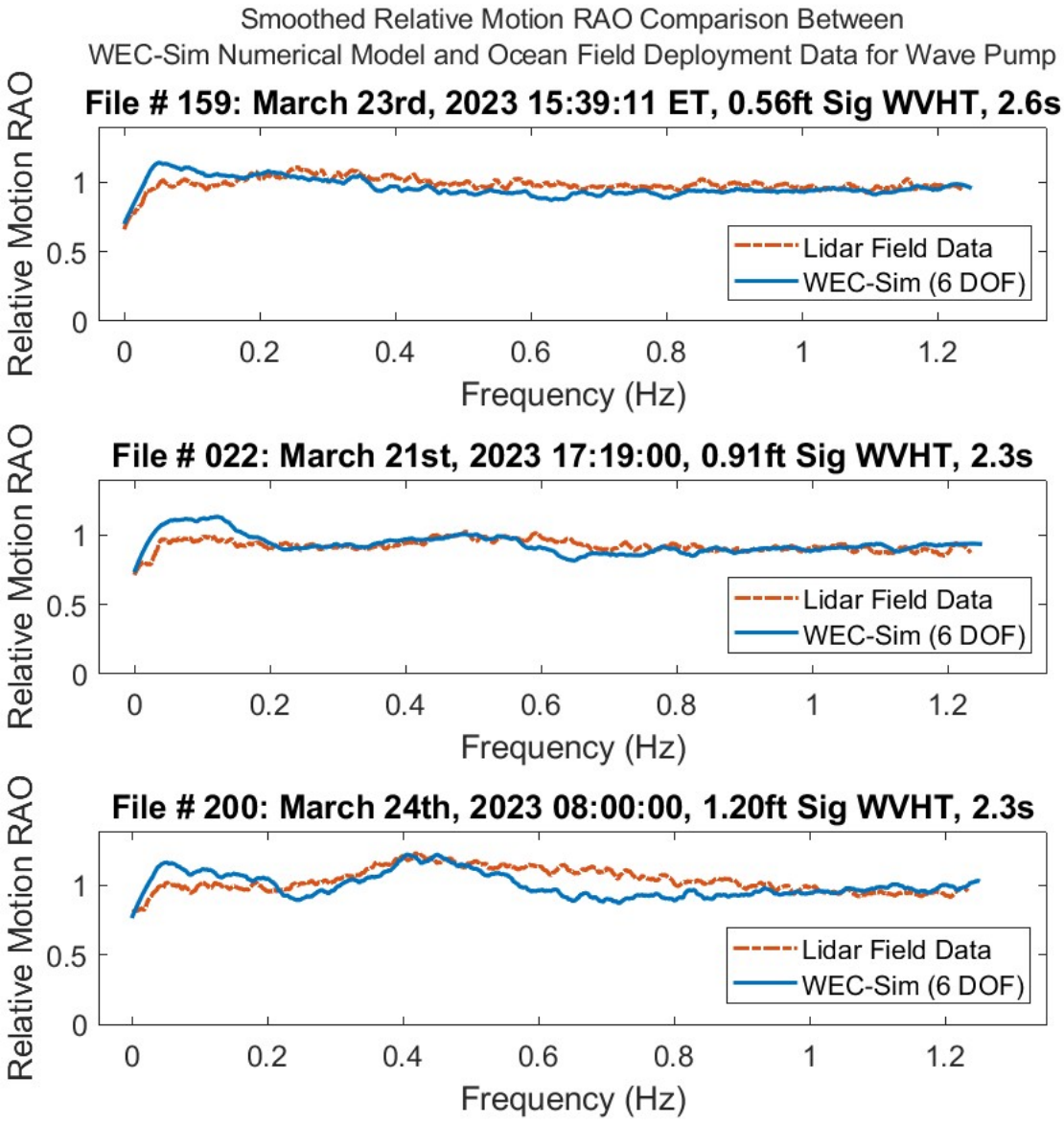

Figure 8.6: 6 DOF spar constraint three example plots of WEC-Sim relative motion RAO and lidar field data relative motion (smoothed RAO's only). Wave conditions used were Sofar spotter elevation data.

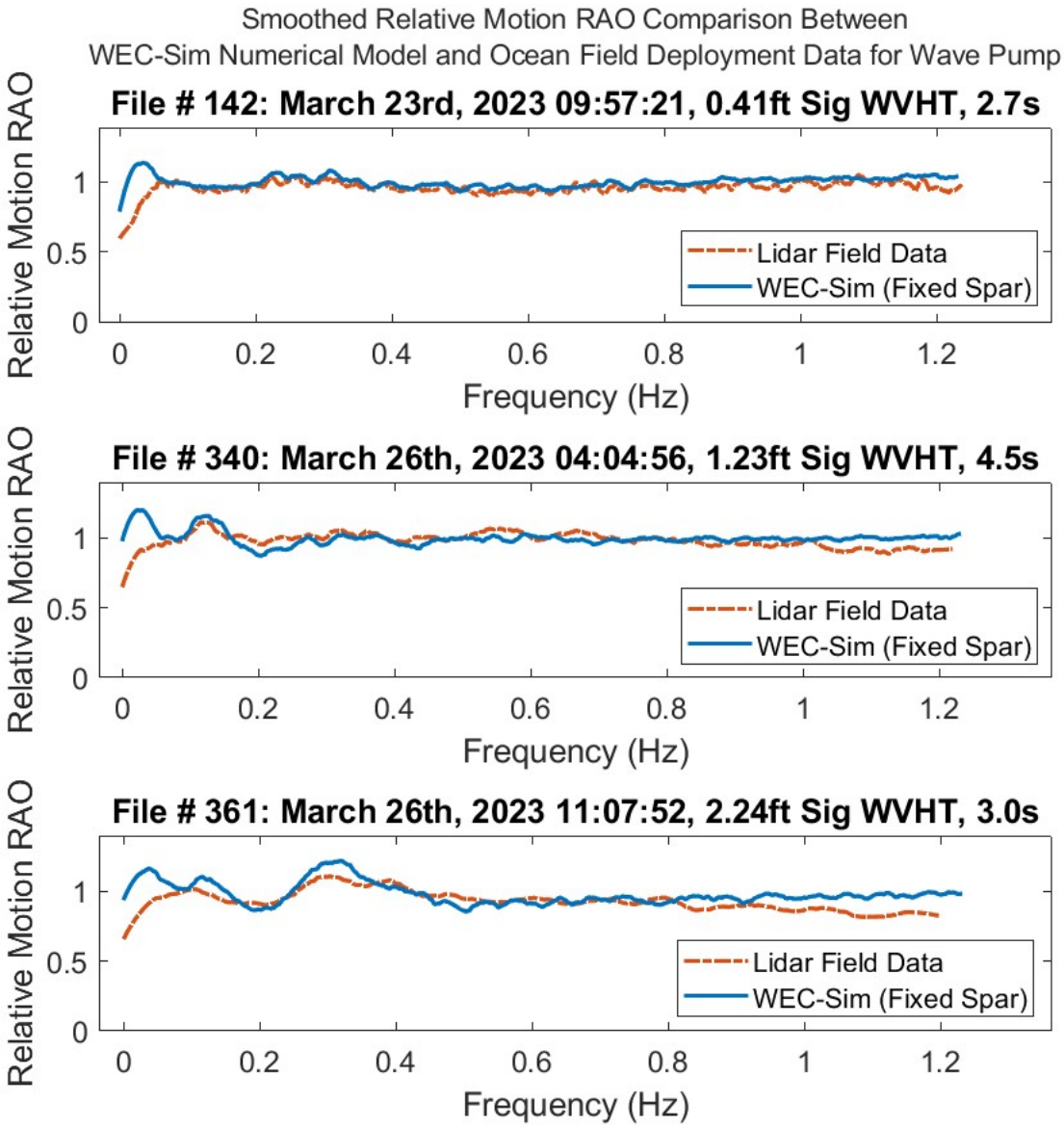

Figure 8.7: Fixed spar constraint three example plots of WEC-Sim relative motion RAO and lidar field data relative motion (smoothed RAO's only). Wave conditions used were Sofar spotter elevation data.

CHAPTER 9

Design Improvements

9.1 Motivation

Through the process of preparing the wave pump device for the ocean field deployment, and analyzing the results afterwards, many opportunities for design improvements have been discovered. These improvements comprise four major categories: performance, survivability, manufacturability, and deployment methods. These categories are interdependent upon each other, but are organized this way for clarity.

Returning to the purpose of the wave pump device, enhancing aquaculture abundance, aquaculture crops benefit from cold and nutrient rich waters. Focusing specifically on macroalgae aquaculture, both cold water and nutrient rich waters have been shown to increase productivity. Additional research between this relationship is needed to quantify exactly how much macroalgae benefits. New research in this field is in the process of being published, and the authors have generously shared some of their findings. They have found that for every 1μM increase in nitrate, kelp productivity increases by approximately 3.5 dried metric tons per hectare per year [73] in the Gulf of Maine.

Given that every aquaculture operation will differ in terms of species grown, regional location, water depth, and size of the farm, wave pump optimization will look different for every project. Regional location of each operation will lead to seasonal variations in temperature, nutrients, and wave conditions that will vary from project to project. Therefore optimizing the wave pump for a specific case study is recommended, to examine how all these factors will affect the design.

For a sugar kelp operation in the Gulf of Maine, in water depths of 100 meters, with a one to one mixing ratio of deep to surface water, it was estimated that an increase in productivity of approximately 25% can be achieved [73]. These estimations also require the use of mow-harvesting of the kelp for maximizing the theoretical yield. Additional field testing to validate these approximations are highly valued for continued work in this field.

Regardless of project specifications, the macroalgae biology clearly indicates pumping large volumes of cold water will increase productivity. This type of treatment can also extend macroalgae growing seasons. The device's performance improvement focused upon pumping substantial volumes of water from 100 meters depth or more. Applying changes in the device geometry the WEC-Sim model aids in optimizing device redesign performance. A discussion on device scaling or using multiple smaller devices was included in this section.

Improving the survivability or durability of the device required examination of the existing hydrostatics and creating a self-righting device. Additionally, making improvements to the heave plate was examined under this section. Knowledge gained from the deployment for improving manufacturability, assembly, deployment, and mooring method were also included in detail for the redesign.

9.2 Performance

9.2.1 WEC-Sim Optimization

The two main categories which will improve device performance were the ability to pump from deeper water depths and increasing the pumped volume output. To pump water at a larger volumetric flow rate for the same wave conditions experienced in the field, a larger piston size was proposed. To maximize piston area, the inner spar cylinder should be removed from the existing design. If this piece was removed, then the T-junction between the spar cylinder and the wave pump section can also be removed. This will reduce complexity of assembling and repairing the device. In this way, the main spar buoy becomes the new 'pump section,' filling with water. To further maximize piston area, a new PVC spar cylinder, size

24, was used. For flotation of the spar buoy, another PVC pipe, size 18, should be embedded inside with a closed-cell polyurethane foam sandwiched between the two pipes Figure 9.1. The length of the main spar should be twenty feet long. With these dimensions, and a foam density of two pounds per cubic foot, the spar has enough buoyancy to float at the ideal equilibrium waterline location. The stroke length of the device would be 1.14m. More details on the device's hydrostatics and self-righting capabilities were included in subsection 9.3.1.

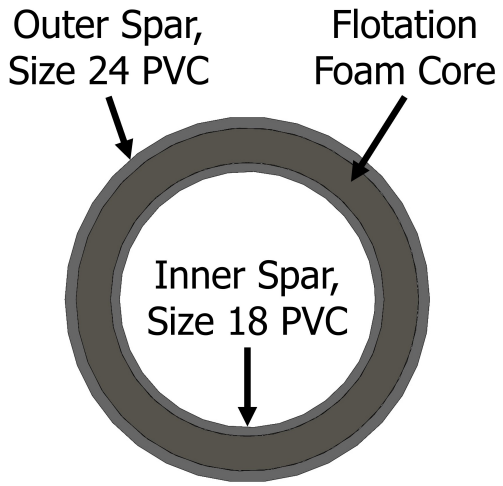

Figure 9.1: Diagram and cross-sectional view of conceptual redesign of wave pump device's spar float.

An inlet section at the bottom of the spar attaches to the existing flange, with ports for hoses. The inlet check valves were installed within the inlet section, and connect to the inlet hoses. The piston diameter increases from 0.10m to roughly 0.42m, this significantly increased the volume pump rate. Two outlet check valves would be positioned three feet underwater along the spar. Having two outlet valves allows for water to flow in two different directions amongst the aquaculture field. Additional hoses or diffusors can be attached at the outlets for maximizing mixing and distribution of the pumped water amongst the macroalgae. The outlet check valves match the size of the intake check valves. These changes allow for a shortened piston rod, which was heavy, difficult to install, and had a corrosion issue before the field deployment. The piston rod was sized such that at the float's minimum position

(resting atop the bottom bumper), the piston was still located above the check valves. A conceptual version of the system redesign is included as a cross-sectional view in Figure 9.2.

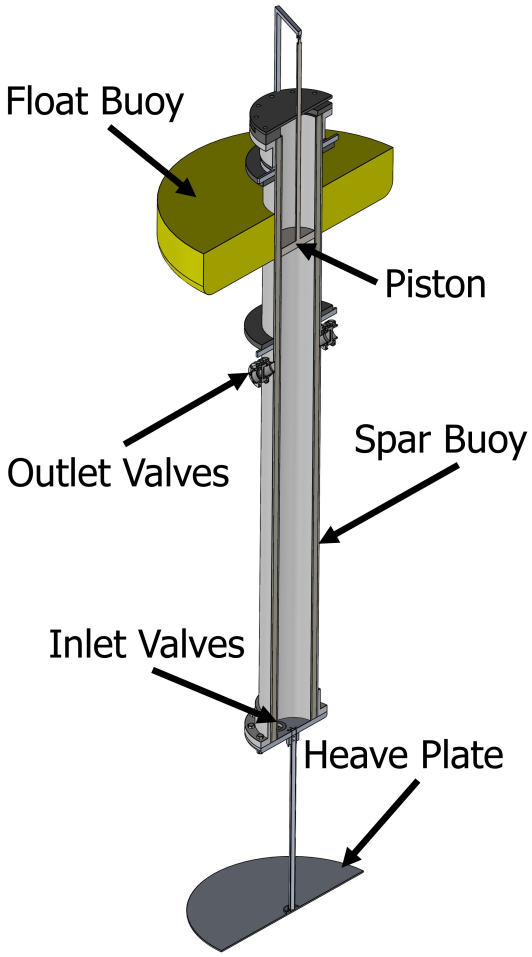

Figure 9.2: Diagram and cross-sectional view of conceptual redesign of wave pump device.

For the Gulf of Maine, 100 meters depth is sufficient in most areas to begin reaching layers in the ocean which contain both high levels of nutrients and colder waters throughout all seasons [73]. The system redesign included two intake hoses which can be up to 100 meters long. The hose used in the field deployment was semi-flexible, strong, and smooth, which makes it a good material to use in future designs. It is available to purchase OTS in 100 foot lengths, which can be coupled together to create 100 meter long hoses. The hose material is PVC, which is slightly denser than seawater, making it naturally a form of

ballast. Adding additional ballast and flotation to each intake hose allow it to be neutral in the water, while sinking the intake end. For more information see on this subsection 9.3.1.

The friction loss from hose lengths increasing from ten feet to three hundred feet decrease from 0.03m to 0.02m (approximately 33% decrease) utilizing Equation 7.7. This calculation assumes a friction coefficient of 0.03 and an average pumped water velocity of $0.93\frac{m}{s}$ within the spar. The hose diameter increased from size 2 to size 4. Given the average available power from the field deployment and the simulated average flow rate from WEC-Sim, pumping from this depth would create a device with an efficiency of 4.8%.

The wave follower buoy, or float buoy, increases in size but remains conserved in shape. To account for the increase in spar size, the overall size of the float was increased from 1.5m to a diameter of 2.4m. In other regions of the world, with different average wave heights and periods, differently sized float buoys would be ideal.

Utilizing an updated WEC-Sim model to reflect the changed design, this device produced an average flow rate of 119.6 gallons per minute (or $27.2\frac{m^3}{hour}$) in an irregular wave state of 2.21 feet significant wave height and 5.9 second wave period generated by a Pierson-Moskowitz spectrum. This was more than seven times the flow rate compared to the existing design in similar wave conditions, and an increase of efficiency from 0.5% to 4.8%. The WEC-Sim model predicted results should be expected to be accurate to a real-world design within 20% accuracy. A 55 second sample of the WEC-Sim simulation is shown in Figure 9.3. The instantaneous maximum outlet flow rates were larger than the previously modeled flow rates, reflecting the changed design. The outlet and inlet check valves maintain alternating values above zero, and the irregular wave pattern was present.

The optimal volume flow rate for a specific macroalgae aquaculture project drives the scaling or number of devices required. Without the knowledge of optimal flow rate, scaling the design or determining the number of devices required was difficult. Further discussion of this concept is in section 10.1, where additional interdisciplinary study will aid in determining optimal flow rates.

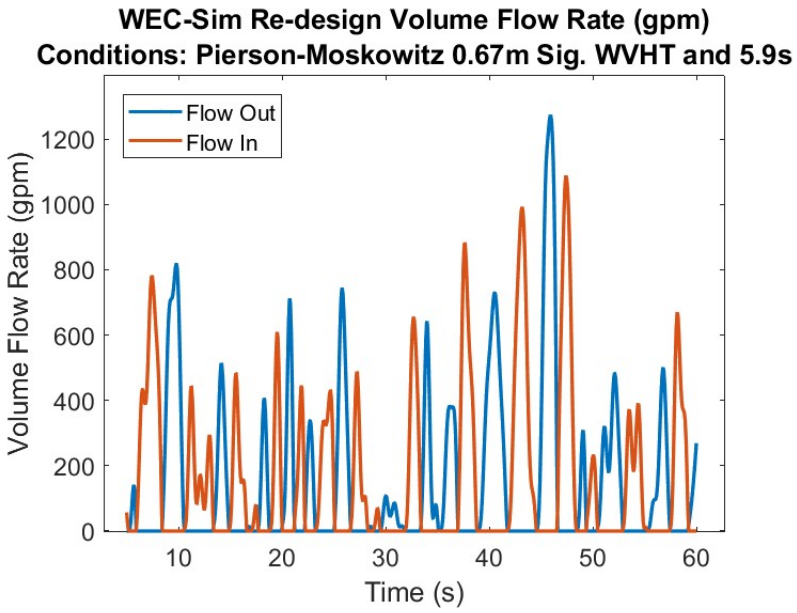

Figure 9.3: Fifty-five second sample of redesign wave pump flow rate modeled in WEC-Sim.

9.2.2 Piston Seal

Another way to increase device efficiency was to make the piston seal within the pump more effective. In the existing design, water was capable of moving past the piston seal into the chamber above. This effects device dynamics, as well as efficiency. By improving the piston seal, while not inhibiting the float's motion, efficiency of the pump would be improved. This improvement could be from using a different type of O-ring, or different combination of O-rings. The change should be tested within the laboratory to ensure that it does not extensively prohibit piston motion.

9.3 Survivability

The survivability of the device depends upon its ability to function as intended in the open ocean for long periods of time. During the field deployment, two notable occurrences indicated opportunity for device improvement. The first was the device turned over in wave conditions with significant height of three to five feet and six second period. When the device turned over, it was stable on its side, and did not right itself. The team had to take a boat

to the field site and right the device. A self-righting device would be an improvement which would aid in increasing device survivability. An analysis of the device hydrostatics, and recommendations for self-righting ballast and buoyancy were explored in subsection 9.3.1. Secondly, when the device came off its mooring, the heave plate and connection were lost. The installation method of the heave pipe was difficult, and required improvement as well. Additional details about the heave plate improvements were examined in subsection 9.3.2.

9.3.1 Hydrostatics

Following the redesign suggestions from section 9.2, the hydrostatics of the device were critically altered. Using the conceptual design, a hydrostatic analysis was performed on the device. This device has the overall spar assembly's center of gravity located 2.429m above the base of the spar. The center of gravity for the spar assembly was determined using a SolidWorks model, with accurate densities added for each component. The waterline location was 4.890m inches from the base of the spar. Assuming that the submerged volume of the heave plate and connection rod are negligible compared to the spar, the center of buoyancy was estimated as half the submerged length of the spar assembly. The center of buoyancy would be located 2.445m above the base of the spar.

The total submerged volume of the spar (without hoses) was 0.853m^3 and the mass was 875kg. A diagram of the waterline and center of gravity for the spar is shown in Figure 9.4.

This indicates a metacentric height of approximately 0.024m, which was calculated using:

$$\overline{gm} = \frac{I}{V} + \overline{bg}, \quad (9.1)$$

[61] where:

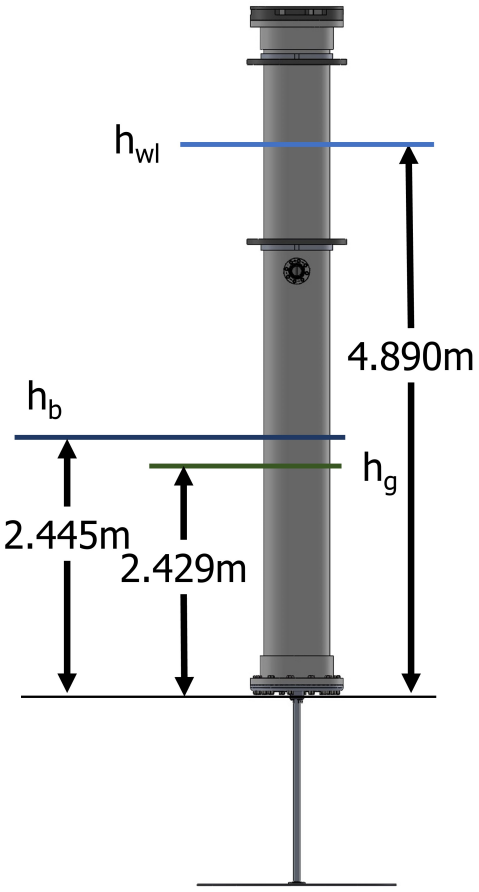

Figure 9.4: Diagram of conceptual redesign for spar float assembly of wave pump device. Waterline (h_{wl}), center of buoyancy (h_b), and center of gravity (h_g) locations shown.

$\overline{gm}$ = Metacentric height (m)

I = Second moment of area about the waterline ($0.0068m^4$)

V = Total submerged volume (0.853m^3)

$\overline{bg}$ = Distance between overall center of buoyancy and gravity (0.016m)

Since the center of gravity was beneath the center of buoyancy, the overall spar assembly was initially stable in seawater. However, the metacentric height is small, and increasing this distance would increase the overall device stability.

An additional calculation was done to ensure the device had sufficient righting moment, if tipped over at sea. A scenario was evaluated for the spar tipped over at 90°. The hoses

were not included in this analysis. A summation of the moments on the spar in this scenario was calculated to determine whether there was a righting moment. It includes a combined buoyancy force and weight force for both the float and spar buoys. The summation was taken about the combined metacenter. A free-body diagram outlining this scenario is included in Figure 9.5.

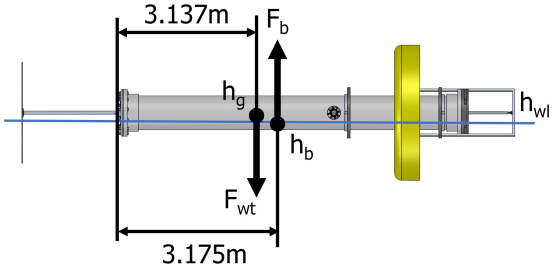

Figure 9.5: Free body diagram of redesigned wave pump tipped on side.

The centers of buoyancy for the spar on its side was calculated based on the new waterline location. The total mass of the spar and float buoys together was 1154kg. This makes the total submerged volume of both bodies $1.126m^3$. A waterline located 0.119m above the lower edge of the spar met this submerged volume requirement. It was assumed that the center of buoyancy is located in the center of the spar buoy, 3.175m from the spar's base. The center of gravity for both bodies was found using the SolidWorks model, which is located 3.137m from the spar base. The location of rotation was assumed to be located between these two points in the horizontal direction. The righting moment was given by:

$$\Sigma \overset{\curvearrowleft}{M} = \overline{wg} g M_{total} + \overline{wb} \rho g V_{total}, \quad (9.2)$$

[61] where:

ρ = Density of seawater ($1025\frac{kg}{m^3}$)

g = Gravitational constant $9.81\frac{m}{s^2}$

$\overset{\curvearrowleft}{\Sigma M}$ = Device's Righting Moment

$\overline{wg}$ = Horizontal distance between point of rotation and device's c.o.g. (0.019m)

$\overline{wb}$ = Horizontal distance between point of rotation and device's c.o.b. (0.019m)

V_{total} = Device submerged volume on its side ($1.126m^3$)

M_{total} = Mass of device (1154kg)

The overall righting moment for this scenario was 430.2N.

9.3.2 Heave Plate

The surface area of the heave plate in the redesign increased, with an outer diameter of 1.183m (compared to the original which was 0.914m). The material of the heave plate should be corrosion resistant, impervious to water, and provide some ballast. Aluminum 6061-T6 was chosen as the new heave plate material, since it matches all these requirements. Additionally the aluminum was strong to prevent flexing and bending. The weight of the new heave plate was 90kg.

A SolidWorks diagram of the heave plate and its connection points was included in Figure 9.6. The 1.83m long connection shaft for the heave plate was made of 316SS, along with the connection flange and shaft interface. An insulating gasket should be placed between the 316SS material and the aluminum material to prevent corrosion. 316SS hardware was used throughout, with sufficient sizes to prevent tearout and shear.

9.4 Manufacturability

To create a design which costs less and can be assembled in a shorter amount of time improves its manufacturability. Parts of the design which reduce complexity usually tend to aid with achieving these goals.

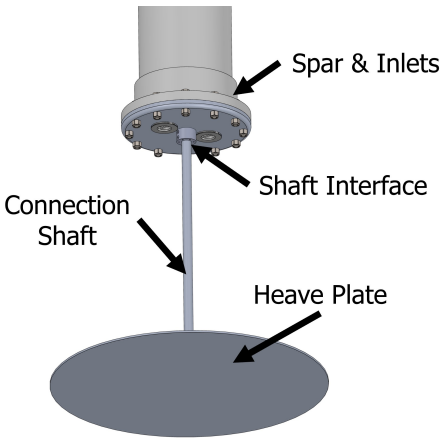

Figure 9.6: Heave plate redesign for wave pump.

The conceptual redesign proposed in this chapter eliminates many problematic aspects of the existing design. However, if the existing design was modified and used again in the future, the following items should be addressed to improve the device. The pump section of the device could be replaced by a custom piece that does not utilize glue joints, and easily makes the interface connections. The pump section's tee fitting should also be replaced so that the interface between it and the inner PVC cylinder is more reliable. When disassembling and reassembling the device, this interface was difficult to torque and seal. Another item for redesign was the heave plate's connection shaft interface. Drilling the shaft with larger holes, and selecting different hardware for attachment would increase the ease of assembly and the strength of the connection.

The top of the spar has an internal bulkhead which was currently sealed using 3M Marine 4200 Fast Cure polyurethane. This seal was imperfect, and also prevents the device from being opened and then quickly sealed again. This sealing location is shown in Figure 9.7, and was marked by the white material. This seal was critical to prevent water that passes by the piston from over-topping the inner piston cylinder, and draining back down in to the main spar cavity. This cavity was filled with air, and if it instead filled with water, the spar dynamics would be significantly altered. Additionally, the air vents at the top of the spar which were critical for piston operation, may induce water intrusion, which was another

reason why this bulkhead seal was important. An improvement to the design would swap out this type of seal for an O-ring or gasket type seal.

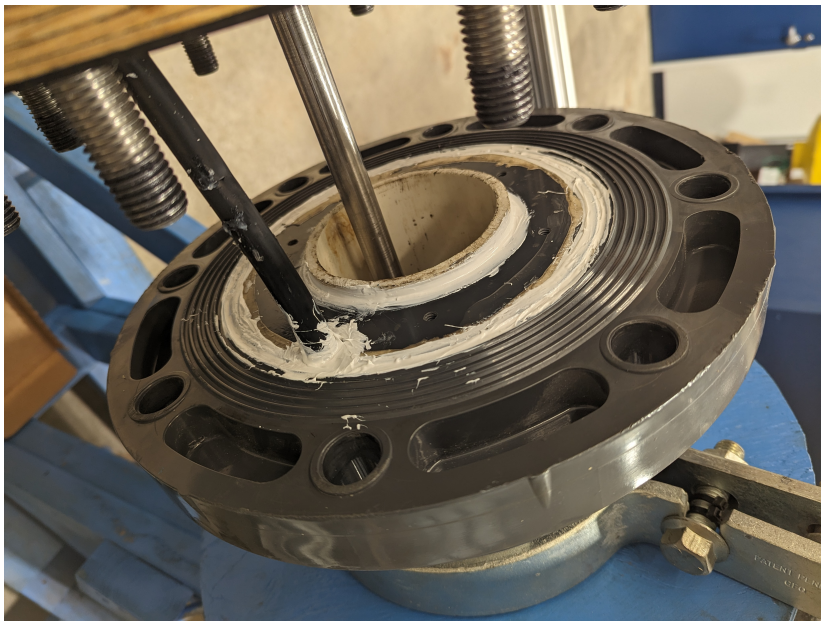

Figure 9.7: Bulkhead seal at the top of the spar.

Similarly, the Marine JBWeld epoxy used to seal the leaks in the pump (see: section 4.8) would ideally be replaced with a more permanent solution such as PVC cement, which chemically bonds the two PVC surfaces together. While these types of epoxies and polyurethanes held for a few weeks, they were not the best solution for long-term designs and should be avoided.

Wave pump devices designed for long-term use in the ocean require a different material for the heave plate. The material of the heave plate was painted plywood. Because the heave plate was not recovered from this field deployment, conclusions cannot be drawn on how well the material survived. However, from submerging it in the tank during the tank tests, the material absorbed water each time. The wood flexed and warped as well. A heave plate made of an impervious, corrosion resistant material that incorporates the ballast calculated

from subsection 9.3.1 would be a significant improvement. While it would be expensive, a 316SS heave plate would be a durable option, or aluminum 6061 with an anti-corrosion coating treatment. The best choice would depend upon how much ballast was required, and cost of manufacture. Marine HDPE or UHMWPE should not be considered, due to its buoyancy in water, which would induce a righting moment contrary to the desired effect.

Plywood was used for the air vents at the top of the spar Figure 9.8. Since this location was not submerged, this component has survived well throughout the years it has been in service. However, for long-term deployments, this material may not last as long. The stopper plates along the spar were also constructed from wood. These pieces should be made from Marine grade HDPE or UHMWPE instead. HDPE is easy to machine, and so the shape of the vents may be easily maintained. HDPE is lightweight which would reduce the weight at the top of the spar. This material is also UV resistant, has low water absorption, and is comparatively low cost to other similar plastics.

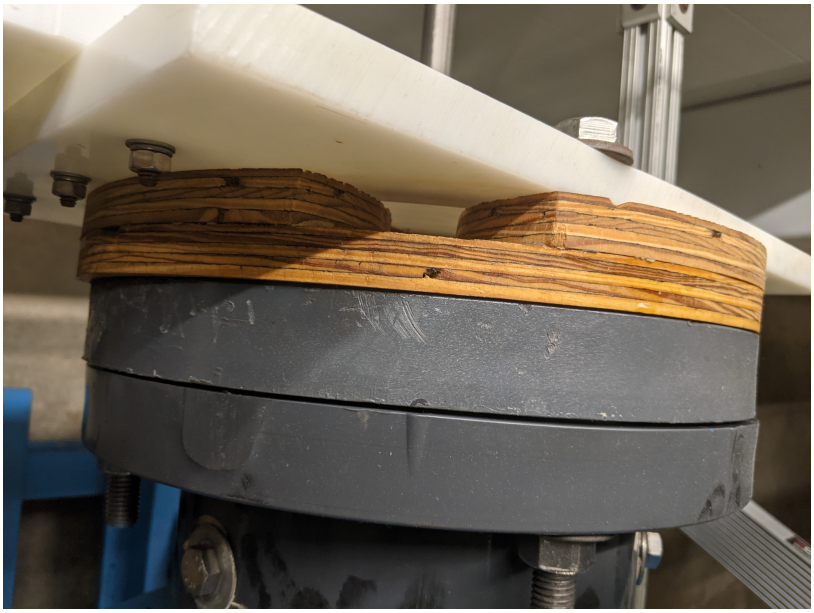

Figure 9.8: Plywood air vent component at the top of the spar buoy.

PVC was a good choice of material for the spar buoy. It is relatively strong and low cost. In colder temperatures, the impact strength of PVC does decrease, but still retains 70% to

90% of its original strength at 32°F [4]. The spar survived well during the nine days it was deployed at sea, with no significant water intrusion. During the deployment when the device came free of its mooring, one of the PVC elbows was broken off of the wave pump section. While this may seem that PVC is not a good choice of materials, as long as the wave pump remains on the mooring PVC is a durable and good choice of material. In a future design, schedule 80 PVC material may be more robust and long lasting, but generally is associated with a higher cost. Since PVC pipes are a commonly manufactured item, this is a good choice for the spar buoy's construction.

The following are recommendations for future designs and best practices for assembling devices for ocean deployment. Designs should be created such that components or smaller sub-assemblies are accessible for repair. The fewer number of tools required to make repairs is ideal. Hardware such as thumb screws or wing nuts are a good option to help reduce the number of tools required. Captive hardware is also recommended to help reduce lost hardware during deployment preparation. Components and smaller assemblies should also be designed for disassembly, making repair efforts quicker. All threaded hardware should be installed with anti-seize compound on the threads. This aids in reducing time during disassembly, and helps prevent cross-threading.

9.5 Deployment Procedure and Mooring

There were several ideas for improving the deployment procedure and wave pump mooring set up for future field trials. For the mooring hardware, 316SS shackles and lifting linkage should be invested in for future deployments. The existing hardware can withstand a period of several weeks in the ocean, but was not sufficiently corrosion-resistant for year- or season-long deployments. Additionally, screw-pin shackles seized with two strands of 14 gauge, single-stranded copper wire with insulating jacket should be chosen as the standard for all mooring connections. A 32-inch Carolina waterworks mooring float should be used when replacing the Appledore mooring posts, if the full length of chain is to be supported. At

other mooring locations, the full weight of the chain at low tide should be suitably supported by a float. A better mooring design would include a three-point setup, attached either to the float or spar buoys. The three-point mooring prevents the snapping motion observed in the on-board device video. These strong forces could degrade the mooring lines, the wave pump, or its instrumentation. By securing the device in three locations, there is less ability for wave-induced pitch and roll.

To improve the mooring process procedure there are several steps which can be taken to prevent future mooring failures. During field deployments there should be one person who is designated as the 'operations manager.' This person is the liaison between the vessel captain and the deployment team. Coordinating with the vessel captain, this operations manager leads the deployment through each evolution, research team and crew, and communication to all parties. The operations manager should additionally verify that the final equipment checks are made. A second individual should be designated 'equipment inspector.' This individual verifies with the operations manager that all final equipment checks at each stage of deployment have been made. The inspector should have a checklist with all deployment equipment review items through each stage of the deployment evolution. The inspector should sign and date each item, and could additionally take pictures, of each review step to ensure they have been completed.

CHAPTER 10

Future Work and Conclusions

10.1 Future Work

One of the main questions associated with this device relates to its efficacy. Over the course of this project, many individuals have inquired: "What is the relationship between pumping rate and quantity of additional kelp grown?" This question relates to the complex nature of an aquaculture operation, which relies upon environmental variability and kelp biological factors. In future projects, answering this question will be critical to advancing this work.

A simple control body volumetric analysis may begin this study. For example, if a four acre kelp farm ranges seven feet deep, the total volume of the farm would be 34,537 m^3. Using a one to one mixing ratio (specified in [73]), half the farm's volume should be replaced. However, this does not account for the volume of the kelp within the field. Using this approximation, a ratio greater than one to one would be analyzed. By subtracting the volume of kelp in the field, a more accurate representation of water volume requiring replacement would be achieved.

The next questions in this kind of control body analysis are: "What is the optimal rate of replacement? Should the volume of water be replaced each day? Or each hour?" This rate will be critical in determining scale and number of wave pump devices. The rate depends upon diffusion methods, sinking rate, and nutrient uptake rate of the kelp. Further research is required to answer these questions before accurate predictions can be made on what effect a wave pump device has on kelp growth.

Environmental factors, which vary widely regionally and by kelp farm, additionally add

complexity to answering device effectiveness. Some of these factors include: water depth, thermocline depth, trophic levels, seasonal variation, and currents. While these factors and questions are not an exhaustive list of required study, they propose a foundation for inquiry. A case study, which uses a specific farm size and location may aid in this research. Both theoretical and in-field studies should be conducted to completely form this case study. Interdisciplinary work amongst engineers, biologists, oceanographers, and end-users will be paramount in conducting this research.

Being able to accurately model wave pump devices is a principal part of this future research. The WEC-Sim numerical model provides an opportunity to model various sizes of wave pump devices in many wave conditions, with low-costs and time commitments. Improvements in the accuracy of the WEC-Sim numerical model will further advance the project, before committing physical devices to the field, which can be both a costly and time intensive process.

10.2 Conclusion

How much does the output yield of macroalgae aquaculture increase with the addition of an upwelling device? This question motivates the research comprising this body of work. While this question is not yet quantifiably answered, this document provides the foundation for examining a method to enhance macroalgal productivity. Wave powered upwelling devices can renewably increase both biomass and growing seasons of aquaculture crops. This boost is contributed to the cold and nutrient dense waters being moved to the surface where macroalgae typically grows. The novel wave powered water pump device design was successfully proven in a field test with high degree of reliability and durability, which are major design factors for ocean-going devices. The design's off-the-shelf components make it low-cost and therefore more accessible to end-users. Prior to ocean deployment, extensive hardware improvements, instrumentation implementation, and deployment procedures were developed for the device. From the field test results, the device was shown to pump over

sixteen gallons per minute in seas with two feet significant heights and periods of five to six seconds. As wave heights increased over the course of the field deployment, flow rates were also shown to increase. The device was also shown to be highly responsive to the wave conditions. Its efficiency was very low at 0.5% maximum; however, this was an indicator of a future team's ability to significantly increase the scale of the device for similar wave conditions. A WEC-Sim numerical model of the device was developed and validated using the field data. The WEC-Sim numerical model was shown to have approximately 20% accuracy compared to the field data. Relative motion Response Amplitude Operators (RAO) in the frequency domain agreed closely between the model and field data. This model may be used in the future to increase the scale of future device designs, and reliably predict their performance prior to manufacture and deployment, which saves valuable research resources. WEC-Sim predicted for one modified design, aimed at increasing flow rate, an average flow rate of 119.6 gallons per minute in wave conditions with significant wave height of 2.21 feet and a period of 5.9 seconds. Determining goal flow rates for devices, and number of devices for specific aquaculture operations will aid in determining the benefit of these devices. As the research continues to determine the efficacy of these devices, interdisciplinary teams can begin to understand whether macroalgaes make a suitable feedstock for biofuels.

Bibliography

[1] Lady Ada. *Adafruit Micro SD Card Breakout Board Tutorial*. 2022. URL: https://cdn-learn.adafruit.com/downloads/pdf/adafruit-micro-sd-breakout-board-card-tutorial.pdf.

[2] Lady Ada. *Adafruit Ultimate GPS*. 2022. URL: https://cdn-learn.adafruit.com/downloads/pdf/adafruit-ultimate-gps.pdf.

[3] Matthieu Ancellin and Frédéric Dias. "Capytaine: a Python-based linear potential flow solver". In: *Journal of Open Source Software* 4.36 (Apr. 2019), p. 1341. DOI: 10.21105/joss.01341. URL: https://doi.org/10.21105%5C%2Fjoss.01341.

[4] PVC Pipe Association. *Cold Weather: No Practical Effect on PVC Pipe Installation and Use*. Tech. rep. Uni-Bell, 2013.

[5] Isabel C. Azevedo et al. "Growth of Saccharina Latissima (Laminariales, Phaeophyceae) Cultivated Offshore under Exposed Conditions". In: *Phycologia* 58.5 (2019 [Online] https://doi.org/10.1080/00318884.2019.1625610), pp. 504–515.

[6] Aurélien Babarit and Gérard Delhommeau. "Theoretical and numerical aspects of the open source BEM solver NEMOH". In: *Proceedings of the 11th European Wave and Tidal Energy Conference (EWTEC2015)*. Nantes, France, 2015.

[7] Chris at BCR. *Using a Flow Sensor with Arduino*. 2021. URL: https://bc-robotics.com/tutorials/using-a-flow-sensor-with-arduino/.

[8] Alex Beale. *3 Ways to Solar Power an Arduino*. 2022. URL: https://footprinthero.com/how-to-solar-power-an-arduino.

[9] William Bemis. *Appledore Island in the Gulf of Maine*. 2015. URL: https://www.shoalsmarinelaboratory.org/sites/shoalsmarinelaboratory.org/files/media/Maps/maps_pdf_appledoreislandmap_edition4_2015.pdf.

[10] Dassault Systemes BIOVIA. *SolidWorks*. Version 2021-2022 Student Edition. San Diego: Dassault Systemes, 2021.

[11] Teis Boderskov et al. "The Effect of Light and Nutrient Availability on Growth, Nitrogen, and Pigment Contents of Saccharina Latissima (Phaeophyceae) Grown in Outdoor Tanks, under Natural Variation of Sunlight and Temperature, during Autumn and Early Winter in Denmark". In: *Journal of Applied Phycology* 28.2 (2015 [Online] https://doi.org/10.1007/s10811-015-0673-7), pp. 1153–1165.

[12] J.J. Bolton and K. Lüning. "Optimal Growth and Maximal Survival Temperatures of Atlantic Laminaria Species (Phaeophyta) in Culture". In: *Marine Biology* 66.1 (1982 [Online] https://doi.org/10.1007/bf00397259), pp. 89–94.

[13] Dakota Bouret, Brian Thorne, and Rory Walsh. *Wave Powered Water Pump*. Tech. rep. TECH 797 Ocean Projects, Final Report. University of New Hampshire, 2021.

[14] Shaun Caron, Paul Madea, and David Kurtz. *Wave Energy at Shoals Marine Lab*. Tech. rep. TECH 797 Ocean Projects, Final Report. University of New Hampshire, 2013.

[15] *Coast of Maine and New Hampshire with Isles of Shoals*. 2023. URL: https://earth.google.com/web/@43.04088244,-70.73113717,29.8531447a,55946.28958907d,35y,0.00000019h,0.91688956t,-0r.

[16] De Los Santos Ruis, I.

[17] J. Cordonnier et al. "Searev: Case Study of the Development of a Wave Energy Converter". In: *Renewable Energy* 80.N.A. (2015 [Online] https://doi.org/10.1016/j.renene.2015.01.061), pp. 40–52.

[18] *corrcoef - Correlation coefficients - Matlab*.

[19] R. Dean and R. Dalrymple. *Water Wave Mechanics for Engineers and Scientists Advanced Series on Ocean Engineering Volume 2*. World Scientific, 1991.

[20] Nathan Denoncourt and Todd Michaud. *Wave Energy Conversion Buoy*. Tech. rep. TECH 797 Ocean Projects, Final Report. University of New Hampshire, 2016.

[21] *Digiten G2" 2 inch water flow hall sensor switch flow meter 10-200L/mi*. 2023. URL: https://www.digiten.shop/products/digiten-g2-2-inch-water-flow-hall-sensor-switch-flow-meter-10-200l-min.

[22] The Economist. *Floating Offshore Farms Should Increase Production of Seaweed*. Oct. 2021 [Online] https://www.economist.com/science-and-technology/floating-offshore-farms-may-increase-production-of-seaweed/21805108.

[23] *Gulf of Maine Mean Wavelength Forecast*.

[24] Mikal Hart. *TinyGPS: A Compact Arduino GPS/NMEA Parse*. 2023. URL: http://arduiniana.org/libraries/tinygps/.

[25] I. Houghton et al. "Performance statistics of a real-time Pacific Ocean weather sensor netowrk". In: *Journal of Atmospheric and Oceanic Technology* (2021), pp. 1047–1058.

[26] *IEC TS 62600-103, Marine energy – Wave, tidal and other water current converters – Part 103: Guidelines for the early stage development of wave energy converters*. Tech. rep. International Electrotechnical Commission, 2017.

[27] Jim Irish. "Environmental Data from the NH OOA site for AquaModel". unpublished. 2010.

[28] John D. Isaacs, David Castel, and Gerald L. Wick. "Utilization of the Energy in Ocean Waves". In: *Ocean Engineering* 3.4 (1976 [Online] https://doi.org/10.1016/0029-8018(76)90022-6), pp. 175–187.

[29] Michael James. *Using serial.read() with Arduino*. Dec. 2022. URL: https://www.programmingelectronics.com/serial-read/.

[30] Lone Sunniva Jevne, Silje Forbord, and Yngvar Olsen. "The Effect of Nutrient Availability and Light Conditions on the Growth and Intracellular Nitrogen Components of Land-Based Cultivated Saccharina Latissima (Phaeophyta)". In: *Frontiers in Marine Science* N.A.7 (2020 [Online] https://doi.org/10.3389/fmars.2020.557460).

[31] J. M. Jonkman. *Dynamics Modeling and Loads Analysis of an Offshore Floating Wind Turbine*. Tech. rep. National Renewable Energy Laboratory, 2007.

[32] JangKyun Kim, Michael Stekoll, and Charles Yarish. "Opportunities, Challenges and Future Directions of Open-Water Seaweed Aquaculture in the United States". In: *Phycologia* 58.5 (2019 [Online] https://doi.org/10.1080/00318884.2019.1625611), pp. 446–461.

[33] *Kinovea*. Version v9.4.

[34] Brian Kirke. "Enhancing Fish Stocks with Wave-Powered Artificial Upwelling". In: *Ocean and Coastal Management* 46.9-10 (2003 [Online] https://doi.org/10.1016/s0964-5691(03)00067-x), pp. 901–915.

[35] *Lidar-Lite v3HP Operation Manual and Technical Specifications*. Garmin Ltd. 2018. URL: https://static.garmin.com/pumac/LIDAR-Lite_v3HP_Instructions_EN.pdf.

[36] Clark C. K. Liu et al. "Hydrodynamic Performance of Wave-Driven Artificial Upwelling Device". In: *Journal of Engineering Mechanics* 125.7 (1999 [Online] https://doi.org/10.1061/(asce)0733-9399(1999)125:7(728), pp. 728–732.

[37] Clark C.K. Liu and Chen Hsiao-hua. "Conceptual Design and Analysis of a Wave-Driven Artificial Upwelling Device". In: *OCEANS 91 Proceedings*. 1991 [Online] https://doi.org/10.1109/oceans.1991.613966.

[38] Clark C.K. Liu and Jin Qiao. "Artificial Upwelling in Regular and Random Waves". In: *Ocean Engineering* 22.4 (1995 [Online] https://doi.org/10.1016/0029-8018(94)00019-4), pp. 337–350.

[39] *Macroalgae Research Inspiring Novel Energy Resources*.

[40] MATLAB. *version 9.10.0 (R2021a)*. Natick, Massachusetts, US, 2021.

[41] Fredys Romero Menco, Ainhoa Rubio-Clemente, and Edwin Chica. "Design of a Wave Energy Converter System for the Colombian Pacific Ocean". In: *Revista Facultad De Ingeniería Universidad De Antioquia* 94.N.A. (2019 [Online] https://doi.org/10.17533/udea.redin.20190406), pp. 8–23.

[42] John J. Milledge and Patricia J. Harvey. "Potential Process 'Hurdles' in the Use of Macroalgae as Feedstock for Biofuel Production in the British Isles". In: *Journal of Chemical Technology and Biotechnology* 91.8 (2016 [Online] https://doi.org/10.1002/jctb.5003), pp. 2221–2234.

[43] Tom Miller et al. *Wave Energy Converter Research*. Tech. rep. TECH 797 Ocean Projects, Final Report. University of New Hampshire, 2009.

[44] J.R. Morison et al. "The force exerted by surface waves on piles". In: *American Institute of Mining Engineers* (1950).

[45] Ignacio A. Navarrete et al. "Effects of Depth-Cycling on Nutrient Uptake and Biomass Production in the Giant Kelp Macrocystis Pyrifera". In: *Renewable and Sustainable Energy Reviews* 141.N.A. (2021 [Online] https://doi.org/10.1016/j.rser.2021.110747), p. 110747.

[46] Sofar Ocean. *Spotter SD Parser: Open source tool for concatenating and parsing SD card data from Spotters*.

[47] Michael Philen et al. "Wave Energy Conversion Using Fluidic Flexible Matrix Composite Power Take-off Pumps". In: *Energy Conversion and Management* 171.N.A. (2018 [Online] https://doi.org/10.1016/j.enconman.2018.06.102), pp. 1773–1786.

[48] *Portsmouth Harbor - Cape Neddick to Isles of Shoals*. 2022. URL: https://www.charts.noaa.gov/PDFs/13283.pdf.

[49] Philip Pritchard and John Mitchell. *Fox and McDonald's Introduction to Fluid Mechanics*. 2015.

[50] *pwelch - Welch's power spectral density estimate - Matlab*.

[51] *rmse - Root-mean-square error between arrays - Matlab*.

[52] Robottronic. *Arduino and I2C: 7 Steps*. Oct. 2020. URL: https://www.instructables.com/Arduino-and-I2C/.

[53] F. Rongere. *Meshmagick v3.2*. Version v3.2. Oct. 2021. URL: https://lheea.github.io/meshmagick/.

[54] Michael Rosen. "SML Diver's Log". via personal email communcation.

[55] Kelley Ruehl et al. *WEC-Sim v5.0.1*. Version v5.0.1. 2022. DOI: 10.5281/zenodo.7121186. URL: https://zenodo.org/badge/latestdoi/20451353.

[56] J.M. Seitz. *LidarLite Arduino Library*. 2020. URL: https://github.com/garmin/LIDARLite_Arduino_Library/blob/master/examples/v3HP/v3HP_PWM/v3HP_PWM.ino.

[57] *smoothdata - Smooth noisy data - Matlab*.

[58] Ratanak So et al. "Development of PTO-Sim: A Power Performance Module for the Open-Source Wave Energy Converter Code WEC-Sim". In: *Proceedings of the ASME 2015 34th International Conference on Ocean, Offshore and Arctic Engineering*. 2015.

[59] *Spotter Technical Reference Manual*.

[60] M. Rob Swift. personal communication. University of New Hampshire.

[61] M. Rob Swift. University of New Hampshire.

[62] Inc. The MathWorks. *Simulink*. Natick, Massachusetts, US, 2021.

[63] The Engineering Toolbox. "Seawater Properties". 2005.

[64] Eric C. Tupper. *Introduction to Naval Architecture*. 5th. Butterworth-Heinemann, 2013.

[65] *United States Coast Guard Navigation Rules and Regulations*. 1981.

[66] N. V. Vershinskiy, B. P. Pshenichnyy, and A. V. Solov'yev. "Artificial Upwelling Using the Energy of Surface Waves". In: *Oceanology* 27.3 (1987), pp. 400–402.

[67] Y. Wei et al. "Investigating the Adaptability of the Multi-Pump Multi-Piston Power Take-off System for a Novel Wave Energy Converter". In: *Renewable Energy* 111.N.A. (2017 [Online] https://doi.org/10.1016/j.renene.2017.04.042), pp. 598–610.

[68] Angelicque White et al. "An Open Ocean Trial of Controlled Upwelling Using Wave Pump Technology". In: *Journal of Atmospheric and Oceanic Technology* 27.2 (2010 [Online] https://doi.org/10.1175/2009jtecho679.1), pp. 385–396.

[69] Gerald L. Wick and David Castel. "The Isaacs Wave-Energy Pump: Field Tests off the Coast of Kaneohe Bay, Hawaii". In: *Ocean Engineering* 5.4 (1978 [Online] https://doi.org/10.1016/0029-8018(78)90002-1), pp. 235–242.

[70] Kristen L. Wilson et al. "Effects of Increasing Water Temperatures on Survival and Growth of Ecologically and Economically Important Seaweeds in Atlantic Canada: Implications for Climate Change". In: *Marine Biology* 162.12 (2015 [Online] https://doi.org/10.1007/s00227-015-2769-7), pp. 2431–2444.

[71] Mertcan Yetkin et al. "Practical Optimal Control of a Wave-Energy Converter in Regular Wave Environments". In: *Renewable Energy* 171.N.A. (2021 [Online] https://doi.org/10.1016/j.renene.2021.02.134), pp. 1382–1394.

[72] Hristo Zhivomirov. *Sound Analysis with Matlab*. 2023.

[73] Beth Zotter et al. "Continuous, High Yield Kelp Production - System Design and Operations". 2019.

APPENDIX A

Manufacturing Drawings

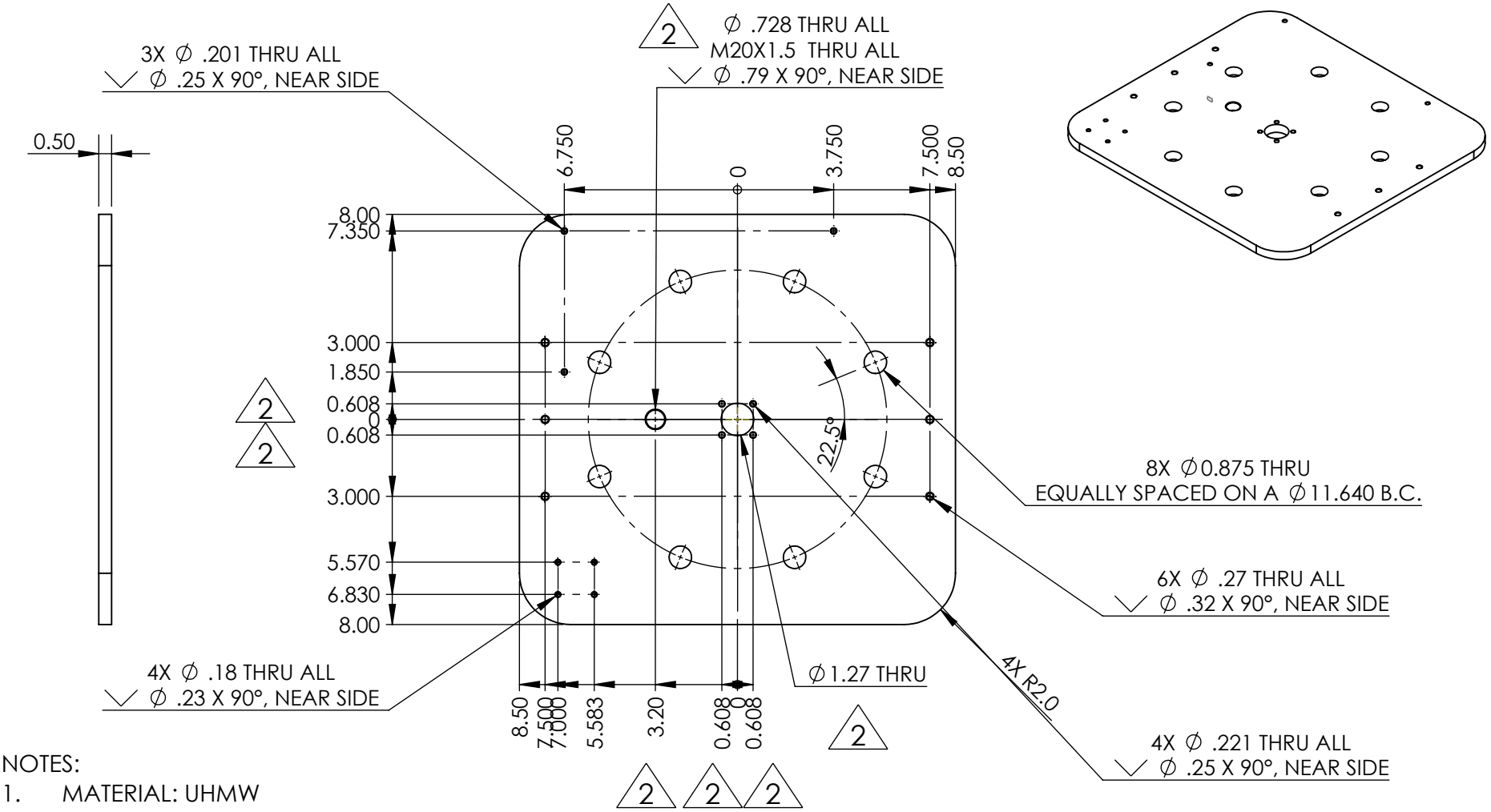

NOTES:

1. MATERIAL: UHMW PE - WHITE
2. FINISH: AS MACHINED
3. BREAK ALL SHARP EDGES & DEBURR

NEXT ASSY	USED ON	
APPLICATION		DO NOT SCALE DRAWING

UNLESS OTHERWISE SPECIFIED:

DIMENSIONS ARE IN INCHES
TOLERANCES:
FRACTIONAL ±
ANGULAR: MACH ± BEND ±
TWO PLACE DECIMAL ± 0.01
THREE PLACE DECIMAL ± 0.005

INTERPRET GEOMETRIC TOLERANCING PER:

MATERIAL:
MARINE UHMW-PE

FINISH

	NAME	DATE
DRAWN	CK	7/27/22
CHECKED		
ENG APPR.		
MFG APPR.		
Q.A.		

COMMENTS:

TITLE:

PLATE, TOP OF SPAR

SIZE	DWG. NO.	REV
A	N/A	2

SCALE: 1:2 | WEIGHT: | SHEET 1 OF 1

APPENDIX B

DAQ Module Pre-Deployment Power Test Data

Pre-Deployment – DAQ Module Power System Test

In the voltage column: B represents the flow meter Arduino circuit, G1 and G2 represent the two battery packs for the lidar Arduino circuit, and Y represents the microSD card and GPS Arduino circuit. The lowest projected run time for a DAQ module battery circuit was 7.5 days. This was concluded to be sufficient for the field test, where the batteries could be swapped in needed.

Time/Date	Voltage	Weather	Results	Notes
2/23/2023 13:50	B: 4.152 G1: 4.124 G2: 4.151 Y: 4.410	Overcast/cloudy, sunset 17:25, hum: 76%, UV 1; high: 22°F, low: 19°F	Data recorded continuously 27.5hrs; Lidar would survive ~8.5 days in these conditions, FM ~12.5 days & SD/GPS ~9 days	Conclusion of Phase 1 due to very low temps (4°F/-16°C) Lithium-ion batteries recommended min low temp operation is -4°F/20°C
2/24/2023 17:20	B: 4.072 (90.9%) G1: 4.035 (86.9%) G2: 4.033 (86.6%) Y: 4.038 (87.2%)	Sunny, sunrise 6:28, hum: 43%, UV ind 3, high: 29°F, low: 21°F		
2/27/2023 9:15	B: 4.077 G1: 4.041 G2: 4.038 Y: 4.043	Sunny, sunrise 6:23, sunset 17:30, hum: 79%, UV 1 High: 34°F, low: 19°F	Data recorded continuously for 30.5 hrs; Lidar would survive ~8.5 days in these conditions, FM would survive ~13.4 days & SD/GPS ~7.5 days	Batteries warmed and voltages increased slightly, no charging between 2/24 and 2/27
2/28/2023 15:45	B: 3.991 (82.0%) G1: 3.899 (71.9%) G2: 3.897 (71.6%) Y: 3.871 (68.2%)	Snow 02:00 to 22:00 3-5 in, sunrise 6:22, sunset 17:31, hum: 84%, UV 0, High: 35°F, low 27°F		Brushed snow off solar panels; Took DAQ module inside for 10 mins for status check @ 15:45
3/1/2023		Sunny partly cloudy, sunrise 6:20, sunset 17:33, hum: 61%, UV 2-3, high: 43°F, low: 33°F		

Time/Date	Voltage	Weather	Results	Notes
3/2/2023		Rain & cloudy, sunrise 6:19, sunset 17:34, hum 86%, UV 1, high: 41°F, low: 25°F	Data recorded continuously for 73.5 hrs - 131.5 total on this battery charge; Lidar would survive ~9 days, FM would survive ~23 days, SD/GPS ~9 days	
3/3/2023 16:13	B: 3.938 (76.2%) G1: 3.635 (38.9%) G2: 3.634 (38.8%) Y: 3.636 (39.1%)	Sunny partly cloudy, sunrise 6:17, sunset 17:35, hum 51%, UV 3, high: 45°F, low: 31°F		Pulled inside to check status and out of storm, batteries were not recharged
3/5/23 11:55	B1: 3.937 G1: 3.639 G2: 3.638 Y: 3.637	Sunny partly cloudy, sunset 17:38, hum 62%, UV 3, high 43°F, low: 30°F	Data recorded continuously for 45.5hrs - 177 hrs total on this battery charge; Lidar would survive ~ 7.5 days FM would survive ~ 29 days SD/GPS ~ 8 days	Goal is to avoid batteries operating below 20% (3.53V)
3/6/2023		Mostly sunny, sunrise 6:12, sunset 17:39, hum: 44%, UV 3, high 44°F, low: 23°F		
3/7/2023 9:25	B: 3.924 (74.6%) G1: 3.343 (2.6%) G2: 3.363 (3.8%) Y: 3.422 (8.0%)	Partly sunny, mostly cloudy, sunrise 6:10, sunset 17:40, hum 55%, UV2, high 36°F low 26°F		Voltages below 20%, charge batteries; GPS code has issue associated with +5 hour correction, switch back to UTC
3/8/23 8:45	B: 4.158 (97.5%) G1: 4.097 (93.7%) G2: 4.103 (94.2%) Y: 4.097 (93.7%)	Partly sunny, sunset 17:41, hum66%, UV2; high 46, low 32	Data recorded continuously for 48.75 hrs; Lidar would survive ~ 8 days FM would survive ~12.6 days SD/GPS would survive ~ 7.5 days	GPS code corrected & **batteries recharged** using wall power; testing another 48 hours to confirm correction
3/10/23 9:35	B: 4.008 (83.9%) G1: 3.925 (74.7%) G2: 3.925 (74.7%) Y: 3.908 (72.9%)			Confirmed GPS code correction successful, DAQ module now records in UTC time without errors - no issues for 48 hours of testing

APPENDIX C

Arduino IDE Programming Codes

Flow Meter Code

```
int flowPin = 2;    //This is the input pin on the Arduino

int flowRate;    //This is the value we intend to calculate.

volatile int count; //This integer needs to be set as volatile to ensure it updates correctly during the interrupt process.

void setup() {

  // put your setup code here, to run once:

  pinMode(flowPin, INPUT);           //Sets the pin as an input

  attachInterrupt(0, Flow, RISING);  //Configures interrupt 0 (pin 2 on the Arduino Uno) to run the function "Flow"

  Serial.begin(115200);  //Start Serial

}

void loop() {

  // put your main code here, to run repeatedly:

  count = 0;      // Reset the counter so we start counting from 0 again

  interrupts();   //Enables interrupts on the Arduino

  delay (50);   //Wait .1 second

  noInterrupts(); //Disable the interrupts on the Arduino

  //Start the math

  flowRate = (count * 2.25);        //Take counted pulses in the last second and multiply by 2.25mL

  flowRate = flowRate * 60;         //Convert seconds to minutes, giving you mL / Minute

  flowRate = flowRate / 10;       //Convert mL to Liters, giving you 10^2 Liters / Minute
**Changed for serial data transfer, what about higher flow rates??**

  Serial.println(flowRate);        //Print the variable flowRate to Serial

//  Serial.write(flowRate);

}

void Flow()

{

   count++; //Every time this function is called, increment "count" by 1

}
```

Lidar Code

```
/*----------------------------------------------------------------------------
LIDARLite Arduino Library
v3HP/v3HP_PWM
This example shows how to read distance from a LIDAR-Lite connected over the
PWM interface.
Connections:
LIDAR-Lite 5 Vdc (red) to Arduino 5v
LIDAR-Lite Ground (black) to Arduino GND
LIDAR-Lite Mode control (yellow) to Arduino digital input (pin 3)
LIDAR-Lite Mode control (yellow) to 1 kOhm resistor lead 1
1 kOhm resistor lead 2 to Arduino digital output (pin 2)
Optional Connections -
   LIDAR-Lite I2C SCL (green) to Arduino SCL
   LIDAR-Lite I2C SDA (blue) to Arduino SDA
(Capacitor recommended to mitigate inrush current when device is enabled)
680uF capacitor (+) to Arduino 5v
680uF capacitor (-) to Arduino GND
See the Operation Manual for wiring diagrams and more information:
http://static.garmin.com/pumac/LIDAR-Lite_v3HP_Instructions_EN.pdf
----------------------------------------------------------------------------*/
#include <stdint.h>
#include <Wire.h>
#include "LIDARLite_v3HP.h"
#include <SoftwareSerial.h> // added 10/10/22
SoftwareSerial link(6, 7); // RX, TX added 10/10/22
LIDARLite_v3HP myLidarLite;
#define MonitorPin    3
```

```
#define TriggerPin    2
uint32_t distance;
uint32_t startTime;
uint32_t endTime;
bool     newDistance = false;
bool     measuring   = false;
// ----------------------------------------
// Add in the #define below to illustrate
// optional use of I2C during PWM mode
// ----------------------------------------
//#define USE_I2C
void setup()
{
   Wire.begin();
   Serial.begin(115200); // Start serial communications
   #ifdef USE_I2C
      // Initialize Arduino I2C (for communication to LidarLite)
      Wire.begin();
      Wire.setClock(400000UL); // Set I2C frequency to 400kHz (for Arduino Due)
   #endif
   pinMode(MonitorPin, INPUT);
   pinMode(TriggerPin, OUTPUT);
   digitalWrite(TriggerPin, LOW); // Set trigger LOW for continuous read
   startTime = micros();
   endTime   = startTime;
}
void loop()
{
```

```
{
 if (digitalRead(MonitorPin))
 {
    if (measuring == false)
    {
       startTime   = micros();
       measuring   = true;
    }
 }
 else
 {
    if (measuring == true)
    {
       endTime     = micros();
       measuring   = false;
       newDistance = true;
    }
 }
 // If we get a new reading, print it
 if (newDistance == true)
 {
    distance = (endTime - startTime) / 10; // 10usec = 1 cm of distance
    Serial.println(distance); // Print measured distance
    Wire.beginTransmission(9);//9 here is the address of the slave board
    Wire.write(distance);//Transfers the value of potentiometer to the slave board
    Wire.endTransmission();
    #ifdef USE_I2C
       uint8_t  signalStrength = 0;
```

```
        myLidarLite.read(0x0e, &signalStrength, 1);
        Serial.print("SS = ");
        Serial.println(signalStrength, DEC);
        Serial.println();
      #endif
      newDistance = false;
    }
  }
}
```

GPS & MicroSD Storage Code

```
#include <Wire.h>
#include <SoftwareSerial.h>
#include <SPI.h>
#include <SD.h> // Needed for the SD card
#include <TinyGPS.h>
#include <TimeLib.h>
TinyGPS gps;
SoftwareSerial ss(8, 7);
// Creating Variables. EndTime is giving and initial value of 0
// The rest do not need initial values. Still need?
unsigned long TimeData;
unsigned long EndTime = 0;
//unsigned long rTime;
//unsigned long Distance;
//unsigned long distance;
//// SD card
int CS_pin = 10;  // SD card pin. This pin that will be used to write to the SD card
////int pow_pin = 8;  // SD card power pin. Sends Power to the SD Shield... no?
```

```
//Data Transfer Code Between Arduinos, wired with a common ground, A4 to A4, A5 to A5

//Trigger issue with going from PWM data to I2C data, clock on A5 triggers data transmission, at full ceiling height, receiver is reading inaccurate data --> ok for our purpose?

int distance;

const unsigned int MAX_MESSAGE_LENGTH = 12; //maximum length of serial communication, adjustable

const int offset = -5;  // Eastern Standard Time (USA) takes effect after November 6th

  void setup()

  {

    Serial.begin(115200);    //setup serial monitor

    ss.begin(9600); //changed from 4800

    pinMode(CS_pin, OUTPUT);

    digitalWrite(CS_pin, HIGH);

   if(!SD.begin(CS_pin)){

    Serial.println("card failed");

   }

   else{

    Serial.println("Card Ready");

    Wire.begin(9);//9 here is the address(Mentioned even in the master board code)

    Wire.onReceive(receiveEvent);

   }//why is this working inside the else statement?

  }

void receiveEvent(int bytes) {

  distance = Wire.read();//Receive value from master board

}

void loop() {

//  /* This for loop is what sets up the data csv files. The file names are incremented by 1 for each iteration of the void loop code.
```

```
//   * Currently is set up to make 1000 files. Increase as needed
  for(int i =1; i<=1000; i++){
    String filename = "Data_";
    filename.concat(i);
    filename.concat(".csv");
    File dataFile = SD.open(filename, FILE_WRITE);
    if (dataFile){
      /* This is where the columns in the file are set.There are three commas because
       *  there are three columns of data being
       * saved. If there were four columns of data then you would put four commas.
       * the Stringer header labels the data columns
       */
      dataFile.println(",,,,,,,");
      String header = "GPS Date (ddmmyy), Hour, Minute, Second, Data Time (ms), Distance (cm), Flow Rate (10^2 lpm)"; //Will change these to Year Month Day Hour Minute Second (Time), Distance (cm), Flow Rate (gpm)
      dataFile.println(header);
      dataFile.close();
      }
      /* This while loop holds all of the code that carries out the actual
       *  measurements. The while loop is set up run until the time
       * reaches 900000 (15 mins).This means you will have 15 minutes worth of data
       * in data_1.csv that was set up above.
       */
    while (TimeData<=1200000+EndTime){ // (1200000) 20 minutes alter time as necessary, this is record time **Changed "900000" to "90000" on 10/10/22 for test run in lab
      TimeData = millis();     // Time since loop while loop has started
       while (Serial.available()>0)
    {
```

```
    //Create a place to hold incoming message
    static char FlowRate[MAX_MESSAGE_LENGTH];
    static unsigned int message_pos = 0;
    //Read the next available byte in the serial receive buffer
    char inByte = Serial.read();
    //Message coming in (check not terminating character) and guard for over message size
    if ( inByte != '\n' && (message_pos < MAX_MESSAGE_LENGTH - 1) )
    {
     //Add incoming byte to flow rate data
     FlowRate[message_pos] = inByte;
     message_pos++;
    }
    //Full data entry sent...
    else
    {
     //Add null character to string
     FlowRate[message_pos] = '\0';
     int FlowRateN = atoi(FlowRate);
while (ss.available())
{
 char c = ss.read();
 (gps.encode(c));
  }
     unsigned long age, date, time;
     int Year;
     byte Month, Day, Hour, Minute, Second;
     gps.get_datetime(&date, &time);
    gps.crack_datetime(&Year, &Month, &Day, &Hour, &Minute, &Second, NULL, &age);
```

```
      byte Hour_C = Hour + offset;
      //setTime(Hour, Minute, Second, Day, Month, Year);
      //adjustTime(offset * SECS_PER_HOUR);
      String datastring =
String(date)+","+String(Hour_C)+","+String(Minute)+","+String(Second)+","+String(TimeData
)+","+String(distance)+","+String(FlowRateN); //replaced "Voltage" with "data" and started
comma after "(data);" 10/10/22
      //SD card
      String filename = "Data_";
      filename.concat(i);
      filename.concat(".csv");
      File dataFile =SD.open(filename, FILE_WRITE);
      if(dataFile){
        dataFile.println(datastring);
        dataFile.close();
        message_pos = 0;
        }
      }
    }
     // FlowRate = Serial.read(); // moving flow rate inside while loop got rid of bogus -1 values,
values are still bogus tho...

    // rTime = millis()-Time;
     EndTime = millis();
     delay(100);
    }
  }
//      delay(2400000);  // Is the time between data files. (2400000) 40 minutes
}
```

APPENDIX D

DAQ Module Power During Ocean Field Test

Field Deployment – DAQ module Battery Data

Date	3/21/23	3/23/23			3/23/23	3/28/23		
Operation Note	Begin: Pack 1	End: Pack 1	Actual Runtime Duration: 47.5 hours		Begin: Pack 2	End: Pack 2	Actual Runtime Duration: 122.3 hours	
Circuit	Voltage	Voltage	ΔV	Projected Runtime	Voltage	Voltage	ΔV	Projected Runtime
Lidar (2X)	4.112	3.997	0.115	71 days	4.112	3.747	0.365	57 days
Flow Meter	4.112	4.049	0.063	130 days	4.112	3.996	0.116	180 days
GPS/Data	4.112	3.962	0.150	54 days	4.112	3.889	0.223	94 days

The field deployment projected runtimes are longer than the outdoor bench test in late February and early March, likely due to the differing weather conditions during each test duration. On longer, warmer, sunnier days, the power system is going to last longer due to solar panel and Lithium battery functionality. The minimum run time in late March can be assumed to be at least 50 days for this DAQ module set up. Slight differences in pack manufacturing could also contribute to some of the differences in runtime.

APPENDIX E

Log of Known Boat Trips During Field Test

Known boat trips to SML mooring field for cross-checking in hydrophone data.

Date	Approximate Time (ET)	Vessel Interaction
3/22/23	10:00	JB Heiser drives thru mooring field and ties up at high tide dock for a few hours, then leaves
3/23/23	08:50-10:20	Galen J vessel drives through mooring field
3/28/23	10:40-12:40	Galen J vessel drives through mooring field
3/31/23	08:00-09:00	Galen J vessel retrieves wave pump, ties up at high tide dock
4/3/23	08:00-09:00	R/V Gulf Challenger retrieves spotter buoy, moorings, hydrophones

APPENDIX F

Video Observations from Wave Pump Device During Field Deployment

Camera 1 Device Video Data Observations

Date/Time	Observation
3/21/23 13:30 to 21:36	No animal sightings, mooring lines cause rotation in large waves, light snow/precipitation begins around 20:30
3/22/23 11:51 to 20:00	No animal sightings
3/23/23 10:50 to 12:11	Galen J visit at 11:09, black back gull sitting on float at 12:11
3/24/23 02:27 to	09:18 to 10:42 various gull interactions: juvenile black back gull flies by at 9:18, 10:40 black back gull lands in water near float, 10:42 juvenile herring gull lands on float, 10:44 two herring gull juveniles land in water near float
3/25/23 16:53 (one video)	Snowing, calm conditions
3/26/23 09:49 to 10:48	Water on lens creates yellow spot
3/27/23 15:11 to 18:54	Buoy on its side, gull calls heard in audio
3/28/23 06:24 to 20:58	Buoy on its side, light precipitation, buoy is righted for evening videos
3/29/23 11:30 to 16:11	Juvenile gull(s) appear in videos between 11:30 and 11:40, gulls exhibit foraging and roosting behaviors interacting with the wave pump and mooring. Creaking noise heard from wave pump.

Camera 2 Device Video Data Observations

Date/Time	Observation
3/21/23 ~13:00 to 20:35	Light precipitation ~20:00, shore lights visible in evening
3/22/23 00:12 to 20:40	Calm conditions
3/23/23 08:18 to 23:58	Galen J trip from 09:00 to 10:15
3/24/23 01:00 to 16:35	Calm conditions
3/25/23 14:57 (one video)	Snowing, calm conditions
3/26/23 08:20 to 15:13	In the morning, building sea state visible, DAQ module is sometimes visible indicating occasional misalignment between spar and float; video taken <10 mins before wave pump overturns
3/27/23 09:25 to 16:00	Wave pump on its side
3/28/23 02:26; 14:17 to 20:44	Swapped camera microSD cards during Galen J trip; wave pump is upright in evening videos
3/29/23 13:15 to 20:09	Calm conditions, possible rope debris (not from wave pump) at ~20:00

Additional screenshots of gull interactions from the video cameras are included here:

APPENDIX G

Specifications for Head Loss Calculation

Wave Pump Piston Pump Head Loss Calculation Tracker		Note: All lengths are in m				
Reference Material: Fox & McDonald Introduction to Fluid Mechanics		**Need to use Colebrook equation to get accurate friction factor**				
Major Losses						
Description	**Components**	**Properties**				
Inlet/Outlet Hose	52375K41	Area = 0.002027, Length = 4.572				
Piston	N/A	Area = 0.008107, Length = 1.0				
Minor Losses						
Description	**Components**	**Properties**	**Part**	**Part No.**	**Area**	
Inlet to inlet hose	52375K41	K = 0.5	hose	52375K41	2.02683E-03	
Reduction from inlet hose to first fitting	52375K41 to 48315K96	AR = 0.686, K=0.17	fitting	48315K96	1.38960E-03	
Enlargement from first fitting to adapter	48315K96 to 4596K448	AR = 0.729, K = 0.15	adapter	4596K448	1.90501E-03	
Check valve	7746K47	K = 0.61				
90 degree elbow	N/A	K = 1.5	**Component Path**		**Area Ratio (AR)**	
Tee Fitting	N/A	K = 2.0	52375K41 to 48315K96		0.686	contraction
90deg Elbow	N/A	K = 1.5	48315K96 to 4596K448		0.729	expansion
Check Valve	7746K47	K = 0.61	4596K448 to 48315K96		0.729	contraction
Reduction from adapter to second fitting	4596K448 to 48315K96	AR = 0.729 K = 0.15	48315K96 to 52375K41		0.686	expansion
Enlargement from 2nd fitting to 2nd hose	48315K96 to 52375K41	AR = 0.686 K = 0.17	52375K41 to 48315K96		0.686	contraction
Reduction from 2nd hose to FM fitting	52375K41 to 48315K96	AR = 0.686 K = 0.17				
	Sum all K's	7.53				

APPENDIX H

Average Values from WEC-Sim Simulated Data and Field Data for Validation

	Time: 3/24/23 08:00:42, DAQ Trial # 200 (208)				Time: 3/21/23 17:19:00, DAQ Trial # 022			
Property ↓ Method →	**WEC-Sim**	**LIDAR/FM**	**Spotter**	**% Difference**	**WEC-Sim**	**LIDAR/FM**	**Spotter**	**% Difference**
Avg. Flow Rate (gpm)	9.613	11.7	N/A	19.58	7.314	9.01	N/A	20.78
Avg. Stroke Height (ft)	0.653	0.837	N/A	24.70	0.518	0.644	N/A	21.69
Avg. Stroke period (s)	2.32	1.93	N/A	18.35	2.39	2.02	N/A	16.78
Tot. Vol Pumped (gal)	108	234	N/A	13.59	59.7	180.09	N/A	14.34
Delta Inlet-Outlet (gal)	0.146	N/A	N/A	N/A	0.0202	N/A	N/A	N/A
Sig. WVHT (ft)	N/A	N/A	1.24	N/A	N/A	N/A	0.91	N/A
Wave Period (s)	N/A	N/A	2.4	N/A	N/A	N/A	2.29	N/A
Note:	WEC-Sim worked for first 675s, 6 DOF				WEC-Sim worked for first 490s, 6 DOF			
	Time: 3/22/23 00:59:45, DAQ Trial # 045				**Time: 3/23/23 15:39:11, DAQ Trial # 159**			
Property ↓ Method →	**WEC-Sim**	**LIDAR/FM**	**Spotter**	**% Difference**	**WEC-Sim**	**LIDAR/FM**	**Spotter**	**% Difference**
Avg. Flow Rate (gpm)	4.589	3.969	N/A	14.49	4.4999	3.135	N/A	35.75
Avg. Stroke Height (ft)	0.343	0.615	N/A	56.78	0.375	0.322	N/A	15.21
Avg. Stroke period (s)	2.68	2.13	N/A	22.87	2.97	3.45	N/A	14.95
Tot. Vol Pumped (gal)	91.7	79.3	N/A	14.50	40.9	62.58	N/A	22.64
Delta Inlet-Outlet (gal)	0.043	N/A	N/A	N/A	0.043	N/A	N/A	N/A
Sig. WVHT (ft)	N/A	N/A	0.56	N/A	N/A	N/A	0.56	N/A
Wave Period (s)	N/A	N/A	2.36	N/A	N/A	N/A	2.59	N/A
Note:	WEC-Sim completed simulation without errors, 6 DOF				WEC-Sim worked for first 545s, 6 DOF			
	Time: 3/24/23 14:41:09, DAQ Trial # 222				**Time: 3/25/23 20:04:09, DAQ Trial # 316**			
Property ↓ Method →	**WEC-Sim**	**LIDAR/FM**	**Spotter**	**% Difference**	**WEC-Sim**	**LIDAR/FM**	**Spotter**	**% Difference**
Avg. Flow Rate (gpm)	11.149	12.476	N/A	11.23	4.052	3.817	N/A	5.97
Avg. Stroke Height (ft)	0.886	1.005	N/A	12.59	0.412	0.329	N/A	22.40
Avg. Stroke period (s)	2.68	2.01	N/A	28.57	3.63	3.77	N/A	3.78
Tot. Vol Pumped (gal)	57.4	249.1	N/A	7.54	15.9	76.2	N/A	4.18
Delta Inlet-Outlet (gal)	0.066	N/A	N/A	N/A	0.236	N/A	N/A	N/A
Sig. WVHT (ft)	N/A	N/A	1.202	N/A	N/A	N/A	0.68	N/A
Wave Period (s)	N/A	N/A	2.44	N/A	N/A	N/A	3.71	N/A
Note:	WEC-Sim worked for first 309s, 6 DOF				WEC-Sim worked for first 235s, 6 DOF			

	Time: 3/26/23 11:05:34, DAQ Trial # 361				Time: 3/23/23 10:57:46, DAQ Trial # 145 (137)			
Property ↓ Method →	**WEC-Sim**	**LIDAR/FM**	**Spotter**	**% Difference**	**WEC-Sim**	**LIDAR/FM**	**Spotter**	**% Difference**
Avg. Flow Rate (gpm)	13.631	16.2999	N/A	17.83	3.285	2.404	N/A	30.97205133
Avg. Stroke Height (ft)	1.341	1.044	N/A	24.91	0.328	0.35	N/A	6.489675516
Avg. Stroke period (s)	3.13	2.82	N/A	10.42	3.747	3.483	N/A	7.302904564
Tot. Vol Pumped (gal)	19.3	325.5	N/A	12.18	65.1	48	N/A	30.23872679
Delta Inlet-Outlet (gal)	0.194	N/A	N/A	N/A	0.035	N/A	N/A	N/A
Sig. WVHT (ft)	N/A	N/A	2.24	N/A	N/A	N/A	0.41	N/A
Wave Period (s)	N/A	N/A	3	N/A	N/A	N/A	3.18	N/A
Note:	WEC-Sim worked for first 85s, 6 DOF				WEC-Sim appears to run full sim, Fixed			
	Time: 3/23/23 09:57:21, DAQ Trial # 142 (134)				**Time: 3/23/23 05:55:40, DAQ Trial # 132 (122)**			
Property ↓ Method →	**WEC-Sim**	**LIDAR/FM**	**Spotter**	**% Difference**	**WEC-Sim**	**LIDAR/FM**	**Spotter**	**% Difference**
Avg. Flow Rate (gpm)	3.257	3.307	N/A	1.523461304	3.043	1.571	N/A	63.80580841
Avg. Stroke Height (ft)	0.337	0.518	N/A	42.33918129	0.32	0.329	N/A	2.773497689
Avg. Stroke period (s)	3.953	2.78	N/A	34.84330907	3.93	3.93	N/A	0
Tot. Vol Pumped (gal)	64.589	66.1	N/A	2.312359877	60.348	31.329	N/A	63.30704539
Delta Inlet-Outlet (gal)	0.2	N/A	N/A	N/A	0.055	N/A	N/A	N/A
Sig. WVHT (ft)	N/A	N/A	0.41	N/A	N/A	N/A	0.41	N/A
Wave Period (s)	N/A	N/A	2.65	N/A	N/A	N/A	2.84	N/A
Note:	WEC-Sim appears to run full sim, Fixed				WEC-Sim appears to run full sim, Fixed			
	Time: 3/24/23 14:09:06, DAQ Trial # 226 (218)				**Time: 3/26/23 04:04:56, DAQ Trial # 340 (331)**			
Property ↓ Method →	**WEC-Sim**	**LIDAR/FM**	**Spotter**	**% Difference**	**WEC-Sim**	**LIDAR/FM**	**Spotter**	**% Difference**
Avg. Flow Rate (gpm)	10.09	12.19	N/A	18.85098743	7.956	6.473	N/A	20.55582507
Avg. Stroke Height (ft)	0.727	0.878	N/A	18.81619938	0.905	0.493	N/A	58.94134478
Avg. Stroke period (s)	2.455	2.05	N/A	17.9800222	3.954	3.036	N/A	26.26609442
Tot. Vol Pumped (gal)	200.1	243.6	N/A	19.60784314	157.6	129.4	N/A	19.65156794
Delta Inlet-Outlet (gal)	0.172	N/A	N/A	N/A	0.193	N/A	N/A	N/A
Sig. WVHT (ft)	N/A	N/A	1.23	N/A	N/A	N/A	1.23	N/A
Wave Period (s)	N/A	N/A	2.52	N/A	N/A	N/A	4.47	N/A
Note:	WEC-Sim appears to run full sim, Fixed				WEC-Sim appears to run full sim, Fixed			

	Time: 3/24/23 09:07:00, DAQ Trial # 211 (203)				Time: 3/26/23 10:45:32, DAQ Trial # 360 (351)			
Property ↓ Method →	**WEC-Sim**	**LIDAR/FM**	**Spotter**	**% Difference**	**WEC-Sim**	**LIDAR/FM**	**Spotter**	**% Difference**
Avg. Flow Rate (gpm)	10.081	10.998	N/A	8.700602495	15.095	16.157	N/A	6.796365033
Avg. Stroke Height (ft)	0.721	0.746	N/A	3.408316292	1.242	1.11	N/A	11.2244898
Avg. Stroke period (s)	2.431	2.026	N/A	18.17365941	2.789	2.75	N/A	1.408196425
Tot. Vol Pumped (gal)	199.9	219.8	N/A	9.482964022	299.4	322.9	N/A	7.55262735
Delta Inlet-Outlet (gal)	0.19	N/A	N/A	N/A	0.599	N/A	N/A	N/A
Sig. WVHT (ft)	N/A	N/A	1.23	N/A	N/A	N/A	1.99	N/A
Wave Period (s)	N/A	N/A	2.37	N/A	N/A	N/A	3	N/A
Note:	WEC-Sim appears to run full sim, Fixed				WEC-Sim appears to run full sim, Fixed			
	Time: 3/26/23 11:05:34, DAQ Trial # 361 (352)				**Time: 3/26/23 12:05:42, DAQ Trial # 364 (355)**			
Property ↓ Method →	**WEC-Sim**	**LIDAR/FM**	**Spotter**	**% Difference**	**WEC-Sim**	**LIDAR/FM**	**Spotter**	**% Difference**
Avg. Flow Rate (gpm)	15.537	16.3	N/A	4.793165185	15.784	16.068	N/A	1.78324752
Avg. Stroke Height (ft)	1.4	1.044	N/A	29.13256956	1.39	1.12	N/A	21.51394422
Avg. Stroke period (s)	3.051	2.816	N/A	8.010908471	2.989	3	N/A	0.367340124
Tot. Vol Pumped (gal)	308.1	325.5	N/A	5.492424242	313.05	321.1	N/A	2.538831507
Delta Inlet-Outlet (gal)	0.026	N/A	N/A	N/A	0.556	N/A	N/A	N/A
Sig. WVHT (ft)	N/A	N/A	2.24	N/A	N/A	N/A	2.29	N/A
Wave Period (s)	N/A	N/A	3	N/A	N/A	N/A	3.25	N/A
Note:	WEC-Sim appears to run full sim, Fixed				WEC-Sim appears to run full sim, Fixed			